Compact, Efficient and Flexible Drive Unit with Wide Operating Area for Conveyors

Nielsen, Simon Staal

Publication date:
2021

Document Version
Publisher's PDF, also known as Version of record

Citation for published version (APA):
Nielsen, S. S. (2021). *Compact, Efficient and Flexible Drive Unit with Wide Operating Area for Conveyors*. Aalborg Universitetsforlag. Ph.d.-serien for Det Ingeniør- og Naturvidenskabelige Fakultet, Aalborg Universitet

COMPACT, EFFICIENT AND FLEXIBLE DRIVE UNIT WITH WIDE OPERATING AREA FOR CONVEYORS

BY
SIMON STAAL NIELSEN

DISSERTATION SUBMITTED 2021

AALBORG UNIVERSITY
DENMARK

Compact, Efficient and Flexible Drive Unit with Wide Operating Area for Conveyors

AALBORG
UNIVERSITY

Ph.D. Dissertation
Simon Staal Nielsen

Dissertation submitted June 2021

Dissertation submitted: June 30, 2021

PhD supervisor: Associate Professor Peter Omand Rasmussen
Aalborg University

PhD committee: Associate Professor Lasse Schmidt (chair)
Aalborg University
Professor Hamid A. Toliyat
Texas A&M Universitet
Professor Yujing Liu
Chalmers University of Technology

PhD Series: Faculty of Engineering and Science, Aalborg University

Department: Department of Energy Technology

ISSN (online): 2446-1636
ISBN (online): 978-87-7573-918-9

Published by:
Aalborg University Press
Kroghstræde 3
DK – 9220 Aalborg Ø
Phone: +45 99407140
aauf@forlag.aau.dk
forlag.aau.dk

Printed in Denmark by Rosendahls, 2021

Preface

The research described in this dissertation has been carried out at the Department of Energy Technology at Aalborg University in the period from July 1st 2018 to June 30th 2021. The dissertation is prepared as an extended summary and a collection of papers and submitted to the Faculty of Engineering and Science in partial fulfillment of the requirements for the degree of Doctor of Philosophy.

The research is funded by Flexlink AB and the Department of Energy Technology at Aalborg University with the aim of taking the conveyor industry a step forward and the goal of making an improved drive unit for chain conveyor systems. Specifically, the X85 series of conveyors from Flexlink is used as a case study for the work presented throughout the dissertation. The collaboration with Flexlink AB was commenced prior to the period of the PhD studies, and the research described in this dissertation is initially based on a demonstrator designed by the Author and a colleague during this preliminary collaboration.

Acknowledgments

I would like to express my deepest gratitudes and appreciation to my supervisor, Peter Omand Rasmussen, who, since I met him the first time during my master studies years ago, has introduced me to the world of electric machines, magnetic gears and electronics. He has inspired through many discussions and thrown many crazy ideas on the table. His positive attitude, curious personality and perseverance will forever be an inspiration.

A big thank you is also given to Flexlink AB who have made this project possible through funding. By willingly sharing information and asking critical questions they have helped push the development in the project. The Department of Energy Technology is owed a thank you as well for their share in the funding of the project.

The guys in the workshop at the Department of Energy Technology have worked hard to manufacture the many, many parts necessary for the demonstrators build in this project. They are always there to discuss details that makes for better parts and easier manufacturing, and they do so with a smile.

Some current and former colleagues deserves to be mentioned too. Dong Wang has made a huge effort to develop control algorithms and software for the inverter made in this project. Nick and Rasmus have been offering their

help with motor design, good technical discussions and experimental work during my years at the department. A thank you is extended to Rasmus Jæger, a former co-student and colleague with whom the preliminary work for this PhD project was carried out.

Finally my partner in life, Kim, deserves a huge thank you for always meeting me with a smile and positivity despite all the late nights working at the University. She is, and forever will be, something special to me.

Simon Staal Nielsen

Aalborg University, 2021

Abstract

This dissertation investigate a suitable application for magnetic gearing technology through the specific case of a drive unit for conveyor applications. The conveyor drive unit is designed as a system consisting of a magnetic gear, a permanent magnet machine and an inverter.

The thought of utilising magnetic fields for gearing to obtain benefits of contactless power transfer has been a motivation for scientists since the beginning of the 20^{th} century. The invention of the high energy product rare earth magnets has been an enabler for magnetic gears with high torque density, and during the latest two decades, the research within the field have picked up pace. Many demonstrators have been build, mostly evolving around the concentric magnetic gear (CMG) type which offers high torque density with a "relatively" simple mechanical construction. Direct comparisons between magnetically geared electric machines and direct drive machines have shown very positive results regarding torque density, energy efficiency and material consumption.

Magnetic gearing technology have not had a commercial breakthrough despite the many demonstrators which have shown an increasing understanding of the technology. However, except a few specialised cases, the trend in the most resent work describing magnetic gears in specific application converges toward low speed, high torque applications, where the magnetic frequency, and hence rotational losses, can be kept sufficiently low. These characteristics are found in the conveyor industry, and because conveyors are used extensively within many different industries, this case pose a great opportunity for a commercial breakthrough where characteristics such as high energy efficiency, inherent overload protection, contactless power transfer and no need for lubrication will make a difference.

Through this dissertation, three iterations of a demonstrator for a magnetically geared conveyor drive unit are presented. A complete drive unit is a complex system, hence each demonstrator is used to narrow down the special focus points for modelling work and development for the next version. The last demonstrator, MagCon V3, represents a drive unit with a peak system energy efficiency (grid to chain) of 78.5% in the relevant operating area for a sprocket output power of 431 W, and the torque density for the CMG reaches 133 Nm/l.

A novel, commercially feasible approach to manufacture the ever challenging segment ring for the CMG is presented, where flanges are moulded directly onto the laminations stack via injection moulding.

Thermal steady state tests show great results at low to medium speed. At high speed, thermal challenges are encountered despite a low maximum temperatures of 84°C in the gear and 97°C in the motor windings. It is believed that the problem is caused by a mismatch between thermal expansion for laminations and polymer in the segment ring, and an alternative polymer is presented with a coefficient of thermal expansion similar to that of steel laminations.

Acoustic noise at a level higher than expected is experienced, however, this is shown to be caused by an inappropriate pole- and segment combination in the CMG, and by changing this, the acoustic noise level will likely be decreased substantially.

Two main challenges with acoustic noise and thermal expansion are likely solved by material choice and an improved pole/segment combination, and it is believed that the conveyor application will be a very good application for the CMG.

Resumé

Gennem denne afhandling undersøges det, hvorvidt en drivenhed til et transportbånd er en passende applikation for et magnetisk gear. Drivenheden designes som et komplet system bestående af et magnetisk gear, en elmotor samt en frekvensomformer.

Ideen om at udnytte magnetisme i forbindelse med gearing for at opnå en kontaktløse overførsel af kraft har motiveret forskere siden starten af det 20. århundrede. Da permanentmagneter med et højt energiprodukt blev opfundet, gjorde det ideen endnu mere attraktiv, da disse magneter har gjort det muligt at lave et magnetisk gear med en høj momenttæthed, og gennem de seneste to årtier er forskningen inden for feltet accelereret. Der er efterhånden blevet bygget mange demonstratorer, hvor størstedelen har været baseret på det koncentriske magnetisk gear, der giver mulighed for at opnå en høj momenttæthed via en relativt simpel mekanisk konstruktion. Sammenligninger mellem magnetisk gearede elektriske maskiner og maskiner designet til at drive samme applikation direkte, uden gear, har ydermere givet positive resultater hvad angår momenttæthed, energieffektivitet og materialeforbrug.

På trods af de mange demonstratorer der i stigende grad har vist en øget indsigt i, og forståelse for, de magnetiske gear, har teknologien endnu ikke oplevet et kommercielt gennembrud. Bortset fra nogle få, specialiserede tilfælde, er tendensen inden for feltet dog, at de magnetiske gear designes til applikationer, hvor lav hastighed og højt moment er et krav. Denne tendens skyldes til dels, at de hastighedsafhængige tab her kan begrænses. Den lave udgangshastighed og kravet til et højt moment findes inden for transportbåndssektoren. Da transportbånd generelt er vidt udbredte inden for rigtig mange industrier, udgør de altså en god mulighed for, at kunne give magnetgearsteknologien sit kommercielle gennembrud, og tilmed i en sammenhæng hvor egenskaber som høj energieffektivitet, indbygget overbelastningssikring, kontaktløs overføring af kraft samt det, at der ikke er behov for smøring af det magnetiske gear, kan gå ind og gøre en forskel.

Gennem denne afhandling præsenteres tre iterationer af en magnetisk gearet drivenhed, der bygger på det koncentriske magnetiske gear. Da en komplet drivenhed udgør et komplekst system, vil det fremgå, hvordan hver iteration udnyttes til at få en bedre forståelse for, hvor indsatsen skal lægges med hensyn til at forbedre teoretiske modeller, samt hvilke aspekter af drivenheden der skal fokuseres på. MagCon V3 er den tredje og sidste iteration som præsenteres i denne afhandling. Her demonstreres en maksimal energieffektivitet (fra forsyningsnet til akseleffekt) inden for det relevante arbejdsområde på 78.5% ved en akseleffekt på 430 W, og momenttætheden for det magnetisk gear måles til 133 Nm/l.

Segmentringen i det koncentriske magnetisk gear har altid været en udfordring at fremstille. Denne afhandling introducerer en effektiv fremstillingsproces, hvor flangerne, der anvendes til at fastgøre segmentringen, støbes direkte på de motorblik selve segmentringen er lavet af, via en sprøjtestøbeproces.

Gennem termiske forsøg demonstreres det, hvorledes MagCon V3 klarer sig godt fra lav til medium hastighed. Ved maksimal hastighed opstår der problemer der sættes i forbindelse med temperaturen i segmentringen, og det til trods for de forholdsvis lave temperaturer der ikke overstiger 84°C i segmentringen og 97°C i motorviklingerne. Data fra MagCon V2 og V3 tyder på, at problemet opstår på grund af forskelle i den termiske udvidelseskoefficient for motorblikkene og den polymer der er anvendt i støbeprocessen, og der gives et bud på en alternativ polymer med en termisk udvidelseskoefficient, der ligger tættere på udvidelseskoefficienten for motorblik.

Niveauet for den akustiske støj fra de magnetisk gearede drivenheder overstiger det forventede niveau. Den primære kilde til den akustiske støj viser sig at være en uhensigtsmæssig kombination af poler og segmenter i det magnetisk gear, og ved at vælge en mere hensigtsmæssig kombination forventes det, at den akustisk støj kan reduceres betydeligt.

De to primære udfordringer med akustisk støj og termisk udvidelse kan altså med stor sandsynlighed løses via alternative materialevalg samt en ny kombination af poler og segmenter i det magnetisk gear, og de øvrige resultater i dette projekt peger på, at en drivenhed til transportbånd er en rigtig god applikation for det magnetiske gear.

Dissemination

The present dissertation is prepared as a collection of scientific papers. Research that have not been documented through scientific papers is described throughout the extended summary.

Peer-reviewed publications included in the dissertation

A) S. S. Nielsen, R. K. Holm and P. O. Rasmussen, "Conveyor System With a Highly Integrated Permanent Magnet Gear and Motor," in IEEE Transactions on Industry Applications, vol. 56, no. 3, pp. 2550-2559, May-June 2020, doi: 10.1109/TIA.2020.2977877.

B) S. S. Nielsen, R. Koldborg Holm, N. I. Berg and P. Omand Rasmussen, "Magnetically geared conveyor drive unit - an updated version," 2020 IEEE Energy Conversion Congress and Exposition (ECCE), 2020, pp. 285-292, doi: 10.1109/ECCE44975.2020.9235375.

C) S. S. Nielsen, H. Y. Wong, H. Baninajar, J. Z. Bird and P. O. Rasmussen, "Pole and Segment Combination in Concentric Magnetic Gears: Vibrations and Acoustic Signature," in IEEE Transactions on Energy Conversion, (Not published - under review)

Other relevant peer-reviewed publications

D) S. S. Nielsen, R. K. Holm and P. O. Rasmussen, "Conveyor System with a Highly Integrated Permanent Magnet Gear and Motor," 2018 IEEE Energy Conversion Congress and Exposition (ECCE), 2018, pp. 2359-2366, doi: 10.1109/ECCE.2018.8557607.

E) S. Korsgaard, A. B. Kjaer, S. Staal Nielsen, L. Demsa and P. O. Rasmussen, "Acoustic Noise Analysis of a Magnetically Geared Permanent Magnet Generator" 2019 IEEE Energy Conversion Congress and Exposition (ECCE), 2019, pp. 717-723, doi: 10.1109/ECCE.2019.8912892.

F) A. B. Kjaer, S. Korsgaard, S. S. Nielsen, L. Demsa and P. O. Rasmussen, "Design, Fabrication, Test, and Benchmark of a Magnetically Geared Permanent Magnet Generator for Wind Power Generation," in IEEE Transactions on Energy Conversion, vol. 35, no. 1, pp. 24-32, March 2020, doi: 10.1109/TEC.2019.2951998.

G) S. S. Nielsen, T. Kerekes, D. Sera and P. O. Rasmussen, "Improvement of Ventilation Drive System with Solar Power and a Voltage Level Based Control Structure," 2018 IEEE Energy Conversion Congress and Exposition (ECCE), 2018, pp. 2549-2554, doi: 10.1109/ECCE.2018.8557499.

Dissemination through conference presentations: Paper B, D, E and G

The dissertation is based on some of the submitted/published scientific papers and conducted dissemination listed above. Each scientific paper is associated with a co-author statement which is made available to the assessment committee.

Contents

1

Introduction

Being able to convey material or items, being bulk materials or single components, assemblies on an assembly line or components and packages for sorting or storing, is a huge part of industry today. Many references to conveyors and their use through history can be found. One of the more famous and well-known examples are the optimised production of the Ford model T in 1913 where Henry Ford was able to produce a car in 90 minutes by utilising conveyors in the manufacturing infrastructure [1]. The mining industry also presents some very impressive conveyor systems, such as the 50 km long conveyor belt owned by Worsley Alumina in Australia used to transport the raw bauxite from the mine to the refinery. It is also in the mining industry that some of the fastest conveyor belts are found. German RWE are using conveyor belts running as fast as 15 m/s to remove the overburden material which covers the desired lignite, also known as brown coal.

A conveyor in its most simple form is a chute where material, components or packages are moved by gravity, but off cause, more versatility is added in a powered conveyor, which may be based on a combination of powered and passive rollers on which the conveyed items are transported directly, or based on a driven and an idling pulley wheel on which a looped belt or a chain is fitted.

Drive units for stationary conveyor systems in manufacturing facilities and the like are typically based on electric machines and can roughly be divided into two categories: Direct drive solutions and geared solutions. These solutions are further seen implemented as integrated drum motors, where motor and gear, if existing, is designed into the pulley wheel only with the electrical wiring exiting the assembly, or as the more common combination of a pulley wheel driven by an external electric motor which may be geared or not.

The directly driven solutions have the advantages of simplicity, low maintenance and robustness as very few components are used and no lubrication is needed except for the bearings. Due to the interdependence between torque and volume in electric machines [2], it may however be beneficial to combine a physically smaller fast running electric machine with a gearbox to obtain a high output torque while maintaining a compact system. A pulley wheel combined with an external, geared electric machine is a typical solution and available in conveyor solutions from many manufacturers [3] [4] [5].

1.1 External drive solutions

This dissertation concerns drive units below 1 kW, and in this power range many standard geared motors are available. The basic option is a fixed speed drive comprised of an induction machine directly connected to the grid and geared by some form of mechanical gearbox. For applications requiring variable speed a frequency converter is introduced. An example of a typical geared motor with frequency converter in this class is the Movimot from SEW Eurodrive who is one of the suppliers for large conveyor manufacturers such as Bosch Rexroth [5] and Flexlink [3]. The Movimot line includes a wide range of standard gear boxes and motors to cover different loads and speeds.

The directly driven, externally mounted solutions are less common. In [6] a 500 kW, 60 rpm PM synchronous machine with high pole count is developed as a direct drive for a conveyor in a coal mine. On the more commercial side, Dorner [7] has introduced the semi-direct drive seen in Fig. 1.1 where a transverse flux PM machine from ETM is driving the conveyor through a timing belt. The timing belt is introduced to offset the motor-axis from the conveyor roller-axis and make the mounting more flexible.

Fig. 1.1: Semi-direct drive from Dorner [7].

It is stated that this machine surpasses their geared drives in operating range with a constant torque of 5.5 Nm in a speed range of 10-300 rpm with a peak efficiency of 89 %. Hereby a single motor is able to cover the operating areas of several different geared drives. A specialized electric machine topology such as the transverse flux machine is known for a high torque density which enables more compact direct drive units. However, other factors such as a low power factor must be taken into account, as this has an influence on the inverter rating for the drive unit [8].

1.2 Drum motors

Drum motors first appeared in 1928 and a patent on this design was obtained in 1932 [9]. The drum motors have been developed to utilise otherwise empty space inside conveyor rollers in a pursuit of even more compact solutions. The drum motors further introduces a drive unit which is simple to install and very rugged towards ingress of dirt, dust and liquids as everything is enclosed in the drum. Drum motors are both available as geared and direct drives, and are in general long and slender solutions. As an example of the geared drum motors, Interroll [10] offers a variety of combinations between induction motors, permanent magnet synchronous motors (PMSMs) and steel as well as polymer gear boxes implemented into the drum which drives the conveyor belt. A selection is shown in Fig. 1.2.

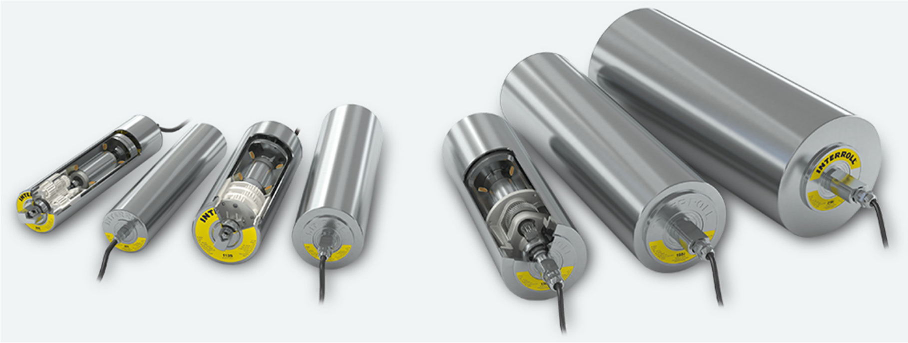

Fig. 1.2: Example of geared drum motors from Interroll [11].

Interroll can provide drum motors from 25 W to 1100 W in different series of rollers in diameters from 81.5 mm to 138 mm and lengths of 250 mm to 1600 mm. The development and test as well as experimental validation of these drum motors have seen academinc interest in [12] and [13] where a multiphysics thermal model of a line fed permanent magnet motor for the drum solutions for Interroll is presented.

Drum motors are also found as direct drives. An example is Magnetic Innovations [14] who offers direct drive drum motors based on a PM synchronous machine with a continuous torque of 44.4 Nm and a continuous power of 310 W. They furthermore offer two different directly driven “smart conveyor belt motors”, with the option of an absolute position sensor for automation purposes. These are relatively short, side mounted drum motors with lengths of 103 and 140 mm and a diameter of 125 mm. They deliver 3.5 and 8 Nm continuously and runs with a speed up to nominal 300 rpm.

1.3 Case study - Flexlink X85H chain conveyor

The work presented in this dissertation is based on the X85H series of chain conveyors from Flexlink AB which is used as a specific case study for developing an improved conveyor drive unit. In this chain conveyor system, items are conveyed by the chain on top of an aluminium beam before the chain return on the bottom of the beam. At one end of this beam, a drive unit is mounted, and at the other end, a passive idling unit is mounted. Depending on the specific load point of a system, the drive unit can be driven by a number of combinations of standard gear boxes and electric machines to fit the load and speed required in the application.

In Fig. 1.3 the X85H drive unit and a geared motor is mounted in the system, and in Fig. 1.4 the isolated drive unit and geared motor is seen. In this figure, the sprocket that interacts with the conveyor chain is furthermore visible. The width of the drive unit is 85 mm which fits the width of the conveyor chain. As seen on Fig. 1.4 the drive unit is flat on the side opposite to the motor so that two mirrored conveyor drive units can be placed directly next to each other. Another important feature is the height of the geared motor. This must be kept below the height of the conveyor chain so that item wider than the conveyor chain can be conveyed.

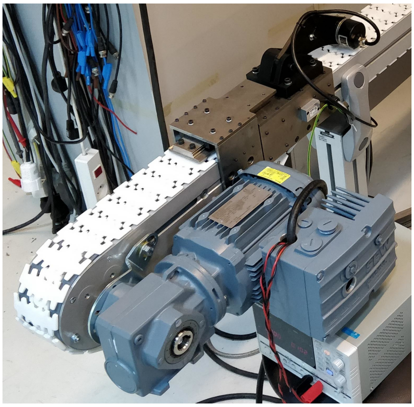

Fig. 1.3: The X85H chain conveyor series with one of the currently available geared motors.

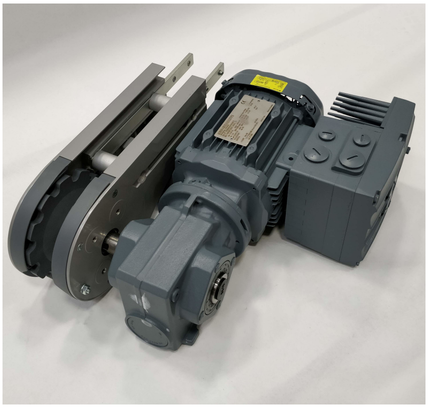

Fig. 1.4: Isolated drive unit and geared motor. The sprocket that interacts with the chain is seen between the two flanges.

The X85H series covers the operating area seen in Fig. 1.5 where speed and load on the chain is given. As the sprocket has a mean radius of 64.7 mm the operating area can be converted into torque and revolutions per minute (rpm) on the sprocket as shown in Fig. 1.6. The maximum continuous torque is 81 Nm, however, to overcome static friction and inertia loads at startup, a peak torque of 100 Nm has been specified from Flexlink. Please note, that axis values for torque and rotational speed on Fig. 1.4 is rounded off to improve readability of the figure. To evaluate accurate output power, use force and speed from Fig. 1.5.

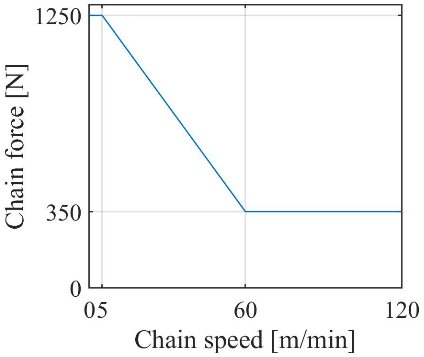

Fig. 1.5: Operating area of the X85H conveyor series from Flexlink AB, chain speed and force.

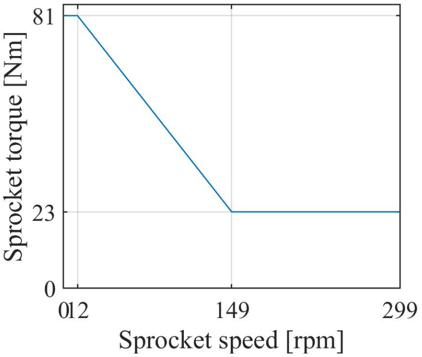

Fig. 1.6: Operating area of the X85H conveyor series from Flexlink AB, sprocket speed and torque.

When standard gears and motors are used to cover this entire operating area, the number of unique parts and possible combinations are growing quickly. To get an idea of the extent of combinations, the X85H options are shortly reviewed.

Motors comes in 5 different power ratings, and the gearboxes comes in 3 types, each type available with different gear ratios. Also, the motors come in different versions depending on the frequency and voltage of the grid they are connected to.

Most of the geared motors are available as fixed or variable speed, and the variable speed drive units are available with the frequency converter mounted to the motor or separated from the motor. Furthermore, all drive units can be equipped with a slip clutch to prevent overload of the chain, and naturally, the motor and gear can be placed on the left or the right side of the chain. Hence, it should be clear by now that a lot of unique part numbers and combinations have to be managed.

1.3.1 Reference drive unit

To have an idea of the physical properties and performance of the current solution, one of the popular geared motors, Movimot SA37, is evaluated. The majority of X85H conveyors that goes to the market are specified for the lower speed range where the Movimot SA37 shown in Fig. 1.4 is a typical solution. The specifications for the geared motor and the physical properties of the complete drive unit system consisting of drive unit, geared motor and frequency converter is given in Tab. 1.1.

Movimot nameplate information	
Motor type	Induction machine
Motor nominal power	370 W
Gear type	Helical / worm gear
Gear ratio	53.83:1
Gear output speed range	5.2-26 rpm
Gear output nominal torque	88 Nm

Physical properties	
Length	411 mm
Width	346 mm
Height	183 mm
Mass	20.5 kg

Table 1.1: Movimot SA37 and drive unit specifications.

To further characterise the system, the system energy efficiency is evaluated by Eq. (1.1). The input for Eq. (1.1) is obtained experimentally in the laboratory.

$$\eta_{system} = \frac{P_{chain}}{P_{grid}} \cdot 100 \tag{1.1}$$

P_{grid} is the frequency converter input power [W] measured by a power analyzer and P_{chain} is the output power [W] calculated from chain speed and chain force as in Eq. (1.2) with F_{chain} being chain force [N] and v_{chain} being chain speed [m/s].

$$P_{chain} = F_{chain} v_{chain} \tag{1.2}$$

Chain force and speed are obtained from a modified conveyor system where the chain force is measured by a load cell and the chain speed is measured by an encoder wheel. In one end of the conveyor the device under test (DUT) is mounted, and in the other end a geared PMSM servomotor is mounted to control the chain force. The chain force is varied by changing the ohmic load on the servo motor.

The efficiency map is shown in Fig. 1.7 where the red line indicates the operating area. Due to the passive ohmic load on the load machine, it is not possible to reach maximum load at low speed. The maximum system efficiency is 37.2 % in the area which is evaluated. This is not impressive but not surprising either due to the combination of an induction machine and a worm gear with a high gear ratio.

Two distinct advantages of the worm gear, which is used in the gearbox for the Movimot SA37, is that they are self locking and that they can obtain

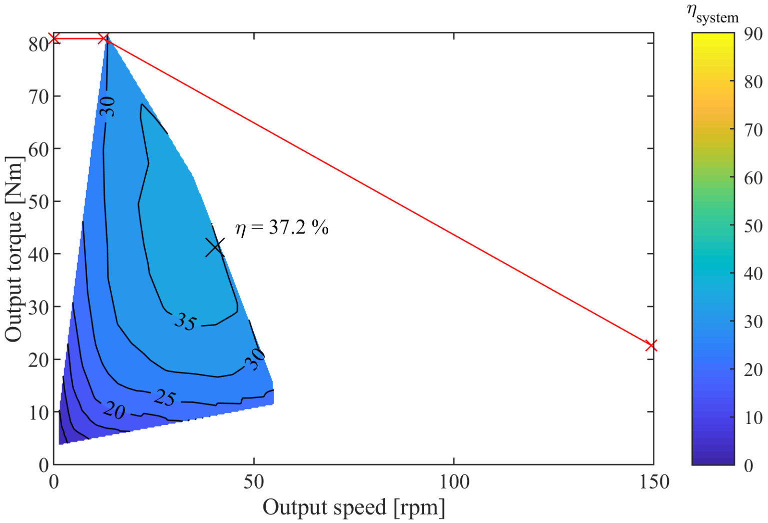

Fig. 1.7: System efficiency with Movimot SA37.

very high gear ratios in a single stage. However, a well-known property, and disadvantage, of the worm gear is low energy efficiency. In [15], two worm gears with gear ratios of 7:1 and 28:1 were tested both clockwise and counter clockwise with a mechanical input power of 1.6 kW on the 7:1 gear and an input power of 0.53 kW on the 28:1 gear. Both gears were operated with and input speed of 1400 rpm and at nominal torque. Efficiencies between 61 % and 92 % were measured. In general, the efficiency of worm gears is highly dependent on the conversion ratios and the load applied to the gear due to the friction between worm screw and gear which is the largest loss component in these types of gear [16].

1.4 Customer motivation

When customers to Flexlink are choosing drive units and geared motors for their applications, obviously it is important to them, that what they buy is able to perform the task they want it to perform. When asking Flexlink in more detail about what seems important to their customers when choosing drive units, the following parameters are highlighted:

- Low purchase prise.
- Compact unit to increase possibilities for implementation in tightly packed applications.
- Not too heavy.

- Some degree of reconfigurability to fit the unit into the application.
- For applications in sensitive environments: No active cooling to avoid stirring and moving the air.

Customers rarely asks about energy efficiency of the geared motors as they have larger focus on purchase price than on the cost during the lifetime of a product. The Author somehow considers it as the duty of academia and also OEMs to educate customers on energy efficiency since this is important, not only from an economic point of view, but also from an environmental point of view.

An increasing demand to have access to data from a production facility and to improve the possibilities of controlling each unit in a production facility individually to increase the flexibility is also seen. Hence, the following two bullets are added to the list:

- Energy efficiency.
- Increase access to data and enable individual control of drive units.

These six points should be considered and have influence when designing a new drive unit solutions for conveyor applications.

1.5 Novel approaches

In [17] a novel approach to improve conveyor drive units is proposed. A magnetic gear consisting of two magnetic wheels with skew magnets is developed to transfer the torque between two perpendicular shafts, see Fig. 1.8.

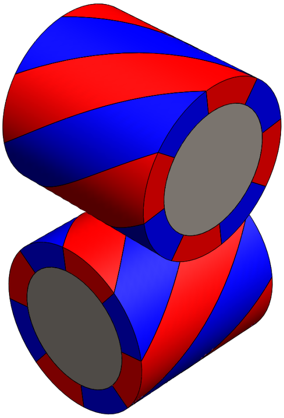

Fig. 1.8: Magnetic gear with perpendicular axis. Torque transferred by helix shaped magnets.

Fig. 1.9: Helical angular MG from Misumi [18].

The magnetic gear is replacing a connection previously facilitated by a belt, however, by implementing a contactless magnetic gear, the dust created by the wear between belt and pulleys over time is avoided. The importance of this is emphasized, as this specific conveyor operates in an environment very sensitive to dust.

The implementation of a magnetic gear is very interesting and the technology developed in [17] is commercially available, shown in Fig. 1.9 [18] [19]. However, the specific type of magnetic gear has a very poor utilisation of the magnets. As it is seen in Fig. 1.8, only a fraction of the magnet material is "engaging" and hereby actively contributing to the torque transmission. The gear is transferring 0.356 Nm with a gear ratio of 1:1 (basically constituting angular magnetic coupling) and if the volume of the gear is taken as a box enclosing the gear wheels, the gear has a torque density of 6.54 Nm/l. This is in the range of the torque density obtainable by naturally cooled radial flux permanent magnet synchronous machines (PMSMs) which as a rule of thumb is 10 Nm/l [20].

1.6 Magnetic gears and applications

The idea of implementing a magnetic gear in conveyor drive units is interesting due to the inherent properties of the technology which include [21]:

- No physical contact.
- Inherent overload protection.
- Potential for very high energy efficiency.
- No teeth lubrication and reduced maintenance.
- Potential for improved reliability.
- Low requirements to "teeth tolerances".
- Reduced acoustic noise from mechanical contact.
- Linear device, no backlash.

Many magnetic equivalents of classic gears such as spur gears, worm gears and bevel gears have been investigated and in some cases physical demonstrators have been built. The first appearance of a magnetic gear was described in a patent from 1901 by Charles G. Armstrong [22] were an electromagnetic spur gear was presented, however, without the strong rare earth magnets developed in the early 1980's, magnetic gears have not been able to compete with the torque density of classical mechanical gears.

It is not only the availability of high energy product magnet materials that has influence on the torque density. In the magnetic equivalents of gear types such as spur gears, worm gears and bevel gears, only a few magnets are contributing to torque transfer at a given instant, just like only a few teeth are engaged at a certain instant in the mechanical counterpart. Consequently, these gear types demonstrates very poor utilisation of the permanent magnets with a low torque density as a result. In [23] a magnetic spur gear is developed and a demonstrator is manufactured to validate the models. After optimising the magnetic structure an experimentally measured torque density of 18 Nm/l was obtained.

In recent years, research is focused on gear topologies where a larger part of the magnet material is contributing to the torque transmission at each instant. These more torque dense topologies includes the magnetic counter part of planetary, cycloidal and harmonic gears as well as the concentric magnetic gear (CMG) seen in Fig. 1.10.

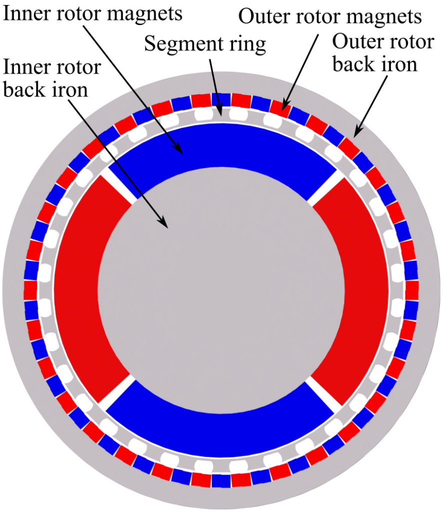

Fig. 1.10: Cross section of the concentric magnetic gear. Based on [24].

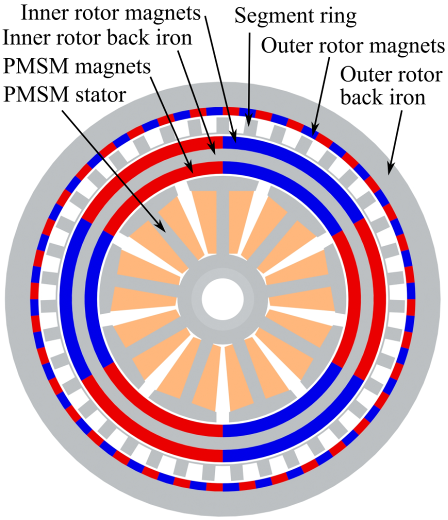

Fig. 1.11: Cross section of a CMG with integrated PMSM.

Especially the CMG has drawn the attention of researchers due to the high torque density and relative simple mechanical design compared to the other three topologies [25]. In 2001, a century after the idea of magnetic gears was first published, [20] presented theoretical work describing a CMG with a simulated torque density of 100 Nm/l, defined by Eq. (1.3) where τ_{stall} is the stall torque [Nm] of the MG and $V_{act.}$ is active magnetic volume [l] given by the stack length and the outer diameter of the outer rotor.

$$\rho_\tau = \frac{\tau_{stall}}{V_{act.}} \tag{1.3}$$

Although the CMG was first presented in a patent by Jr. Thomas B. Martin in 1968 [26], [20] is commonly accepted as a milestone paper for the magnetic gearing technology and since then, several physical demonstrators have been build [27].

The CMG consists of three concentric rotors. The inner rotor is the high speed rotor (HSR). The middle rotor is the segment ring, also known as the flux modulating rotor, which modulates the space harmonics of the flux density from the inner rotor poles to match the space harmonics of the flux density from the poles on the outer rotor. Different properties can be obtained based on which rotor, if any, is fixed, and which rotors are used as input and output.

The relation between the number of pole pairs on the rotors and the number of segments is given by Eq. (1.4).

$$Q = p_o \pm p_i \tag{1.4}$$

With Q being the number of segments, p_i the number of pole pairs on the inner rotor and p_o the number of pole pairs on the outer rotor. When choosing a pole- and segment-combination according to Eq. (1.4), the relative speed of the three rotors are given by Eq. (1.5)

$$\omega_i = \frac{p_o}{p_o - Q} \cdot \omega_o + \frac{Q}{Q - p_o} \cdot \omega_{seg} \tag{1.5}$$

Where ω_i, ω_o and ω_{seg} is the rotational speed of inner rotor, outer rotor and segment ring respectively [28]. It is common to chose Q as given in Eq. (1.6) as this yields the highest torque.

$$Q = p_o + p_i \tag{1.6}$$

The gear ratio depends on which rotor is fixed, and when choosing the number of segments according to Eq. (1.6), the gear ratio for the three different configurations can be derived from Eq. (1.5) by setting the rotor speed of the fixed rotor equal to zero. The relations between input- and output-speed are then given by Eq. (1.7), (1.8) and (1.9) with stationary *outer rotor*, *segment ring* and *inner rotor* respectively.

$$\omega_o = 0: \quad \omega_i = \left(\frac{p_o}{p_i} + 1\right) \cdot \omega_{seg} \tag{1.7}$$

$$\omega_{seg} = 0: \quad \omega_i = -\frac{p_o}{p_i} \cdot \omega_o \tag{1.8}$$

$$\omega_i = 0: \quad \omega_o = \left(\frac{p_i}{p_o} + 1\right) \cdot \omega_{seg} \tag{1.9}$$

The configuration in Eq. (1.7) and (1.8) are most common, and the choice between the two depend on the specific application and requirements. The configuration in Eq. (1.9) is not as useful, as the gear ratio is very small.

The idea of integrating an electric machine with a magnetic gear to obtain a compact machine with low speed and high torque output emerged only three decades after the first ideas about magnetic gears saw the light of day, and it was described in a patent obtained in 1933 [29]. In this dissertation the concept is referred to as the Motor Integrated Permanent Magnet Gear (MIPMG) and it is illustrated in Fig. 1.11 where a stator is placed in the centre of the CMG and motor magnets are placed on the inside of the inner rotor back iron. A version where the stator is placed on the outside of the outer rotor has also been presented under the name Pseudo Direct Drive (PDD). A detailed overview of the state of art of magnetic gears is given in [28] [25] [27].

A lot of research has been dedicated to determine basic properties of magnetic gears of different topologies, but except a very early attempt [30] where a reluctance type of magnetic gear was integrated with an axial flux machine for robotics applications, research aimed at designing magnetic gears into actual applications has only taken place for the latest decade.

1.6.1 Applications for magnetic gears

In [31] and [32], basically identical MIPMGs was presented in a traction application for electric motorcycles and for a wind turbine generator application, and it seems like only the winding configuration sets the two machines apart as all physical dimensions and the pole configuration matches each other. The gear ratio in both papers is 7.33:1. In [31] and [32] the rotor from an outer rotor brushless DC machine (BLDC) was basically combined with the high speed rotor of a CMG on a mutual back iron, and the stator for the BLDC machine was placed in the center, an idea which was presented in a patent by Rolls Royce [33]. The MIPMG from [31] and [32] comprises a compact unit with a low speed and high torque output. In this work, the outer rotor is used as output rotor. In [31] an output speed of 600 rpm and a peak torque of 103 Nm is presented, yielding a theoretical torque density of 87 Nm/l. However, the stack length of gear and BLDC is the same, hence the end windings of the BLDC will take up additional space, and the output torque is only presented as the peak BLDC torque multiplied by the gearing ratio. In general, not much detailed work is presented, as well as no demonstrator and experimental validation is shown.

The work done in [32] is further elaborated upon in [34] where a demonstrator has been build and test results are presented. The nominal power for the wind turbine generator is 500 W at 136 rpm. At this load point, a measured efficiency of 72 % is stated. Some positive indications are found by comparing the MIPMG with a scaled direct drive machine (DDM) designed as a wind turbine generator. Here it is found, that the volume and the mass of the MIPMG is 56 % and 39 % respectively of the volume and mass of the DDM which is very promising estimates.

These findings are backed up by [35]. Here, a 3.5 kW MIPMG for wind power generation is presented. It is designed with the same specifications regarding input speed and power as a commercially available DDM for a small wind turbine, and the purpose of the demonstrator is to facilitate a direct comparison between a DDM and a MIPMG. The reduction in the amount of materials used is given in Tab. 1.2.

	Factor
Total mass [kg]	4.2
Total volume [L]	5.5
Copper mass [kg]	11.5
Electrical steel mass [kg]	3.9
Magnet mass [kg]	1.3
Housing [kg]	3.8

Table 1.2: Reduction in material use for 3.5 kW MIPMG wind turbine generator [35].

Despite improving the efficiency at nominal load by 1.7 percentage points, the surface area of the MIPMG was significantly smaller, so the steady state temperature was higher, and the acoustic noise level was increased as well [36]. The results are very promising though, as they clearly show significant savings for all materials, reduced volume and increased efficiency in a direct comparison with a DDM.

A magnetically geared generator for wind turbines on a larger scale is presented in [37] where an analytical model is used to optimise a 10 MW PDD in a theoretical study, and it is shown that an energy efficiency greater than 98.5% should be possible. However, the loss model only takes copper loss and iron loss into account, hence mechanical losses, windage losses and eddy current losses in the magnets are not included. A physical demonstrator of a 500 kW PDD wind turbine generator has been build and successfully tested by Magnetomatics in the EU H2020 DemoWind program, and this demonstrator is the largest magnetic gear build to date with a nominal torque of 200 kNm [38]. Unfortunately, not much detailed information is available.

In [39] very detailed work is presented regarding a MIPMG. The MIPMG is designed for traction applications, where the design has taken its offset regarding dimensions, power and gear ratio of the traction motor used for a Toyota Camry. The gear for the MIPMG is designed with the outer rotor as output and has a gearing ratio of 8.83:1, with a base speed of the integrated PMSM of 4000 rpm and the possibility of running at constant power of 35 kW up to 14000 rpm. The mechanical implementation is described quite thoroughly, and an interesting analysis shows, that it is possible to make the stack length of the PMSM shorter than that of the gear while still matching the torque between PMSM and gear. This leaves space for the end windings inside the gear so that the torque density of the active parts become a more "true" torque density compared to earlier work. Another detail is the addition of a bridge between the segments in the flux modulator ring. This bridge is added to improve the structural integrity of the modulator ring, improve manufacturability, and also to minimise the flux variation seen by the high speed magnets to reduce eddy current losses in these. It is shown that this bridge has an insignificant effect on the output torque. In [40] the MIPMG is thoroughly tested, and a measured stall torque of 520 Nm is obtained, corresponding to a torque density of 92 Nm/l. It is found that the losses in the MIPMG are extremely high, and a series of tests show, that the rotational losses are high due to a high magnetic frequency in combination with details in the manufacturing process and choices in the mechanical construction and materials used, as substantial eddy current losses was induced in the surrounding components and in the titanium sleeve used to retain the magnets on the inner rotor. Finally, the limited availability of lamination materials further increased rotational losses, hence at 3500 rpm on the PMSM the rotational loss amounts to 3.9 kW.

In [41] an improved second version of the MIPMG (MIPMGv2) was presented where much effort was put into reducing the rotational losses of the MIPMG. This is mainly done by reducing the maximum PMSM speed to 10000 rpm as well as reducing the number of poles on all rotors. Also, both outer and inner rotor is made with buried, axially segmented magnets to minimise eddy current losses and avoid the titanium sleeve. 0.2 mm laminations are used for all laminated parts and larger air gaps as well as so-called dummy slots in the bottom of each segment on the segment rotor are implemented to further smooth out the flux variations seen by the inner rotor magnets, hereby further reducing eddy current losses. In the MIPMGv2 the segment ring is used as the output rotor. This increases the structural rigidity of the MIPMGv2 and allows for liquid cooling of the outer rotor, and it increases torque density. Liquid cooling was also added to the PMSM stator shaft, however this was very inefficient. The maximum output speed was 1200 rpm with the 9:1 gearing ratio and the measured stall torque of the

MIPMGv2 was 857 Nm, yielding a measured torque density of 99.7 Nm/l. The derivation of specifications and documentation of implementation in the test vehicle is presented in [42]. The MIPMGv2 obtained an energy efficiency above 90 % in a very large part of the intended operating area, and a peak efficiency above 93 % was obtained.

At an equivalent speed of 135 km/h, losses were reduced with a factor 8 in the MIPMGv2 compared to the MIPMGv1. However, the losses were still 2.28 times higher than estimated by the models. Part of this additional loss was found as eddy current losses in the surrounding structural components. Especially components monted close to the end of the magnetically active components experienced significant eddy current losses, and after modifying the length of the segment ring, replacing some stainless steel parts with PEEK and removing some material where high flux variations were seen, the losses was reduced to a factor of 1.65 compared to the models. The MIPMGv2 is at good example to show, that it is absolutely possible to design a good magnetically geared PMSM where high torque density and good thermal performance is obtained, but the development history of this demonstrator also shows that when CMGs are designed with high magnetic frequencies, and also designed in a compact manner to fit the application, extreme care must be taken in the choice of materials and the design of surrounding components to limit the rotational losses.

In [43] and [44] the results from the research on two prototype CMGs for vertical take-off and landing (VTOL) vehicles done by NASA is presented. The requirement for the targeted CMG is high specific torque, as mass is an important factor in aviation. The targeted output speed is 4500 rpm, even higher than what was presented for the two MIPMGs from [39] and [41]. The authors specifically highlights the following reasons for initiating the CMG research:

- No lubrication.
- Potential of reduced cabin noise.
- Elimination of regular grounding of the VTOL vehicles due scheduled maintenance sessions.

To obtain a high specific torque, the mass of the CMGs are kept low by implementing a Halbach array on both inner- and outer rotor which increases the magnetic field strength and eliminates the need for back iron on the two rotors. Besides saving weight, the absence of back iron decreases the rotational losses significantly. To decrease the rotational losses further, eddy current losses in the magnets are kept low by laminating them axially from 1 mm thick pieces. Finally, in the second demonstrator that is presented, the segments in the segment ring are made from a cobolt steel (HIPERCO 50) to increase the magnetic saturation level and decrease losses. To further decrease the mass, the radial dimension of the segments were only 2.65 mm [45]. The supporting structure around the magnetic components is printed from carbon reinforced nylon to obtain the required mechanical strength while maintaining a low mass and a carbon fiber sleeve is wound around the inner rotor magnets to retain them at high speed. An impressive estimated 40 Nm/kg and 147 Nm/l is obtained for the second demonstrator. For comparison, the MIPMGv2 from [41] had a specific torque of 10.5 Nm/kg [28] and the magnetically geared wind turbine generator from [35] had a specific torque of 11.43 Nm/kg. It is not completely fair comparisons, as the MIPGMv2 and the generator also included a PMSM and not only the CMG, however, a factor of 4 in specific torque compared to well designed CMGs with torque densities of 99.7 and 85.6 Nm/l is a significant difference, also when the PMSM is taken into account.

The authors in [43] and [44] have succeeded in designing CMGs with impressive specific torque which fits their application very well, but they have used exotic and expensive materials, both for all the supporting structure as well as in their magnetic design. They further had troubles during testing, as the segment ring in their second demonstrator failed. One of the reasons the segment ring failed was the small radial dimension which did not provide sufficient mechanical strength and it still needs to be proven that this problem can be solved.

An area where promising tendencies for CMGs have been highlighted is in marine energy applications. In marine energy applications repairs and maintenance is inconvenient and the costs are high since special equipment must be used, hence the more rugged the generators can be designed and the less maintenance that is required, the better. In [46] the following properties are emphasized when comparing to solutions with mechanical gears:

- Inherent overload protection.
- Contactless torque transfer.
- No lubrication of gear.

In [47] an MIPMG is build for marine energy applications. In this work, the inherent overload protection is specifically pointed out as an advantage, as the difference between peak wave power and average wave power in these applications is high. Hence, the CMG and PMSM in the MIPMG can be designed with a power rating lower than the peak power, yielding a smaller an less expensive unit. A scaled version is designed and a demonstrator is build and tested with success. A measured stall torque of 3870 Nm is obtained which yields a torque density of 82.8 Nm/l. The peak efficiency measured on the demonstrator is above 90%. As this demonstrator is build with the purpose of showing that a magnetic gear of this size is feasible, the integration of the magnetically active components with all the surrounding mechanical parts is done in a very conservative fashion to avoid additional losses an to ensure the functionality of the gear. This means that the physical size of the generator is quite big.

In [48] and [49] the 1st and 2nd stage of an CMG for a Marine Hydrokinetic Generator (MHG) are presented. The magnetic gearbox is designed for 5 kW input at 40 rpm, and the 2-stage design is chosen to obtain a total gearing ratio of 1:63.3, hence quite high compared to other single stage CMG that have been demonstrated. This gearbox takes advantage of the non-contact torque transfer, as the segment ring of the first stage is used to hermetically seal the inner rotor, the second stage CMG and the generator. A conceptual drawing is seen in Fig. 1.12 where the segment ring is denoted "Fixed modulator".

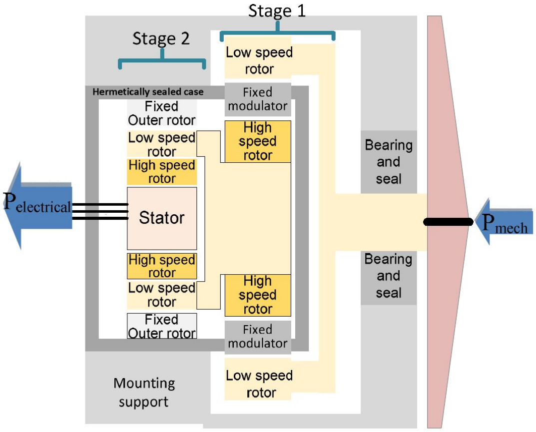

Fig. 1.12: Conceptual drawing of the 2-stage magnetic gearbox for the MHG. Illustration from [48].

By utilising Halbach magnet arrays and flux focusing structures on the rotors, 3D FE models yields impressive torque densities of 306.4 and 276.5 Nm/l for the 1st and 2nd stage. The outer rotor back iron is not included in the volume however, as it is not seen as a magnetically active part due to the use of Halbach arrays, hence this makes the comparison to the demonstrator in [47] a little unfair. Also, [47] had the generator integrated into the CMG and only needed *one* gear stage. In Fig. 1.12 the initial idea of implementing the generator into the 2nd stage gear is illustrated, however, in [49] it is made clear that there is not enough space and that a separate generator is needed. This makes a direct comparison between the two solutions difficult but if the torque density of the two-stage gearbox is calculated from the combined volume of the two CMG stages and the stall torque of the 1st stage, a theoretical torque density of 260 Nm/l is obtained. Even though the outer rotor back iron and generator is not included, this is quite high.

1.6.2 Comparison to mechanical gears

To get an idea of the performance of CMGs compared to that of mechanical gears [50] made a study concerning commercial available mechanical gears of various types. Among other parameters, the study compares torque density, gear ratio and input speed. The volume used for the torque density is calculated from the gear box dimension excluding features such as flanges for mounting motors and securing the gearbox. It can be discussed how to calculate volumes for accurate comparisons of CMGs and mechanical gears, however, the data from [50] gives a good idea about the torque density of various mechanical gear commercially available. Fig. 1.13 show the torque density of the mechanical gears as a function of gear ratio and it is seen that worm gears and spur gears/helical gears in general offers the lowest torque density while the mechanically more advanced planetary, cycloidal and harmonic gears offer quite high torque densities.

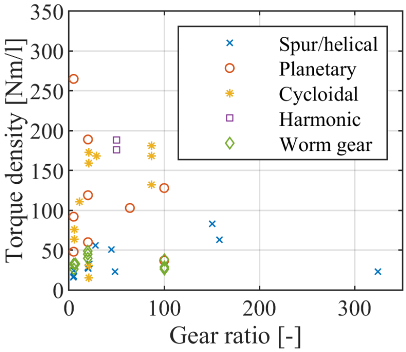

Fig. 1.13: Torque density of mechanical gears as function of gear ratio. Data from [50].

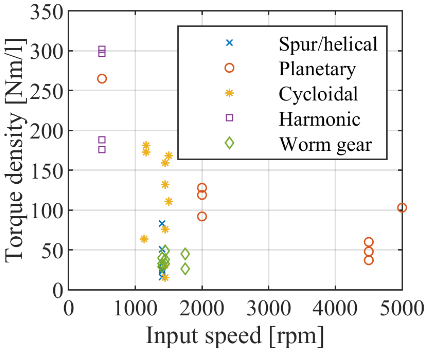

Fig. 1.14: Torque density of mechanical gears as function of input speed. Data from [50].

In Fig. 1.14 the same torque density data is plotted as a function of input speed, and it is clearly seen how the rated torque density decreases with increased input speed when looking at all gear types collectively.

1.6.3 Matching technology and application

There is no doubt that promising tendencies have been demonstrated for CMGs and MIPMGs and huge progress has been made since the paper from Atallah et.al. in 2001 that so famously have been accepted in academia as the milestone that marked a true acceleration within the research of the technology. In the latest decade, demonstrators have been build which have yielded great insight into which applications suit CMGs and which aspects proposes a challenge.

The implementation of a magnetic gear into a traction application is very interesting from a torque density perspective and rugged and well-functioning demonstrators have been build and integrated into an actual vehicle. The work done at NASA regarding CMGs with large specific torque indicates, that there indeed could be a future here. However, the high magnetic frequencies seen in these applications poses a challenge when it comes to choice of material and tight integration into their application, where the surrounding materials and stray flux must be considered very carefully. Naturally, the design choices made by NASA eliminates surrounding materials where rotational losses can be induced, but it comes at a cost of expensive materials, and a feasible and rugged design for the ever challenging segment ring still have to be demonstrated in this case.

Marine energy applications is an area where its possible to take advantage of some of the unique features of CMGs. Working demonstrators have been made, and it has also been shown that it is possible to match the torque density of even very torque dense commercially available mechanical gears. Likewise, functional demonstrators have been build and tested for wind turbines, and as a magnetically geared generator have been shown to beat a direct drive PM generator on almost all parameters, these applications could point to a bright future for magnetically geared generators as parameters such as reliability and a minimum of maintenance are critical.

True low speed, high torque applications seems to fit the CMG technology well, and this is why it is interesting for a conveyor application with the operating area seen in the X85H series from Flexlink.

1.7 Research Objectives

The research objective is to increase the knowledge about feasible applications for magnetic gearing technology where the unique properties are utilised.

From literature it is seen that true low speed, high torque applications are likely to be a good match. An example of such a system is found in the X85H series chain conveyor system from Flexlink AB. The conveyor system is a strong study case since it has a very wide application area in an industrial context, hence, every improvement of prior art in this area are likely to have a large impact. This poses the main research question:

Can the advantages of magnetic gearing be utilised to design a compact and energy efficient conveyor drive unit with a wide operating area and how is it integrated with an electric machine and inverter?

To answer the main research question, the following questions are considered:

- How does a practical implementation of a magnetic gear influence the performance of the magnetic gear?
- Do some topologies of a gear/motor combination have distinct advantages compared to others?
- How can the gear/motor/inverter be integrated from a systems point of view?
- How is the system integration and each individual component designed in a commercial feasible way?
- Is the thermal management possible through passive cooling?
- Does the magnetic gearing technology pose any threads to the factory working environment?

By answering these questions the body of knowledge within magnetic gears and industrial drives will be expanded with respect to sweet-spot applications and increase the knowledge about significant factors which influence the magnetic gearing technology when taken from the laboratory to the real world.

1.7.1 Scope of research

This dissertation presents the process of investigating the possibilities for developing a complete drive unit for the X85H chain conveyor system. The drive unit consists of a concentric magnetic gear coupled to a permanent magnet machine which is driven by an inverter designed for the purpose. Different configurations of the MG and PMSM is investigated, but when it comes to the type of MG, only the concentric MG is considered due to the combination of mechanical simplicity and high torque density. These are also the reasons why this type of MG have seen the greatest interest in academia.

The work done by the author is focused at designing the magnetic gear and inverter hardware and the whole concept of integrating these into a drive unit together with a PMSM. The specific electromagnetic design of the PMSM is not done by the author, although the design has been an iterative process between the author and the designer to obtain a good fit between MG and PMSM regarding speed, torque, losses and so on. This is why the specific PMSM design will not be described thoroughly in this dissertation, but details relevant to the system are discussed. Finally, the control design and software development for the inverter is done by a colleague.

1.7.2 Reading guidelines

Chapter 1: Introduction

In the first chapter an introduction to the topic of conveyors are given together with the description of the case study for the dissertation, the X85H chain conveyor system from Flexlink, and the motivating factors for customers when buying these systems are discussed. In extension to a discussion of existing work where magnetic gears have been build for specific applications, it is discussed why magnetic gears are an interesting technology for this application.

Chapter 2: MagCon V1

In the second chapter the first version of a magnetically geared drive unit, MagCon V1, is presented. This chapter is based on Paper A which is appended in the back of the dissertation. The chapter gives a summary of the paper, but it is recommended to read the paper before reading the chapter. MagCon V1 suffered from large rotational losses and large cogging torque. Through tests the locations of these losses are identified.

Chapter 3: MagCon V2

The third chapter presents the second version of the magnetically geared drive unit, MagCon V2. This chapter is based on Paper B, also appended in the back of the dissertation. Initially, a summary of the paper is given, however, as with chapter 2, it is recommended to read the paper before the chapter. Thermal tests, loss separation tests, energy efficiency and core loss models are discussed in this chapter before giving a summary of the performance of MagCon V2 that solved the main problems with MagCon V1, but exposed problems with the stability of the segment ring.

Chapter 4: MagCon V3

This chapter concerns the development and test of the third and final demonstrator of the MagCon drive unit and is the most elaborate chapter in this dissertation. An investigation of different pole- and segment combinations for the CMG is discussed and a new approach to making the segment ring is introduced and demonstrated. This chapter also briefly introduces the inverter that have been designed and integrated with MagCon V3.

Chapter 5: Acoustic noise and vibrations

This chapter is based on Paper C which is the last paper that is appended to this dissertation. The challenges with acoustic noise is addressed thoroughly in this chapter through analytical expressions, finite element analysis and measurements of sound pressure and accelerations on the drive units. Different sources of noise and vibrations are uncovered. Through a collaboration with Portland State University, access is gained to the acoustic data from a magnetic gear designed for marine applications, and the acoustic signature of the MagCon V1 and MagCon V3 drive units are compared to the acoustic signature of this magnetic gear.

Chapter 6: Closing remarks

This final chapter presents the conclusion on the work presented in this dissertation, the scientific contributions and a number of relevant points that are suggested for future work.

2

MagCon V1

In this chapter, the design and results obtained with the first demonstrator, MagCon V1, is presented. The main focus for MagCon V1 is to show, that it is feasible to integrate a magnetically geared drive unit into this specific application, hence the focus is on designing a CMG and PMSM and to integrate these mechanically into the application. The main priority at this point is to exploit how compact the drive unit can be designed, hence torque density of both CMG and PMSM is primary focus points. The final drive unit is seen in Fig. 2.1. The conveyor chain is partly removed to reveal the white sprocket which is placed between two aluminium flanges. The front flange is called the *motor flange* as the PMSM is placed here. The opposite flange is called the *encoder flange* as an encoder is placed here for control and test purposes. The encoder is not visible, but the gray cable below the drive unit goes to the encoder. The gray enclosure behind the PMSM houses the electrical connections for the PMSM.

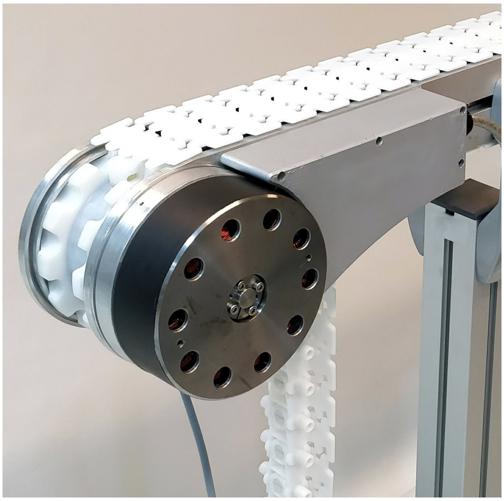

Fig. 2.1: First version of the magnetically geared drive unit: MagCon V1 [24].

2.1 Paper A, summary

Paper A is an extended journal-version of Paper D. Paper A describes the design of MagCon V1. Three different topologies for the integration, shown in Fig. 2.2, are discussed through an initial design stage:

1. Fully integrated: CMG and PMSM is designed as a magnetically geared machine and integrated into the sprocket.
2. External: CMG and PMSM is designed as a magnetically geared machine and placed on the side on a modified version of the original drive unit.
3. Semi-integrated version: CMG is integrated into the sprocket and PMSM is placed next to the gear. PMSM rotor and inner rotor of gear shares a common shaft.

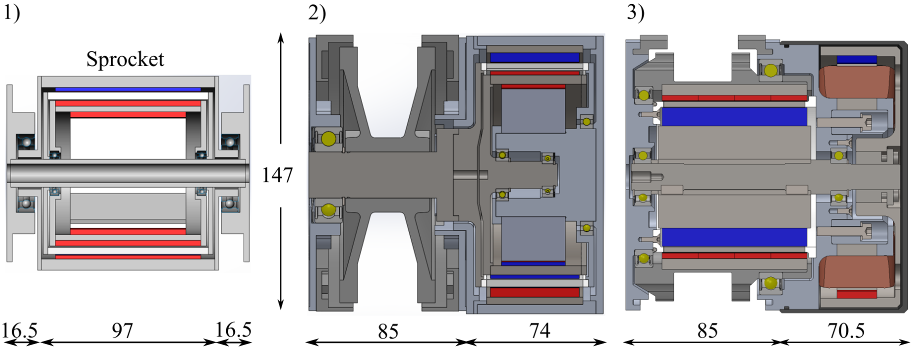

Fig. 2.2: Topologies considered for MagCon V1, figure based on [24].

In the initial design stage each CMG is roughly sized via parameter sweeps in a 2D FE model and the size of the electrical machines are evaluated based on existing, similar electric machines from reputable manufacturers. Option 3 is chosen based on better thermal properties where CMG and PMSM are not directly coupled thermally and better possibilities to remove heat from the PMSM stator. Furthermore, due to the large air gap diameter the stack length of the PMSM can be made very short. Finally, the mechanical structure is the simpler one of the three topologies. At this point in the design phase, the semi-integrated version was considered the most compact drive unit compared to the external one, which was later confirmed when the torque density was evaluated on the physical demonstrator and compared to existing MIP-MGs in literature. The fully integrated version was discarded early in the process, as it was clear that it was not possible due to an unrealistic torque density requirement of 27 Nm/l for the passively cooled PMSM enclosed, and to some degree thermally isolated, inside a CMG.

The CMG and PMSM for the semi-integrated version is finally designed through parameter sweeps in FE models and the demonstrator was manufactured and assembled.

Through tests it was found, that the CMG have a stall torque of 89 Nm at 20 °C which is sufficient for continuous operation, but less than the required peak value of 100 Nm. However, a measured torque density of 142 Nm/l is obtained which is reasonable high compared to what is obtained for CMGs with surface mounted, radially magnetised magnet arrays in literature. The rotational losses are also evaluated, and here a surprising result was obtained. At full speed (4500 rpm for the PMSM), the rotational losses are 1284 W for the CMG and 269 W for the PMSM. This is very high when considering that the peak output power for the drive unit is 700 W at full speed, and the temperature of MagCon V1 is increasing fast at this speed.

By dividing the PMSM rotor magnets into 5 pieces axially the rotational losses in the PMSM was reduced by 75-90 W depending on temperature. From further tests it is shown that the rotational losses are primarily found in the surrounding components, being aluminium flanges and the large bearing that is placed on the outside of the CMG, seen in Fig. 2.2 or "Large bearing" in Fig. 2.3. Because of high induction levels in the CMG and heavy saturation in the outer rotor back iron, the magnetic flux is not contained in the gear, hence large magnetic fields leaks into the surrounding components with large eddy current losses as a results. Also, 522 W rotational loss is found in the active CMG components which is too much.

On top of the large rotational losses, a bad pole/segment combination results in high cogging torque with an amplitude on the inner rotor of 2.5 Nm. This corresponds to 42 % of the maximum torque.

Despite large cogging torque and large rotational losses, thermal DC tests and steady-state thermal test of the PMSM showed that from a thermal perspective, the PMSM was able to operate continuously in the entire operating area, and by mapping the energy efficiency of MagCon V1 in an operating area similar to the operating area in which the Movimot SA37 was tested in section 1.3.1 it is seen, that the peak efficiency of MagCon V1 is 22.2 percentage points better than the Movimot SA37. However, due to the limitation of passive cooling and a surface area that is much smaller compared to the Movimot, the losses are too high to keep the temperature on a safe level.

2.1.1 Mechanical integration

A part of the research objective is to design each component, and the system as a whole, in a commercially feasible way, i.e., make sensible design choices on a component level and to consider the ease of assembly. In the following the mechanical integration and the assembly is presented. Figure 2.3 show an exploded view and name convention for MagCon V1 and Fig. 2.4 show the axial cross section in detail.

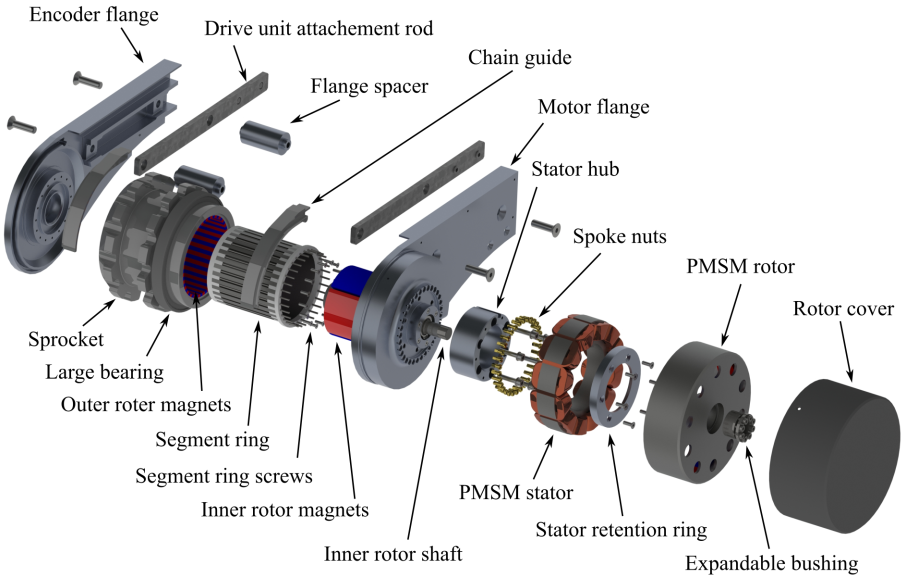

Fig. 2.3: Exploded view of MagCon V1.

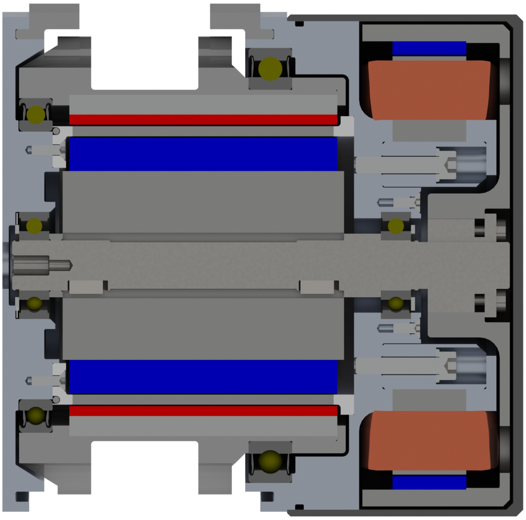

Fig. 2.4: Cross section of MagCon V1.

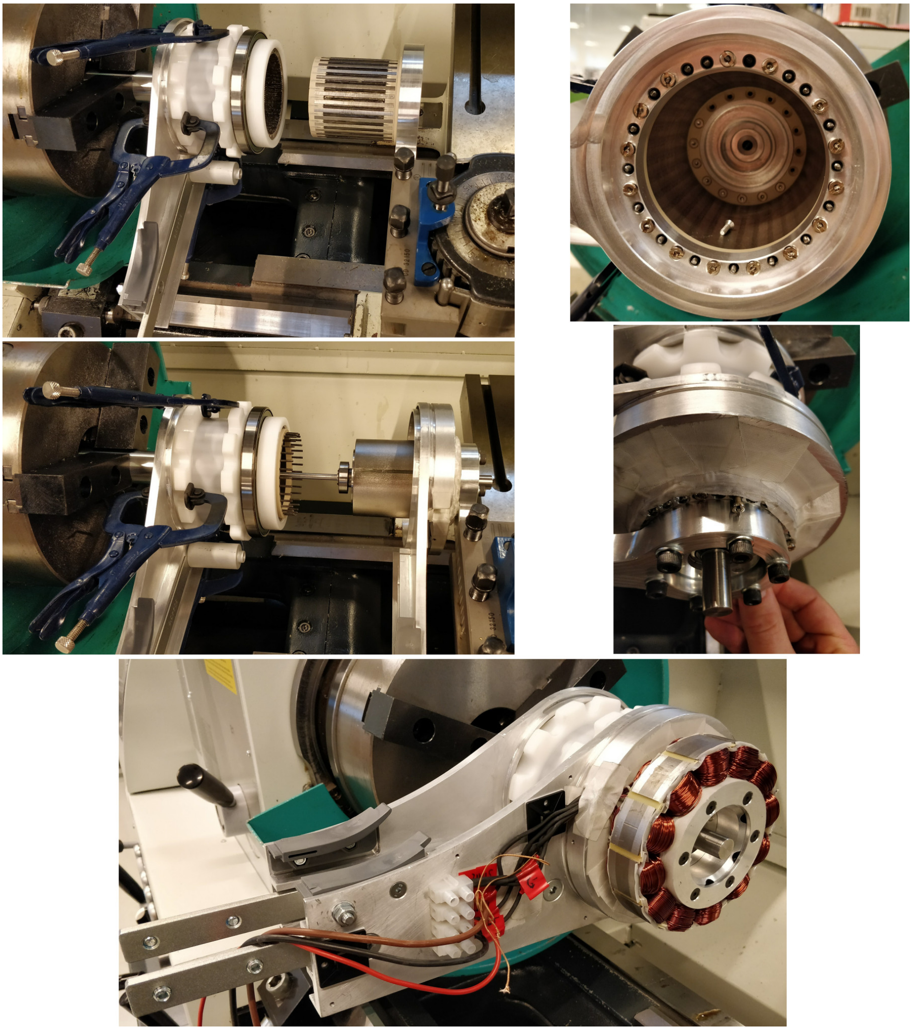

Fig. 2.5: Assembly of MagCon V1.

The main idea behind the mechanical design of MagCon V1 is to minimize the volume. As CMGs have 3 concentric rotors, it is fairly common to see a number of end plates, or end flanges, bolted to the rotors and connected to a common shaft, either a fixed connection or via bearings for the rotating rotors. This approach, however, increase the mechanical complexity, and the end plates takes up space without actively contributing to the main function of the CMG. Hence, it is chosen to suspend the sprocket directly in two large bearings that allows direct access to both segment ring and inner rotor.

Because it has been chosen to use an outer rotor PMSM for MagCon V1, it is necessary to have a part of the motor flange going between the CMG and

PMSM to accommodate the stator and one of the inner rotor bearings. As seen from the investigation of rotational losses in Paper A, this is not desirable. Also, from an assembly point of view, this does pose some challenges.

In Fig. 2.5 the CMG assembly process is shown step by step. To handle the magnetic forces the assembly is done with dedicated assembly tools which are fitted in a lathe. Following steps are taken:

1. Fix sprocket to encoder flange with clamps, Fig. 2.5 upper left.
2. Insert segment ring and mount "Segment ring screws", Fig. 2.5 upper left+right.
3. Mount inner rotor on shaft and insert into motor flange.
4. Insert this sub-assembly into the segment ring / sprocket assembly, Fig. 2.5 middle left.
5. Mount the "spoke nuts", Fig. 2.5 middle right.
6. Mount PMSM stator, Fig. 2.5 bottom, before finally mounting PMSM rotor.

The fact that the sprocket is not self-supporting while inserting the segment ring is sub-optimal, and the fact that the inner rotor must be assembled with the motor flange through a small bearing before inserting the inner rotor into the segment ring introduces the risk of damaging this bearing.

2.2 Summary and conclusions from MagCon V1

MagCon V1 have shown that it is possible to design a compact, magnetically geared drive unit that comes close to the specified stall torque. A number of problems have been described however, and for the next iteration, the following focus areas are prioritised:

- Reduce rotational losses for CMG, PMSM and surrounding components.
- Reduce cogging torque.
- Simplify mechanical design.
- Increase stall torque for the CMG.

In chapter 3 *MagCon V2* the design of MagCon V2 is presented, where these key topics are addressed.

3

MagCon V2

To address the weak points for MagCon V1 described in chapter 2 *MagCon V1*, a significant redesign of both CMG, PMSM and mechanical integration have been undertaken. The process is described in Paper B and the resulting drive unit, MagCon V2, is shown in Fig. 3.1.

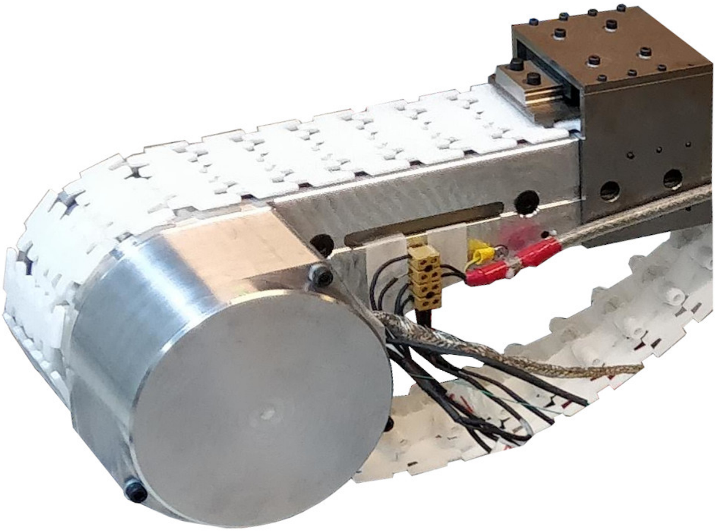

Fig. 3.1: The updated version of the magnetically geared drive unit: MagCon V2 [51].

3.1 Paper B, summary

The rotational losses in MagCon V1 were quite substantial, and to learn more about how to reduce them, the first part of Paper B concerns an experimental investigation of how the losses are affected by reducing the induction level in the gear. This is done by designing a new inner rotor with weaker, buried magnets. Because they are buried in a laminated stack, the risk of inducing eddy current losses in the inner rotor magnets are heavily reduced too. The new inner rotor reduces the stall torque with 52% which is expected. The important takeaway however, is that the rotational losses in all parts except, naturally, the PMSM is reduced significantly with the new rotor. What is really interesting is, that the losses induced in the large bearing are now negligible, and the losses in the motor flange are primarily present in the central part of the flange where the PMSM stator is mounted. To somehow consolidate this experimentally obtained test result into a design constraint that can be used in the design models for the new gear, the 2D FE model of MagCon V1 is modified with the new inner rotor, and the large bearing is added, so that a "safe" peak flux density (B_{pk}) in this bearing can be obtained. It is seen that B_{pk} is reduced from 2.37 T to 0.49 T.

With the new constraint on B_{pk} in the bearing, three options for the new gear design is investigated to evaluate the influence on the stack length of the CMG:

1. p_i = 2, surface mount inner rotor magnets.
2. p_i = 3, surface mount inner rotor magnets.
3. p_i = 3, buried inner rotor in flux focusing V-shape.

To avoid cogging torque, the gear ratio of the CMG with p_i=2 is changed to 14.5:1. For the CMGs with p_i=3 the gear ratio is decreased with approximately 1/3 to 10.67:1 to avoid increasing the fundamental magnetic frequency too drastically. This keeps the rotational losses similar between the 2 and 3 pole pair configuration when similar induction levels are assumed, but requires a larger torque from the PMSM.

Because the CMGs are analysed in a 2D FE model, the target stall torque is increased by 30% to 130 Nm to take 3D-effects into account in a simplified way. This is based on experience from MagCon V1. It is found that option 2 yields the shortest gear with a stack length of 94 mm. Option 3 requires a stack length of 104 mm to meet the target and option 1 requires a stack length of 118 mm.

Naturally, the reduced gear ratios increases the torque requirement to the PMSM. The PMSM from MagCon V1 has a stack length of 22 mm and if this is scaled to fit the updated gear ratios for the new CMGs, the following PMSM lengths are obtained:

$$\text{Option 1} : 22 \cdot \frac{15}{14.5} \approx 23 \text{ mm} \tag{3.1}$$

$$\text{Option 2+3} : 22 \cdot \frac{15}{10.67} \approx 31 \text{ mm} \tag{3.2}$$

This means that the combined length of CMG and PMSM is shorter for option 2 and 3. Despite the longer stack length, the CMG with buried magnets is chosen because it eliminates eddy current losses in the inner rotor magnets which are hard to remove and the magnets are mechanically locked to the rotor, hence the design does not rely on glue to secure the magnets. Finally, simple square magnets can be used.

Until now an ideal geometry of the CMG with 100% fill factor for the outer rotor magnets and square segments has been used for the study. After implementing the real geometry of the outer rotor magnets as well as making adjustments to the segment ring geometry, the stall torque of the CMG is reduced to 125 Nm in 2D FEA, however, at this point in time, the mechanical design was frozen, and so was the CMG design. 125 Nm stall torque in the 2D FE model yields an expected measured stall torque of 96 Nm at 20 °C.

From MagCon V1 it was seen that an outer rotor PMSM is not ideal. It complicates the mechanical design of the drive unit, and a significant amount of eddy current losses are induced in the part of the motor flange where the stator is mounted. Also, an additional cover was needed to shield of the outer rotor, and this cover, to some extend, degraded the heat dissipation from the PMSM. Hence, for MagCon V2 an inner rotor PMSM is introduced as this eliminates the need for having stationary, electrically conducting material between the CMG outer rotor and the PMSM to mount the PMSM stator to. To reduce the eddy current losses in the PMSM magnets, buried magnets in a V-shaped flux concentrating arrangement is implemented, and similar to the inner rotor for the CMG, this further enables the use of simple rectangular magnets which are securely retained inside the rotor laminations. Normally, one of the techniques that are employed to reduce the eddy current loss in surface mount PMSM rotor magnets is to add shoes at the end of the stator teeth which reduces the flux variation seen by the magnets, however, as the magnets are buried in the new PMSM rotor, straight stator teeth may be used which enables the use of concentrated windings on pre-wound bobbins. This simplifies the assembly process compared to needle winding. The final major change made to the mechanical integration is the segment ring which now has a large polymer flange on the end towards the PMSM that extends radially outwards to the aluminium motor flange. This way, the aluminium motor flange is kept out of reach for the magnetic fields from the CMG. The axial cross section of MagCon V2 is seen in Fig. 3.2.

After assembly, the measured stall torque is 98 Nm at 20°C which is 2 Nm more than expected. This may be attributed to the longer stack length compared to MagCon V1 which reduces the influence from the 3D-effects that reduces the difference between 2D FE results and experimentally obtained results.

The critical rotational losses are reduced by a factor of 4.6 compared to MagCon V1 at full speed. This clearly shows that the design changes have had great impact. Despite the large reduction, the rotational loss at full speed is still 339 W, hence, at this point the idea of introducing a *low speed* and a

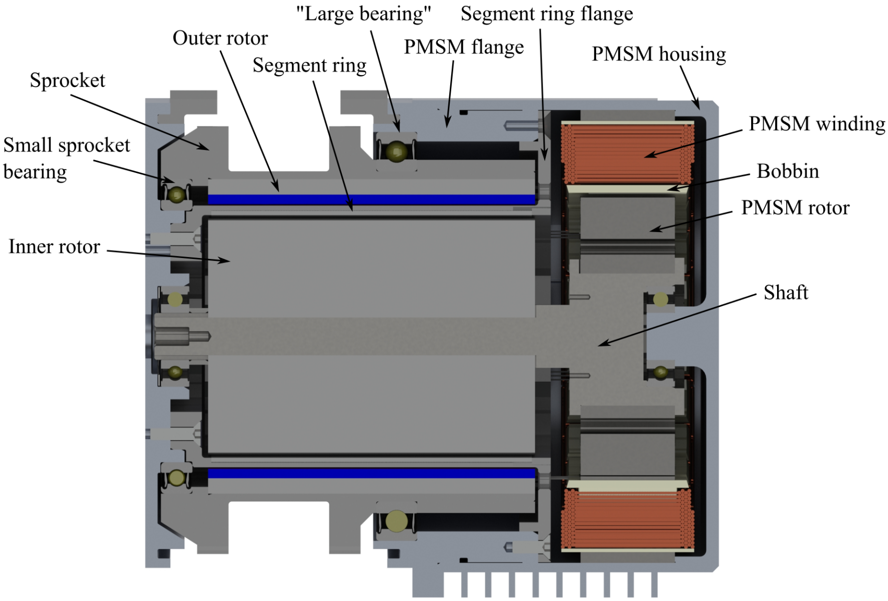

Fig. 3.2: Cross section of MagCon V2.

high speed version of the drive unit is introduced. The exact speed where the transition between the low- and high-speed takes place is as interesting optimisation problem, however, half speed (1600 rpm on PMSM) is chosen, as drive units for lower speeds are most popular with the customers. Also, this is where the torque requirement transitions to a constant value which is seen in the operating area in Fig. 1.6. The demonstrator of MagCon V2 is from now on considered a *low speed* drive unit, and at maximum speed, the rotational losses are 130.9 W, distributed as 42.6 W in the PMSM and 88.3 W in the CMG and remaining parts.

Finally, thermal steady state tests at low, medium and maximum speed at approximately the nominal loads for each speed are presented. At low speed and high load, thermal steady state is reached after 7 hours. The windings reaches the highest temperature which is 93°C. At medium speed, the highest temperature continues to be located in the windings which now reach 103°C. During the first two tests the drive unit performed well, and no problems occurred. However, after 5 hours and 30 minutes in the third test at the highest speed, a sudden increase in segment ring temperature showed that the CMG had failed, and it was found that the segment ring had deformed and made contact with the outer rotor.

After completing the thermal steady state tests, the stall torque and back-emf had not changed which confirmed that no demagnetization had occurred from the elevated temperatures.

3.1.1 Eddy current loss in large bearing and motor flange

In Paper B a design constraint for maximum flux density in the large bearing was deduced from experimental data. To validate this constraint, the test from Paper B where an additional bearing and a dummy aluminium flange is mounted to the sprocket of MagCon V1 is repeated for MagCon V2. Fig. 3.3 shows an additional large bearing placed on the sprocket, and in Fig. 3.4 the dummy-flange which emulates the part of the motor flange that is placed radially outside the CMG is mounted as well. Be aware that in Fig. 3.3 and 3.4 the test-setup is illustrated on MagCon V1, however, it is identical for MagCon V2.

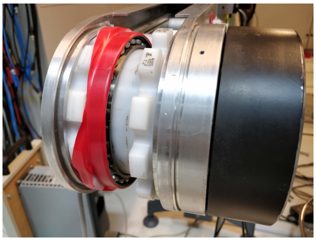

Fig. 3.3: Test of additional loss in large bearing. The figure show MagCon V1, but the test for MagCon V2 is identical [24].

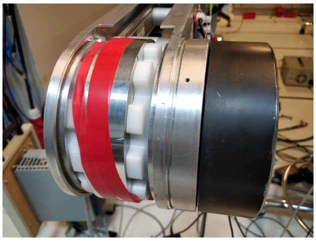

Fig. 3.4: Test of additional loss in dummy flange. The figure show MagCon V1, but the test for MagCon V2 is identical [24].

The result is shown in Fig. 3.5 and it is seen that the rotational loss in all tests are very close. MagCon V2 alone has a rotational loss of 130 W at 1600 rpm in this specific test. In the zoomed view it is seen that the bearing and dummy flange adds some additional loss, however, when both bearing and dummy flange is mounted, the loss is increased with 2.4 W which is seen as satisfactory. This means that the design rule can be applied for future designs.

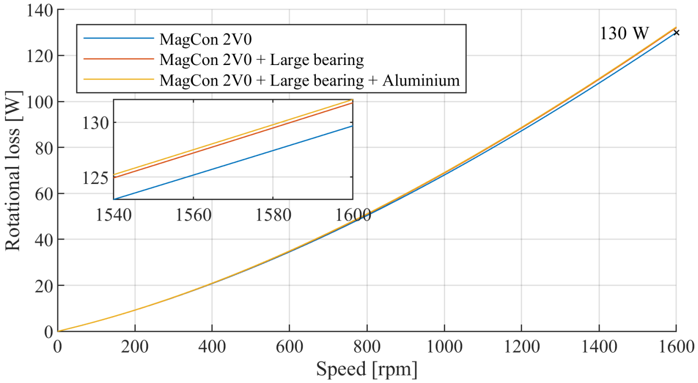

Fig. 3.5: Rotational loss in large bearing and dummy flange.

3.1.2 MagCon V2 efficiency

As for the Movimot gearmotor and MagCon V1, a system efficiency map ("grid-to-chain") is made for MagCon V2 which is shown in Fig. 3.6. As expected from the much reduced rotational losses, a large improvement is obtained compared to the efficiency map presented for MagCon V1 in Paper A. If the contour lines for MagCon V1 in that paper are studied it is seen that with increasing speed, they have a tendency to point slightly upwards. If the contour lines for MagCon V2 in Fig. 3.6 is studied in the same speed range up to 50 rpm it is seen, that they are pointing downwards, e.g., the efficiency is increasing with increasing speed in this range. This show how the rotational losses are less dependent on speed in MagCon V2. The peak energy efficiency measured is 81.3%, and within the operating area a maximum of 77.5% is obtained.

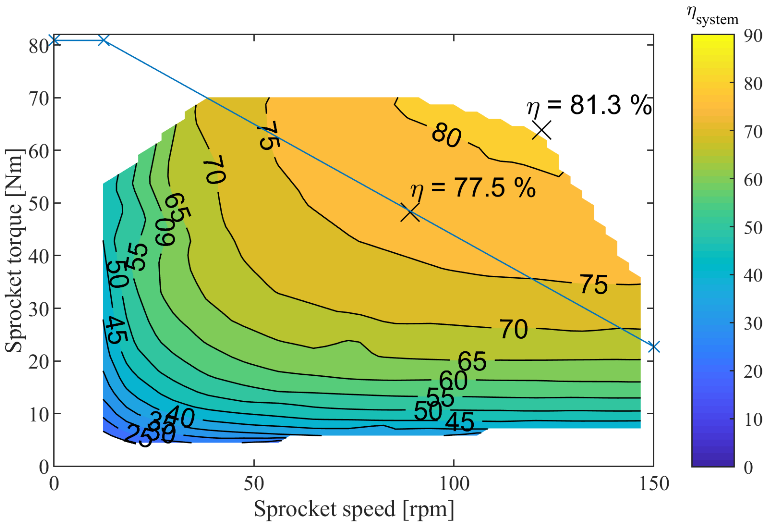

Fig. 3.6: System efficiency with MagCon V2 and Danfoss VLT.

The standby power consumption of the Danfoss VLT is 15 W where the standby consumption for the inverter on the Movimot is 3 W, hence this gives a disadvantage to the MagCon V2 when comparing energy efficiency, especially at light load.

3.1.3 Elaboration on thermal steady state tests

In paper B the results from thermal steady state tests were presented by the highest temperatures at steady state. This chapter elaborates more on the results. Temperatures are measured with thermocouples and the position of some of the thermocouples is shown in Fig. 3.7.

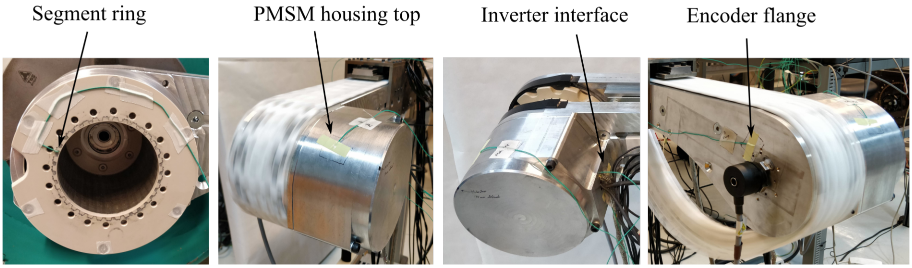

Fig. 3.7: Location of thermocouples during thermal test, thermocouples in PMSM windings not shown.

The thermocouples in the windings are distributed so that the temperature in various positions are evaluated. The exact placement is given by the code in the legend of Fig. 3.8, 3.9 and 3.10, and consist of three parameters: Winding layer, radial placement in stator and whether the thermocouple is placed in the end-winding or in the middle of the stack. Hence, the first entry in the legend for Fig. 3.8 states that the thermocouple is placed in the inner winding layer adjacent to the bobbin, radially in the middle and in the end-winding.

Fig. 3.8 show the test results at 12.2 rpm and 74.4 Nm on the sprocket which is low speed/high torque. As stated in Paper B the 93°C winding temperature is the highest due to the relative high copper losses in this point, but as the winding is thermal class F with a maximum operating temperature of 155°C this is no problem, even so the test is made at 25°C ambient temperature, and not 40°C which is the worst case specification.

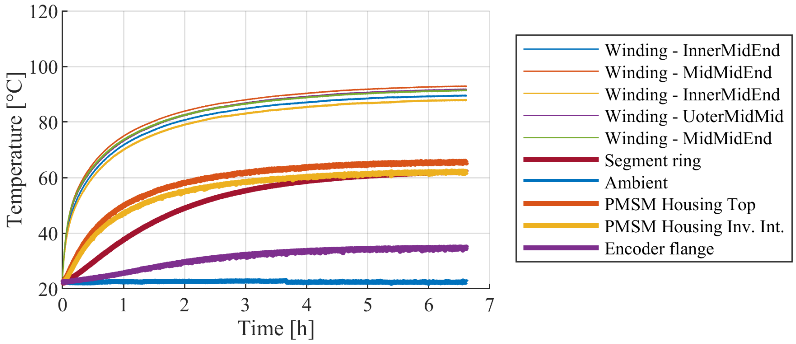

Fig. 3.8: Temperature development during thermal steady state tests of MagCon V2 at 12.2 rpm and 74.4 Nm.

Fig. 3.9 show the results at medium speed and load. It is seen that the copper temperature continues to be the highest at 103°C. The load is only 74% of the load in Fig. 3.8 hence the copper loss is reduced to $0.74^2 \cdot 100 = 54.8\%$, but the core loss has increased with the increasing speed which at this load point yields a higher temperature. Note also how the largest increase in temperature is seen in the segment ring. The segment ring is isolated quite well thermally because it is surrounded by air and suspended in two polymer flanges, hence it is important to keep losses low in this component. Both motor housing and encoder flange have increased by ≈20°C in temperature.

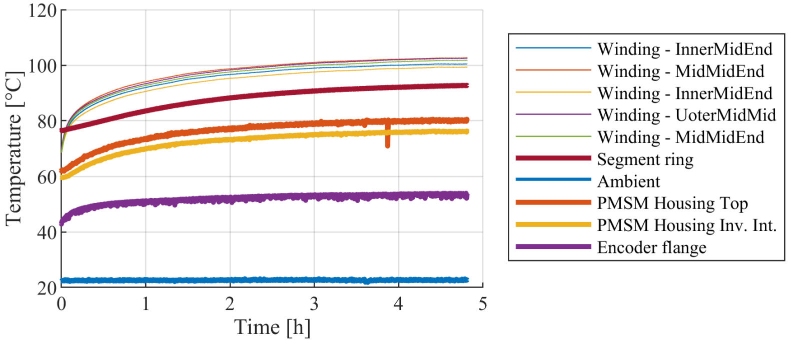

Fig. 3.9: Temperature development during thermal steady state tests of MagCon V2 at 93.7 rpm and 55.3 Nm.

Fig. 3.10 show the results at high speed/low load. This is the load point where the segment ring failed which is seen on the temperature were a sudden increase is seen around 4.5 hours. As already mentioned, the increase in temperature is caused by the segment ring coming into contact with the outer rotor, hereby introducing additional frictional losses. It is also seen that the copper temperature starts to increase again at this point, further indicating that the load on the PMSM increases to deliver the extra power which is lost in the CMG.

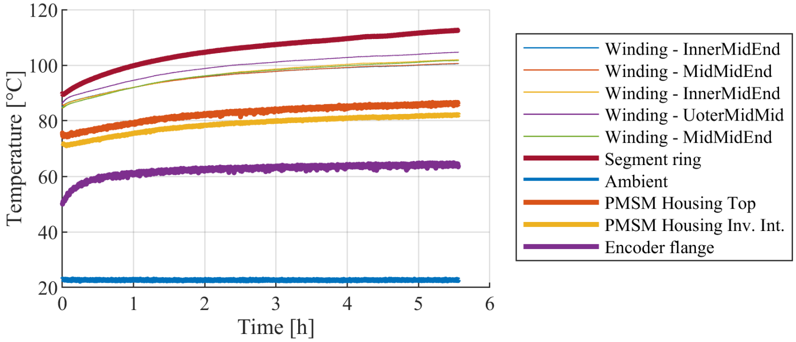

Fig. 3.10: Temperature development during thermal steady state tests of MagCon V2 at 150 rpm and 26.5 Nm.

A note on acoustic noise

During the efficiency tests and the thermal steady state tests it is realised that the level of acoustic noise that is coming from the drive unit seems louder than what is experienced for the Movimot. Especially at higher speed, the perceived sound level seems high enough that it must be taken into account when designing a new drive unit, as acoustic noise will have influence on how the work environment near the conveyor system is perceived.

3.1.4 Modeling of iron- and magnet losses

To learn more about the distribution of the losses in the drive unit, and to improve on the design tools for further development of the MagCon concept, an iron loss model and a simple method for estimating eddy current losses in the magnets are introduced.

Iron losses

The Bertotti three-term equation Eq. (3.3) [52] is a classic method to estimate the specific iron loss, P_{Spec} [W/kg], in laminations with sinusoidal flux density variation. It describes P_{Spec} by three terms that represents hysteresis losses, eddy current losses and excessive losses. The coefficients k_h, α, k_e and k_{ex} are coefficients that can be found by curve-fitting iron loss data from the lamination manufacturer with Eq. (3.3). The frequency of the varying flux density is given by f and B_{pk} is the peak flux density.

$$P_{SpecSine} = k_h f B_{pk}^{\alpha} + k_e f^2 B_{pk}^2 + k_{ex} f^{\frac{2}{3}} B_{pk}^{\frac{2}{3}} \tag{3.3}$$

Because Eq. (3.3) describes P_{Spec} in terms of a sinusoidal variation in B, the accuracy will decrease when the B-waveforms deviates from a perfect sinusoid. In this case, [52] further presents the generalised equation, Eq. (3.4), that yields a more accurate result.

$$P_{SpecGen.} = k_h f B_{pk}^{\alpha} + \frac{k_e}{2\pi^2}\left(\frac{dB}{dt}\right)_{rms}^{2} + \frac{k_{ex}}{(2\pi^2)^{\frac{3}{4}}}\left(\frac{dB}{dt}\right)_{rms}^{\frac{2}{3}} \tag{3.4}$$

Both Eq. (3.3) and (3.4) describe P_{Spec} in laminations that sees uni-directional variation of B, and in the Epstein test frame used to obtain the loss data, most of the lamination material indeed sees uni-directional flux. However, in many real applications, some areas of the lamination are seeing what has become known as *rotating flux*. In Fig. 3.11 the B-locus is shown in different positions in the stator of the PMSM designed for MagCon V2. The B-locus in the two figures have been rotated and are shown in terms of the major- and minor axis, hence the direction cannot be related directly to the geometry shown.

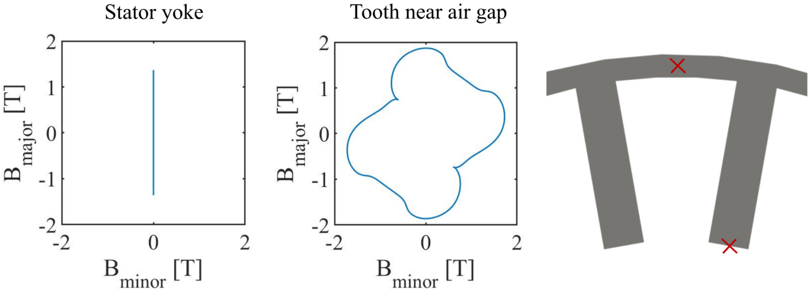

Fig. 3.11: The B-locus changes depending on where in the stator it is evaluated.

To the left in Fig. 3.11 the B-locus at the red X in the stator yoke is shown, which is primarily uni-directional. The middle figure shows the B-locus at the tip of the teeth near the air gap, and here a loop is formed by the B-vector during one electrical period. In [53] a method is presented where Eq. (3.3) is used to evaluate P_{Spec} from the flux density variation on both the *minor* and *major* axis of this loop, and the total specific loss is then given as the sum of the two. To continue to take harmonics of the B-waveform into consideration, $P_{SpecSine}$ is substituted with $P_{SpecGen.}$ from Eq. (3.4), hence the final expression for obtaining the specific iron loss including rotational losses is given by Eq. (3.5).

$$P_{SpecRot} = P_{SpecRot}(B_{pk,major}) + P_{SpecRot}(B_{pk,minor}) \tag{3.5}$$

Geometry is another factor that has influence on the iron loss calculations. The magnetic properties of electrical steel is obtained through heat treatment, and when the final lamination geometry is stamped from the electrical steel sheets, the plastic deformation deteriorates the magnetic properties along the edges. Hence, the Epstein frame gives loss data that fits a stack of laminations build from 30 mm wide strips. By testing lamination strips of different width, [53] derives a cutting factor, K_{cut}, given by Eq. (3.6) to adjust the calculated P_{spec} as a function of lamination width.

$$K_{cut} = C_1 + \frac{C_2}{width} \tag{3.6}$$

From a test where M400-50A electrical steel is used, [53] finds that $C_1 = 0.89$ and $C_2 = 3.0$. The laminations used for the demonstrators presented in this dissertation are made from laser cut M235-35A electrical steel, hence, the best result for this correction factor would be obtained by fitting Eq. (3.6) to a number of new data points obtained from tests with laser cut strips in this material. In [54] a study on the influence on iron loss from laser cutting and stamping is studied. The iron loss for several types of electrical steel in 0.1 mm, 0.2 mm and 0.35 mm thickness that has been laser cut and stamped is measured via Epstein frames and by a single sheet tester. The results show that there is no noticeable difference between the two cutting methods, hence the correction factor is used with the coefficients C_1 and C_2 found in [53]. Fig. 3.12 shows K_{cut}. It is evident that the cutting effects have large influence in small machines where narrow details are present in the laminations.

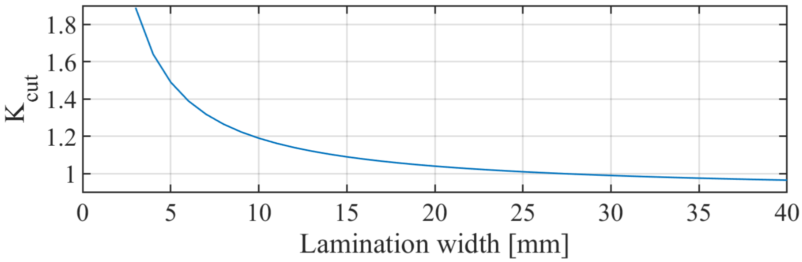

Fig. 3.12: Correction factor K_{cut} to adjust loss calculations for with of electrical steel.

To find the actual iron loss, the specific iron loss is multiplied by the mass of the laminations. The final factor that is taken into consideration for the iron loss model is the stack factor of the laminations. The mass of a stack of a given length is somehow proportional to the stack factor, and in the linear region of the magnetisation curve, the flux density in the laminations at a certain flux is inversely proportional to the stack factor. By assuming that the iron loss is proportional to the square of the flux density, the following is considered true where SF is the stack factor:

$$P_{iron} \propto \frac{1}{SF^2} \cdot SF = \frac{1}{SF} \tag{3.7}$$

The B-waveform for estimating the iron loss for the PMSM and CMG is obtained from each element in the FE model. This gives the opportunity to take local variation in B into account. The total iron loss is then given as the sum of iron loss in all n elements as described by Eq. (3.8).

$$P_{iron} = \sum_{n=1}^{k} \frac{P_{SpecRot,n} \cdot K_{cut,n} \cdot A_{elem,n} \cdot l_{stack} \cdot \rho}{SF} \tag{3.8}$$

where $A_{elem,n}$ is the n^{th} element area [m^2], l_{stack} is the stack length [m] and ρ is the density of the electrical steel [kg/m^3] in an FE model with k elements. The lamination width used to evaluate K_{cut} is specified in a setup file for the iron loss calculation. As an example, the PMSM stator is divided into yoke and teeth, as the yoke and teeth have different widths. From the geometrical position of each element it can be determined if it element belongs to the yoke or a tooth, which then defines the appropriate lamination width.

Magnet losses

The eddy current losses in the magnets are simply estimated from the eddy current term in Eq. (3.3) where k_e is given by (3.9), [55].

$$k_{e,mag} = \frac{\sigma \pi^2 d^2}{6\rho} \tag{3.9}$$

Where σ is the electrical conductivity of the magnet [S/m], d is the limiting dimension [m] and ρ is the density of the magnet material [kg/m^3]. Hence, the magnet loss, P_{mag}, is given by Eq. (3.10) where the specific loss is multiplied by the mass of the magnet, m_{mag} [kg].

$$P_{mag} = k_{e,mag} f^2 B_{pk}^2 m_{mag} \tag{3.10}$$

The flux density in the magnet is evaluated as the mean flux density in all elements of the magnet.

The losses of the PMSM obtained by the models are shown in Fig. 3.13 and in Fig. 3.14 the total rotational loss from the model is compared to the estimate from MotorCAD and experimental test results. MotorCAD is the commercially available software that has been used to design the PMSM. The loss calculation in MotorCAD does not take a factor like K_{cut} into consideration but it is possible for the user to add a *buildfactor*. The designer of the PMSM added a build factor of 1.5 to obtain the best fit to the experimental data.

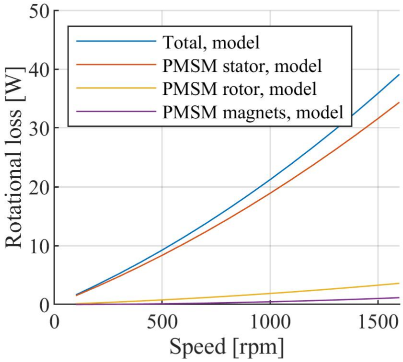

Fig. 3.13: Loss in PMSM components from iron- and magnet loss model.

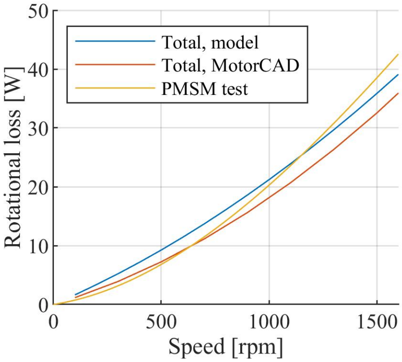

Fig. 3.14: Comparison of modelled losses to results from MotorCAD and experimental test.

In Tab. 3.1 the calculated rotational loss is shown for the PMSM when using the dB/dt method on B_{norm}, when rotational losses are taken into account as in Eq. (3.5) and when this result is adjusted with K_{cut}. It seen that the rotational losses add 10.8%, and on top of that, 47.9% is added from K_{cut}. The correction for stack factor is used for all the results.

dB/dt loss, B_{norm}, SF	23.16 W	
dB/dt loss, rotational, SF	25.66 W	+10.8%
dB/dt loss, rotational, K_{cut}, SF	37.96 W	+47.9%

Table 3.1: Influence of rotational loss and K_{cut} on the loss calculation for the PMSM.

When comparing total loss in Fig. 3.14 it is seen that the result of the iron- and magnet loss model described in this section is fairly close to both MotorCAD and test results and it is deemed satisfactory. At 1600 rpm the estimated magnet loss is 1.15 W. At this speed, MotorCAD estimates 0.42 W, however, the result is seen as satisfactory for such a simple model.

Fig. 3.15 show the modelled loss distribution in the CMG components of MagCon V2 where a total of 26.5 W of loss is induced at 1600 rpm. It is seen that the majority of losses are found in the outer rotor back iron and the segment ring. Losses in the inner rotor magnets are almost zero and iron loss in the inner rotor as well as the losses in the outer rotor magnets are almost equal and very small.

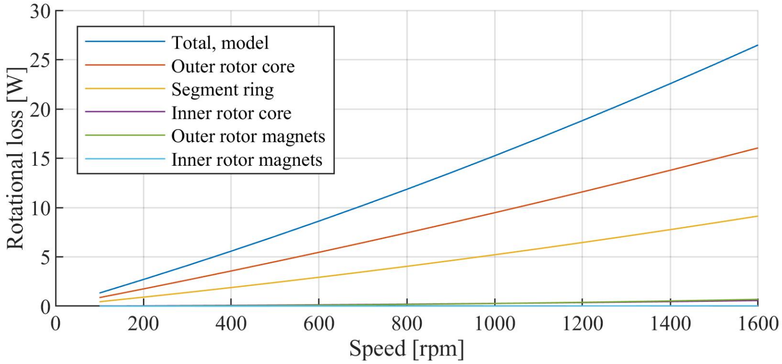

Fig. 3.15: Modelled loss distribution in the CMG components of MagCon V2.

As earlier mentioned, Paper B states that 130.9 W of rotational loss is induced in MagCon V2 at 1600 rpm. The measured rotational loss in the PMSM at this speed is 42.6 W, hence there are 88.3 W in the remaining components of MagCon V2 from which only 26.5 W should be in the CMG according to the model. In Tab. 3.2 the different loss components that have been discussed for different components in MagCon V1 and MagCon V2 so far is presented.

According to data from SKF, up to 14 W is present in the new "small sprocket bearing" because it does not have a low friction seal, and from tests it has been shown that 2.4 W is induced in the large bearing. From the loss-separation tests done for MagCon V1 it is known that losses are induced in the encoder flange. If an equal flux density is assumed in the encoder flange for MagCon V1 and MagCon V2, the loss curves for MagCon V1 can be used to estimate the loss in this flange. The magnetic frequency of the inner rotor for MagCon V2 at 1600 rpm corresponds to that of MagCon V1 at 2400 rpm, and here, 21.9 W is induced in the encoder flange.

Source	Loss [W]
MagConV2 - PMSM (measured)	88.3
CMG iron loss, model	-25.8
CMG mag. loss, model	-0.7
Small sprocket bearing	-14
Large bearing	-2.4
Encoder flange, est.	-21.9
Not accounted for	23.5

Table 3.2: Evaluation of sources for rotational losses in MagCon V2.

There are still 23.5 W that is not accounted for. Some of this loss may be found in the circulating current that goes through the electrically conducting circuit consisting of flanges, inner rotor bearings, inner rotor shaft and flange spacers, which is mentioned in Paper A. Another source of error is likely found in the the iron loss calculation. In Fig. 3.12 it is seen that K_{cut} is increasing rapidly with decreasing width of the laminations. In the iron loss models, the minimum width used to evaluate K_{cut} is 3 mm to avoid too much extrapolation, as the data used to develop K_{cut} did not include lamination strips below 10 mm. However, especially in the segment ring, narrow sections of laminations are found. The bridge used to connect the segments is only 0.6 mm thick, hence it must be expected that the loss characteristic of this material is severely deteriorated.

The iron- and magnet loss models showed satisfactory accuracy for the PMSM, and several factors will have influence when trying to estimate the losses in the remaining parts of the drive unit. Hence, the loss models are implemented in the development process of the next version of the MagCon drive unit.

3.1.5 Mechanical integration

The mechanical design of MagCon V2 is much simplified compared to MagCon V1 which should be apparent from the exploded view in Fig. 3.16. Fewer components and screws are used. Following steps are taken during assembly:

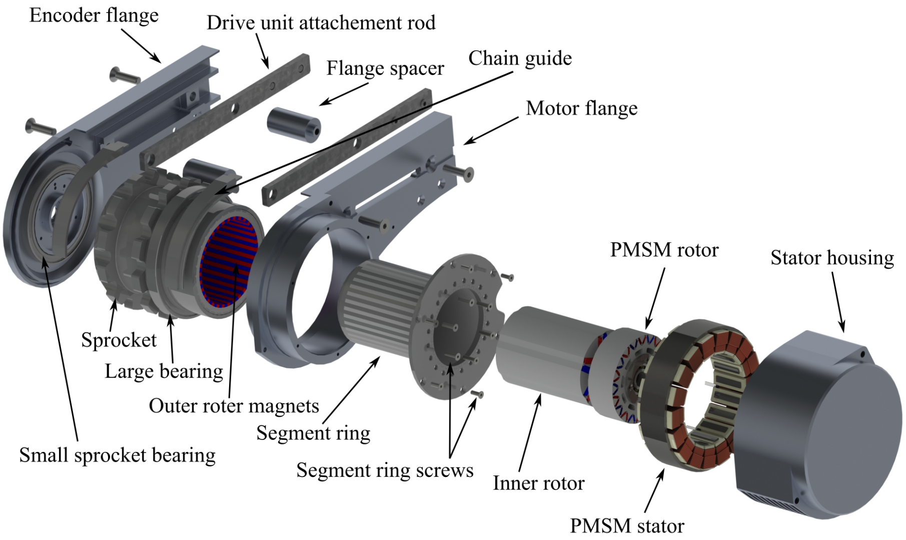

Fig. 3.16: Exploded view of MagCon V2.

1. Mount sprocket between aluminium flanges and keep flange together with flange spacers.
2. Insert segment ring and mount "Segment ring screws".
3. PMSM stator is shrink fit into stator housing.
4. Insert shaft with CMG inner rotor and PMSM rotor into PMSM stator.
5. Slide this assembly into rest of CMG and fix PMSM housing with screws.

3.2 Summary and conclusions from MagCon V2

MagCon V2 solves the main problems of MagCon V1, being high rotational losses and large cogging torque. Further, the mechanical design is much simplified. The stack length of CMG and PMSM combined has been increased by 32 mm, however, the implementation of an inner rotor PMSM enables a more tight packaging of MagCon V2, hence the total width of MagCon V2 is only increased by 27 mm.

Thermal tests show that MagCon V2 is operating very well in a large part of the operating area and the energy efficiency has been improved greatly compared to MagCon V1, however, at high speed operation there is a thermal problem with the segment ring and during thermal tests as well as efficiency tests, acoustic noise which is noticeably higher than what is experienced for the Movimot gearmotor has been observed.

Up until this point, the CMG have been designed based on the remanent flux density for the magnets at 20°C, hence, the reduced magnet strength at elevated temperatures must be taken into account. Finally, as a PMSM is used, the drive unit must be driven by a frequency converter, hence to obtain a complete drive unit solution that fits into to the ecosystem of Flexlink, a frequency converter must be designed. The following focus points are prioritised during the development of the next demonstrator:

- Focus on stability of segment ring at elevated temperatures.
- Improve on acoustic noise.
- Design CMG for steady state temperatures.
- Develop first iteration of frequency converter for the drive unit.

In chapter 4 *MagCon V3* the above mentioned parameters are taken into consideration during the design of MagCon V3.

4

MagCon V3

In this chapter the development of MagCon V3 will be presented. Besides dealing with the main challenges for MagCon V2, this chapter will briefly introduce the concept and main ideas behind the inverter that has been designed for the drive unit. Because the CMG is driven by a PMSM, an inverter is required, and because the work presented in this dissertation concerns the design of a conveyor drive unit *system*, a first iteration of an inverter is designed which meets the expectations and requirements from Flexlink to show how this may be integrated.

Due to the challenges met for the segment ring in chapter 3 *MagCon V2* where acoustic noise were observed at a level that can be problematic for the work environment and problems with the stability of the segment ring at high speed where the temperature is increasing, it is desirable to increase the mechanical strength and stiffness of the segment ring. In [36] it was shown that the acoustic noise of an MIPMG was significantly decreased by closing some venting holes in the MIPMG, which strongly indicated that the source of the sound came from the inside of the MIPMG. It was further shown that the frequency spectrum of the magnetic forces acting on the segment ring to a large degree coincided with the frequency spectrum of the acoustic noise, and by increasing the stiffness of the segment ring, experimental data showed a decrease in the sound pressure level. It makes sense that a large part of the acoustic noise comes from the segment ring, as this is the component with the least stiffness and it is excited from two sides.

For MagCon V1 and MagCon V2 the segment ring laminations were suspended in a polymer cage made from PEEK. This material was chosen because it has a high tensile stress without the need of adding any reinforcement in the form of e.g. glass fiber, hence when the material is machined from solid stock to make the cage, the risk of the parts warping due to internal stresses being released is reduced. Also, the thermal properties of PEEK with the very high operating temperature of 260°C [56] is interesting. However, PEEK is very expensive, and to make the chances for commercial success for MagCon V3 as good as possible, the manufacturing cost must be kept in mind.

The idea of moulding the cage and segment ring flange directly onto the laminations stack in an injection moulding process, which was mentioned in both Paper A and B, is implemented for MagCon V3. Besides being a cost effective process, this further offers the advantage of using fiber reinforced polymers as, ideally, no significant amount of post-injection processing in the form of milling or turning has to be done. Nylon reinforced with 50% glass fiber (PA-66 50GF) is chosen [57]. This has a tensile modulus of 15.5 GPa compared to 4.2 GPa for PEEK, hence the stiffness is essentially increased by a factor 3.7. Furthermore, the high fiber content gives a tensile stress of 220 MPa compared to 116 MPa for PEEK. Besides the introduction of a stiff and strong material for the segment ring cage, the radial thickness of the segments is increased with 33% from 3 to 4 mm.

In [58] the stiffness of the segment ring is improved by inserting non-magnetic support rings into the segment ring stack. Where the segments are only connected by a thin bridge (0.6 mm thick for MagCon V2), these support rings have the full height of the segments which improves the stiffness. This technique is also pursued in the development of MagCon V3, and because the cage is added to the segment rings in an injection moulding process, it is easy to make one version of the segment ring which have a full stack, and another version where the stack is split on the middle, and a glass fiber ring is inserted. This is shown in Fig. 4.1 where a section is cut out of the segment ring to reveal the 4 mm wide light orange glass fiber ring. The dark gray is the PA-66 50GF and the light gray is the laminations. The glass fiber ring has elongated holes that allows the PA-66 50GF to flow and connect the two halves of the segment ring. Having both a full-stack and a split-stack version enables a direct comparison of the two solutions during the test phase.

To reduce the loss in the segment ring, 0.2 mm laminations is introduced for MagCon V2, where both MagCon V1 and V2 used 0.35 mm. Finally, to improve the robustness of MagCon V3 towards mechanical tolerances, both air gaps of the CMG is increased from 0.4 mm to 0.5 mm.

4.1 Magnetic re-design of CMG

A substantial effort was put into the design of the CMG for MagCon V2 and with a measured stall torque of 98 Nm at 20°C magnet temperature, the stall torque was still slightly off target, especially if elevated temperatures are considered. As the air gap lengths in MagCon V3 are increased, it is even more difficult to increase the stall torque further with the current CMG design choices. Until this point the outer rotor magnets have been radially magnetized due to the simplicity where only *one* unique magnet is required, and because a radially magnetised array is relatively easy to glue onto the back iron. However, to continue to increase the stall torque without increasing the stack length even further, a Halbach magnet array on the outer rotor

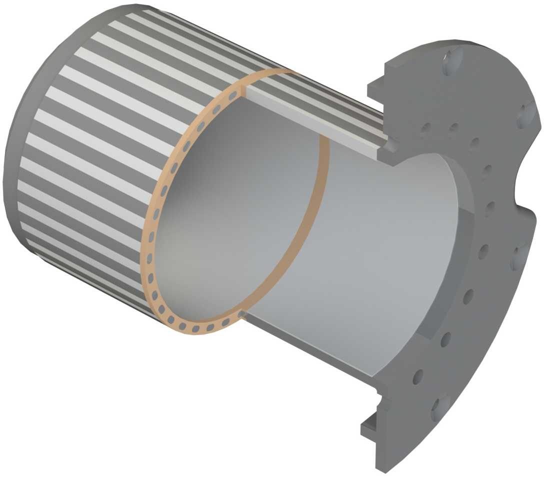

Fig. 4.1: Segment ring where a section is cut out to show the glass fiber ring that is inserted.

is considered necessary to increase the magnetic field strength on the outer rotor. The Halbach array is implemented with 4 segments per pole pair as indicated by the gray arrows on the outer rotor magnets in the magnified view of Fig. 4.2. It is not necessarily a requirement to change the magnet arrangement on the inner rotor, as the main constraint for the design of a CMG in this specific implementation is to limit the flux density in the large bearing outside the sprocket. Because this limit can easily be obtained by the current buried magnet structure which is easy to assemble, mechanically robust and limits eddy current loss in the magnets, this is not changed.

Like MagCon V1 and MagCon V2, the new CMG is designed through a number of parameter sweeps in a 2D FE model. Through all sweeps, a stack length of 100 mm is used which will yield a conservative result that takes the width of the glass fiber ring into account. In reality, as the inner and outer rotor are 104 mm long, the reduction in stall torque due to the glass fiber ring is likely less than indicated by the 2D FEM results due to spreading magnetic fields in the gap between the two segment ring stacks. The starting point for the other important dimension of the CMG is given in Tab. 4.1. A visual representation of the parameters are shown on a cross section of the CMG in Fig. 4.2.

The segment duty ratios describes the ratio of lamination to air on the inner- and outer diameter of the segments. For the inner radius it is given as Eq. (4.1), and the same concept applies to the duty ratio at the outer diameter.

$$D_{seg,i} = \frac{\beta_{steel}}{\beta_{steel} + \beta_{air}} \tag{4.1}$$

Outer rotor magnet height, H_{magOR}	2.5 mm
Outer rotor back iron thickness, $H_{backironOR}$	5 mm
Outer rotor magnet clearance	0.26 mm
Segment thickness, H_{seg}	4 mm
Segment duty ratio, $D_{seg,i}/D_{seg,o}$	0.6/0.25
Segment bridge height	0.6 mm
Air gaps	0.5 mm
Stack length	100 mm
Magnet temperature	20 °C
Magnet grade, outer rotor rad/tan	N40UH/N38EH
Magnet grade, inner rotor	N45SH
Inner/outer rotor material	M235-35A
Segment ring material	B20-AT1500

Table 4.1: Initial dimensions of MagCon V3.

The two notches at the outer diameter of the segments are added to obtain a mechanical interlock to the polymer cage between the segments. The notches are not included in the duty ratio, but have a fixed height and width of 0.5 mm and are added after the "main trapezoidal shape" has been drawn. The distance between the magnet corners in the bottom of the V-shape and between two neighbouring magnets near the air gap is 0.5 mm, and the magnet corner closest to the air gap is at a fixed radial distance of 2 mm from the air gap.

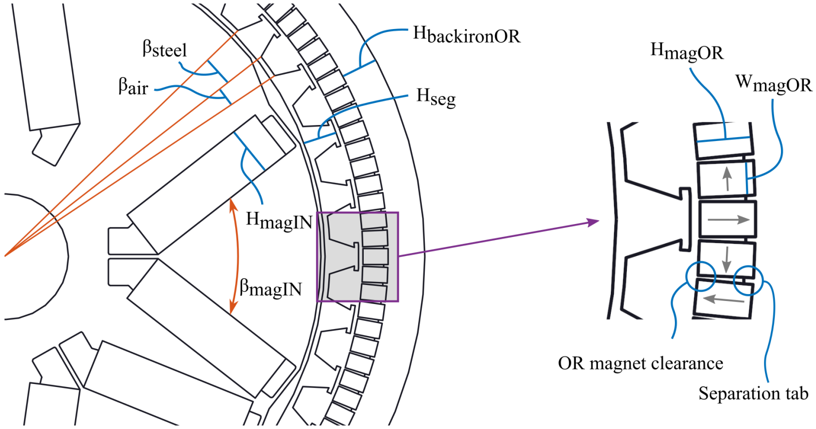

Fig. 4.2: Relevant parameters for the sweep.

In [39] it was shown that the thickness of the inner rotor magnets have a large influence on the stall torque of a magnetic gear, but due to the main limitation on B_{pk} in the large bearing for the MagCon concept, there is a clearly defined limit to the strength of the inner rotor magnets. Hence, the first sweeps concerns the inner rotor magnets thickness, H_{magIN}, and angle, β_{magIN}, with the aim of getting as close as possible to B_{pk} in the large bearing while still considering mechanical aspects and the amount of magnet used.

Fig. 4.3 show the result for B_{pk} and Fig. 4.4 show the stall torque.

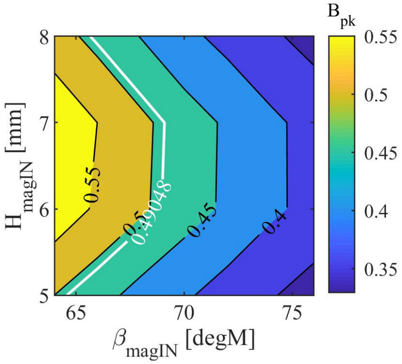

Fig. 4.3: B_{pk} in large bearing as function of inner rotor magnet thickness and angle.

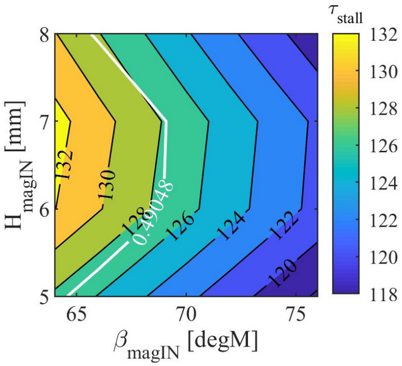

Fig. 4.4: Outer rotor stall torque as function of inner rotor magnet thickness and angle.

The white isocurve show the limit for B_{pk} in the large bearing. All design points to the right of this line are feasible design points which is evident from Fig. 4.3. It is seen that the stall torque increases together with the flux density in the large bearing, and from these plots, a magnet thickness of 6-7 mm and and an angle of 69 degree would be the best choice.

However, in Fig. 4.5 and 4.6 that shows the CMG with a 6 mm magnet thickness together with 70 and 76 degree magnet angle, it is seen, that the amount of material in the lamination around the shaft is getting thinner with decreasing magnet angle. At 70 degree angle the laminations are 3.5 mm thick and at 76 degrees they are 5 mm thick, and the configuration with a 76 degree angle is chosen even though a lower stall torque is obtained.

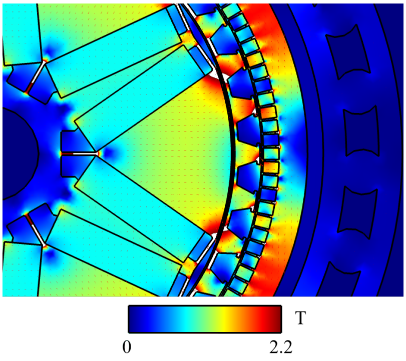

Fig. 4.5: β_{magIN} = 70 degrees.

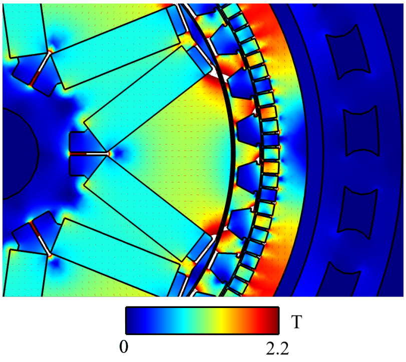

Fig. 4.6: β_{magIN} = 76 degrees.

There is not much difference in stall torque between a 6 or 7 mm thick inner rotor magnet. To decide on the magnet thickness, the mass of the inner rotor magnet is studiet, this is illustrated in Fig. 4.7, and here it is seen, that less magnet is used with the 6 mm thick inner rotor magnet. The stall torque only decrease 0.23 Nm while 5% magnet mass is saved by choosing a 6 mm thick magnet.

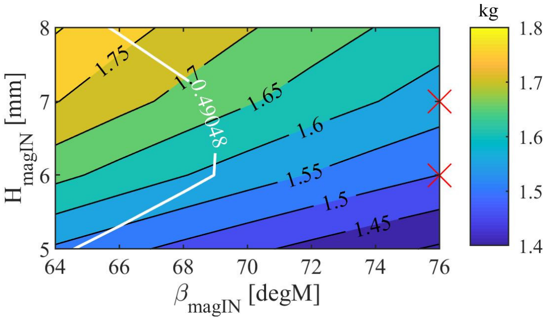

Fig. 4.7: Total magnet mass in CMG as function of inner rotor magnet thickness and angle.

With the choice on magnet layout on the inner rotor, B_{pk} in the large bearing is now below the limit. This means that the outer rotor back iron thickness can be made thinner which will allow a larger air gap diameter to increase the stall torque. As permeability of the outer rotor magnets is close to that of air and because they are included in the main flux path for the inner rotor magnet, the height of these have influence on B in the outer rotor back iron as well. Hence the next sweep investigates the combination of $H_{backironOR}$ and H_{magOR}. In Fig. 4.8 the result regarding stall torque is seen, and in Fig. 4.9 the torque per total magnet mass of the CMG is seen.

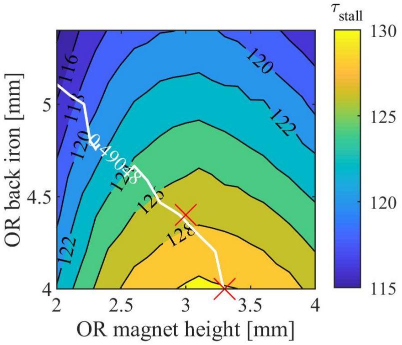

Fig. 4.8: Stall torque as a function of outer rotor magnet height and outer rotor back iron thickness.

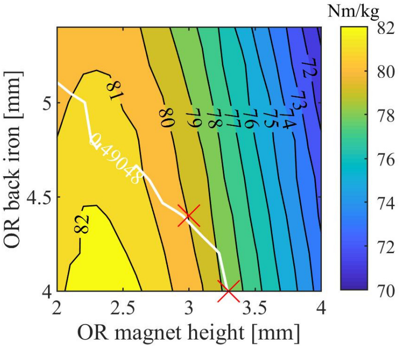

Fig. 4.9: Torque pr. kg. of total magnet mass as a function of outer rotor magnet height and outer rotor back iron thickness.

As for the configuration of the inner rotor poles it is an engineering tradeoff. Two points are interesting, namely a point with 4.4 mm back iron and 3 mm thick magnets which yields 127.5 Nm and another point with 4 mm back iron and 3.3 mm magnets, which yields 130 Nm. Arguments can be made for both configurations, however, 3 mm magnets and 4.4 mm back iron was chosen, mainly due to the lower magnet height compared to the width of only 1.85 mm, which is easier during gluing, and because of the better utilisation of magnet material, as the torque per mass of magnet is higher for this configuration.

The third sweep regards the inner and outer segment duty ratio to see if the design choices so far have had any influence on the optimum value here. The result is seen in Fig. 4.10 where an optimum is found with $D_{seg,i}$ = 0.6 and $D_{seg,o}$ = 0.25. Here, it must be noticed that the large bearing is removed from the model, and because $D_{seg,i}$ and $D_{seg,o}$ is not changed, B_{pk} in the bearing will not change from prior simulations either. However, by removing the bearing, the 2D FE results show a slight reduction of the stall torque from 127.5 Nm to 126.15 Nm.

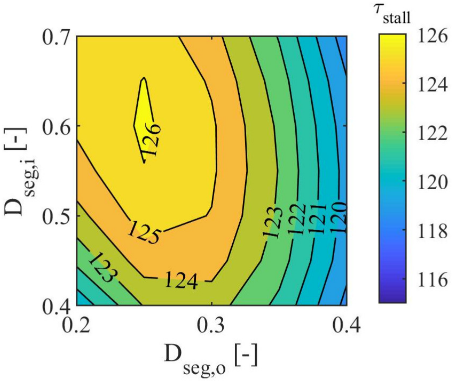

Fig. 4.10: Stall torque as a function of $D_{seg,i}$ and $D_{seg,o}$.

In Fig. 4.2 it is seen that the outer rotor back iron features small *separation tabs* which serves the purpose of guiding the magnets while glueing them and also to increase the glue area to increase the strength of the bond. The drawback of having these separation tabs is that air pockets are introduced between the magnets in the Halbach array, and this reduces the stall torque of the CMG. Fig. 4.11 show how the stall torque is changed as a function of the outer rotor magnet clearance. Clearly, the clearance between the magnets should be kept as small as possible. For MagCon V3 the clearance between the magnets is 0.26 mm, which is chosen so that the separation tab is 0.35 mm wide. This choice is taken because the laminations in the outer rotor are 0.35 thick, and when stamping laminations, no details should be narrower than the thickness of the lamination.

Finally, the magnetic design is tested for demagnetisation. The topic of

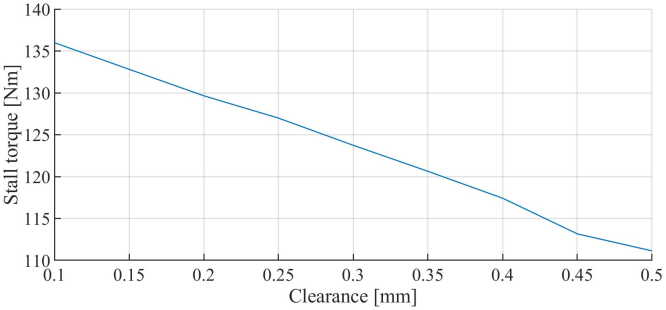

Fig. 4.11: Influence of air between magnets on the stall torque.

demagnetization can be rather complex. Here, a relatively simple approach is taken, where the norm of the magnetic field, H_{norm}, in the magnets is used to determine if there is a risk of demagnetization. By doing this, a worst case scenario is considered, where it is assumed that H_{norm} is always working directly against the magnet.

From the thermal steady state tests of MagCon V2 the temperature of the outer rotor back iron is the highest at full speed, and here a temperature of 79°C has been measured at an ambient of 23°C. Hence to add some margin at the maximum specified 40°C ambient temperature, the 110°C demagnetisation curve is used for the analysis of the outer rotor magnets. Fig. 4.12 shows H at worst case load angle of the CMG, and the white arrows indicated magnetisations direction of the magnets. The white arrow in the segment indicates the "magnetisation direction" induced in the segment by the underlying inner rotor magnet which is not seen in the figures. On the left side the limit on H is 11 kOe, and all areas above this value are white. At H = 11 kOe, the demagntisation of the tangential magnets of the Halbach array is minimal, however, it is seen that a good part of the tangential magnets are white and hence above 11 kOe. To the right the limit is set to 13 kOe, and here only a very small part of the tangential magnets are affected, hence H in the white areas on the left figure are between 11 and 13 kOe. According to the demagnetisation curve at 110 °C the tangential magnets looses ≈0.05 T in remenance at 13 kOe. If the remanance at 20°C (B_{r20}) of the tangential magnets are reduced from 1.25 T to 1.20 T in the 2D FE model, the stall torque is reduced by 2 Nm. As the approach just described is considering an absolute worst case scenario, the influence of demagnetisation of the tangential magnets in the real application will not be of concern. If any risk should be avoided, the grade of the tangential magnets could be upgraded to a N33AH, however, this is a more expensive grade, and B_{r20} is only 1.19 T, hence even weaker than a partly demagnetised magnet in the current N38EH grade.

A similar study is done on the radially magnetised magnets as well as on

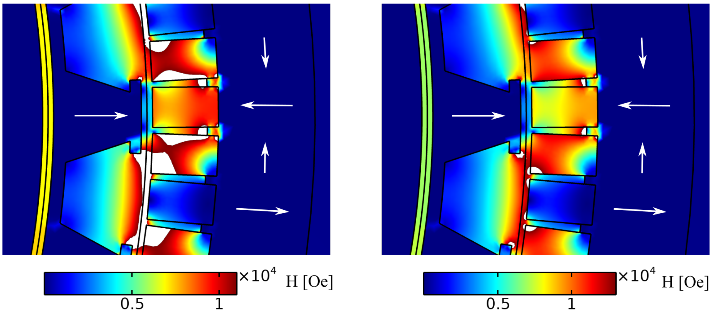

Fig. 4.12: Left: H-field, maximum is 11 kOe. Left: H-field, maximum is 13 kOe.

the inner rotor magnets, and here, there is not seen any risk of demagnetisation.

A flux density plot with flux lines of the final magnetic design is shown in Fig. 4.13. At 20°C the maximum stall torque that is obtained with the given

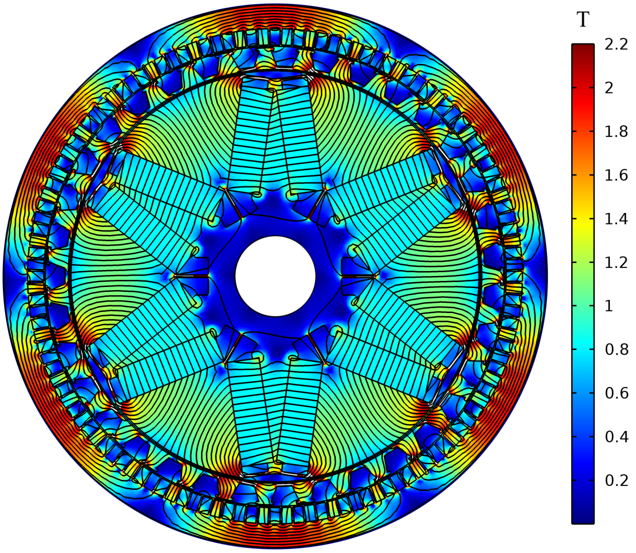

Fig. 4.13: Flux density plot and flux lines for the final design.

design choices is 126.15 Nm with the conservative 100 mm stack length and 131.2 Nm for the full stack version with a stack length of 104 mm. This yields an expected measured stall torque of 97 Nm and 101 Nm respectively at 20°C. The stall torque must further be evaluated at steady state temperature.

The maximum stall torque is only necessary at low speed, hence the temperature at which the stall torque should be evaluated is found from the low speed / high torque steady state thermal tests of MagCon V2. Here, the maximum temperature of the segment ring were 62°C with an ambient temperature of 23°C. The temperature of the outer rotor back iron was not measured at the end of this test, but from the thermal tests at medium and high speed it was seen that the temperature of the outer rotor back iron was 25°C and 35°C lower than the segment ring, respectively. Hence, the magnet temperature at low speed is taken as 60°C, and here, the stall torque of the CMG in 2D FEM is reduced to 116.5 Nm with a 100 mm stack and 121 Nm with a 104 mm stack. This corresponds to an expected measured stall torque of 89.6 Nm and 93 Nm respectively. Naturally, this is lower than the requirement to the peak stall torque set by Flexlink, however, it is agreed that a wider drive unit is not wanted, which would be the case if the stack length of the CMG had to be increased, and also, from a mechanical point of view, a longer CMG stack is not wanted either.

4.1.1 Investigation of alternative CMG design

In Paper B, Fig. 5 show the results of a series of sweeps that evaluates stall torque as a function of pole/segment combinations. Three curves show the stall torque for CMG's with 2, 3 and 4 inner rotor pole pairs as a function of the gear ratio, and the result indicates that a higher torque density can be obtained with 4 inner rotor pole pairs, so this is interesting to pursue.

In the following a CMG with p_i=4, p_o=33 and n_{seg}=37 and a gear ratio of 8.25:1 is studied. It has been designed through a process similar to the one just described where a series of sweeps are used and the final result is seen in Fig. 4.14.

Because the gear ratio has been reduced, the load on the PMSM is increased. To meet the new torque requirement, the stack length of the PMSM designed for MagCon V2 is increased with the ratio of the gear ratios in question:

$$PMSM_{NewStack} = \frac{Gr1}{Gr2} \cdot PMSM_{OldStack} = \frac{10.67}{8.25} \cdot 30 = 39mm \tag{4.2}$$

Hence the PMSM stack length must be increased from 30 mm to 39 mm. The change in rotational losses are estimated based on the existing PMSM where the measured rotational loss curves are used. Due to the smaller gear ratio, the maximum speed of the new PMSM is only 1230 rpm, and here the rotational losses are 28.2 W. Scaling this linearly to the increased stack length, this is increased to 36.5 W of rotational loss at full speed, hence a reduction of 6.1 W compared to the 42.6 W at full speed for the original PMSM. If the copper loss is considered at nominal load however, the copper loss increases from 30.8 W to 36 W, but because the stack length is increased the surface area is also increased which helps remove the heat. As the maximum copper temperature at nominal load for MagCon V2 were 93°C, an increase of approximately 17% in copper loss a housing with larger surface area is not seen as a problem.

Tab. 4.2 lists the deciding parameters for the final design choice.

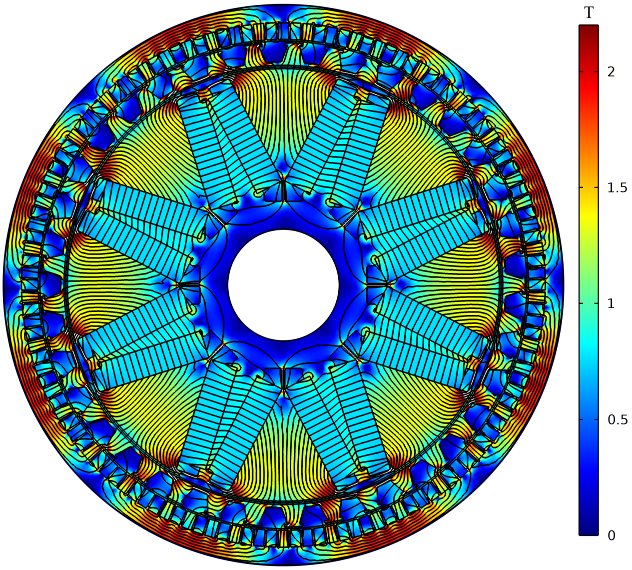

Fig. 4.14: Alternative CMG design with 4 inner rotor pole pairs.

	MagCon V2 1600 rpm	MagCon V3.0 1600 rpm	MagCon V3.1 1230 rpm	MagCon V3.2 1230 rpm
p_i	3	3	4	4
CMG stack	104 mm	104 mm	104 mm	94 mm
PMSM stack	30 mm	30 mm	39 mm	39 mm
Combined stack	134 mm	134 mm	143 mm	133 mm
Airgap	0.4 mm	0.5 mm	0.5 mm	0.5 mm
τ_{stall}, 60°C	88 Nm	93 Nm	100 Nm	90 Nm
Tot. magnet mass	1.91 kg	1.82 kg	2.00 kg	1.82 kg
Loss in CMG				
OR back iron	16.05 W	17.54 W	15.70 W	14.13 W
Segment ring	9.14 W	8.58 W	10.64 W	9.58 W
IR back iron	0.57 W	0.38 W	0.45 W	0.41 W
OR magnets	0.69 W	0.83 W	0.96 W	0.86 W
IR magnets	0.04 W	0.35 W	0.44 W	0.40 W
Total	26.49 W	27.68 W	28.19 W	25.38 W

Table 4.2: Investigation of number of inner rotor poles for MagCon V3.

MagCon V3.0 is the version for which the design phase is thoroughly described in this chapter. *MagCon V3.1* has the new CMG with 4 inner rotor pole pairs and a 104 mm stack length similar to what have been used so far, as well as a longer PMSM. Here it is seen, that it is actually possible to obtain an expected 100 Nm stall torque with 60°C magnet temperature for a CMG with 104 mm stack length, however, the increase in combined stack length of the PMSM and CMG is not desirable, and also, the total amount of magnet material for CMG and PMSM will increase. If it is accepted that the stall torque of the CMG is reduced to 90 Nm, the stack length of the 4 pole-pair CMG can be decreased with 10 mm which is what is done with *MagCon V3.2*. Here it is seen that the combined stack length is now the shortest with 1 mm, and it is also seen, that the rotational losses at maximum speed is the lowest. However, the deciding factor is going to be the loss in the segment ring, as this is so well thermally isolated, and this is where the problems have been seen so far. This is 10.5% smaller in MagCon V3.0 compared to MagCon V3.2. Hence, a compromise is done with respect to total power loss so that the rotational loss in the segment ring can be reduced.

Based on these results, it has been accepted by Flexlink to reduce the requirement to the stall torque, hence *MagCon V3.0* is the chosen drive unit going forward. A final tweek that is done is to reduce the stack length of the segment ring such that it is a little shorter than the stack of the inner and outer rotor. In [59] this was shown to increase the stall torque of the CMG in qustion by 1.8% through a 3D FE model, and on the initial design of the MagCon V1 an analysis were done in 3D FEM where it was found, that by making the stack length 98% of the inner and outer rotor stack length, the stall torque was increased slightly by 1%. With a inner and outer rotor stack length of 104 mm this yields a stack length of 102 mm for the full-stack segment ring and two 49 mm stacks for the split stack version.

The goal of increasing the stall torque of the CMG for MagCon V3 has not been reached although the stall torque have been improved, however, the mechanical strength and stiffness of the segment ring has been increased and the air gaps have been increased with 25% to make the MagCon V3 more robust towards mechanical tolerances.

4.1.2 High speed version

The CMG just described is for the low-speed version of the MagCon drive unit which will have too high rotational losses if used at higher speed. At higher speed, it is not necessary with the high stall torque, hence the induction in the CMG can be reduced to reduce the rotational losses. To minimise the number of unique parts between the low- and high-speed drive unit, it is only the inner rotor that is changed by using magnets of half the width. A flux density plot with flux lines of this design is shown in Fig. 4.15

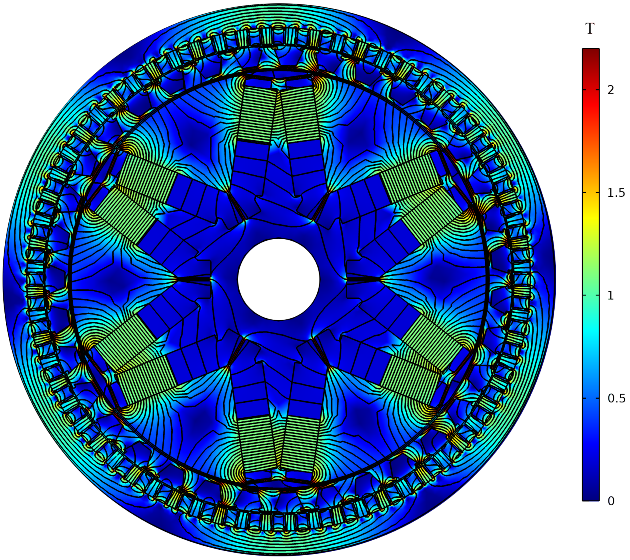

Fig. 4.15: Flux density plot and flux lines for the high speed CMG.

From 2D FEM this design yields a stall torque of 51 Nm with 60°C magnet temperature, hence $51/1.3 = 39.2$ Nm is expected in test, where 1.3 is the simple 3D factor used throughout the design phase. This leaves a good margin to the required 23 Nm between 150 and 300 rpm outer rotor speed. The stall torque does not necessarily need to be 23 Nm exactly, and having more just gives a larger overlap in the operating area between the low- and high-speed version. Like the exact speed that defines the border between the low- and high-speed unit, the stall torque of the high-speed version is an interesting optimisation problem, however, this is not pursued for now but left for future work. From the iron- and magnet-loss model, the losses in the high-speed CMG is estimated and shown in Tab. 4.3 together with the estimated losses for the low-speed version.

	CMG V3.0, low-speed 1600 rpm	CMG V3.0, high-speed 3200 rpm
OR back iron	17.54 W	13.21 W
Segment ring	8.58 W	9.45 W
IR back iron	0.38 W	0.41 W
OR magnets	0.83 W	0.85 W
IR magnets	0.35 W	0.35 W
Total	27.68 W	24.27 W

Table 4.3: Investigation of rotational losses in the high-speed version of the CMG.

The total loss has decreased almost 13%, but the loss in the segment ring has increased 10% which may be a little worrying. However, with the lower induction the fringing fields and leakage fields must be expected to be reduced even further which will decrease the total rotational losses, and hence reduce the temperature of the components surrounding the segment ring.

The strategy where half magnets are used is also applied to the high-speed version of the PMSM. To be able to use the same stator and windings, the flux is approximately halved by halving the width of the PMSM magnets. This approach have been verified with success by the PMSM designer through MotorCAD and experimental results.

4.2 Mechanical integration and assembly

The whole concept of the mechanical integration of MagCon V3 is not changed compared to that of MagCon V2 as this worked quite well, hence this will not be described thoroughly. A few new details and key parts will be mentioned. The integration of the inverter is described later in section 4.4, hence this section only deals with parts belonging to the main drive unit.

Fig. 4.16 show the axial cross section of MagCon V3. The most obvious change is the added feature on the motor housing where the inverter can be connected. Other than that, the distance between the magnetically active parts and the encoder flange as well as the bearings housed here has been increased as much as possible to help decrease the eddy current losses here.

The parts that have changed significantly in MagCon V3 is the outer rotor with the Halbach magnet array and the segment ring with cage and flanges moulded to the laminations stack. Both version of the segment ring are seen in Fig. 4.17. They both feel very rigid and the parts looks really good. However, the mould has to be adjusted slightly to get the tolerances to fit as the two interfaces to the aluminium flanges that keep the segment ring concentric to the inner- and outer rotor had to be machined to obtain a tight fit. These interfaces are indicated on Fig. 4.16 as *Critical tolerance for concentricity*. However, this is the first run on a new mould and in general it is fairly normal that a mould is adjusted to obtain correct tolerances on critical dimensions. In general, at this point, the injection moulding process seem to have great potential which will really help to keep the price down on a CMG.

Fig. 4.18 show the outer and inner rotor stacks with magnets glued onto the outer rotor back iron and into the inner rotor laminations. It is well known that the Halbach array is challenging to glue. If gluing all the radially magnetised magnets first, force must be used to keep the tangentially magnetized magnets between the radially magnetized magnets and onto the back iron until the glue cures. Hence, to show that the introduction of a Halbach array is a feasible solution in a commercial context, it has been an important step to

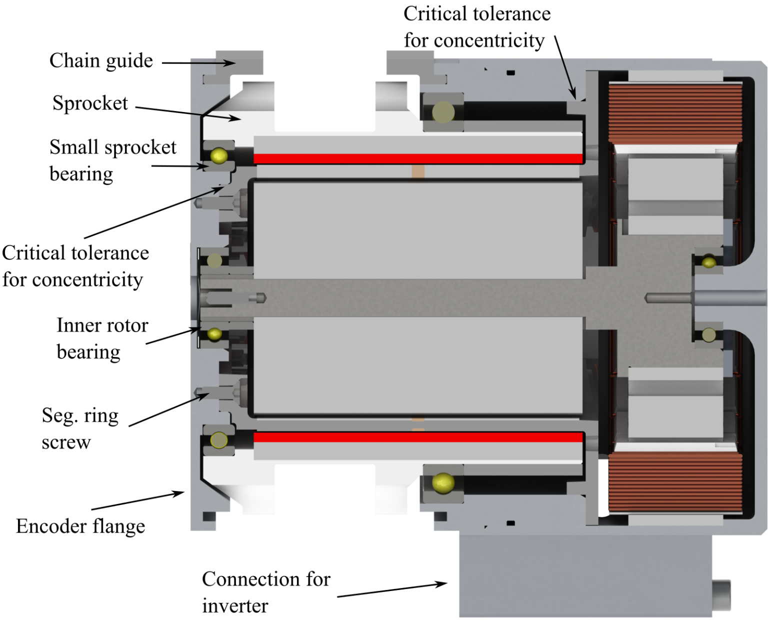

Fig. 4.16: Axial cross section of MagCon V3. Only a few details have been changed in the integration, among other the clareance between inner rotor and encoder flange and bearings in this side.

find a manufacturer that is able to, and wants to, do the assembly of the outer rotor. Such a manufacturer was found, and the magnets in both inner- and outer rotor in Fig. 4.18 has been glued by a Chinese magnet manufacturer. During thermal tests, 2 magnets on the outer rotor came loose, however, after re-gluing these on to the back iron, no problems have been experienced. It is important to notice, that the rotors received from the Chinese manufacturer are proof-of-concept, and in a real production, the magnet array would be vacuum-infused with an epoxy or similar which would secure the magnets very well. This process has been done on the outer rotor magnets for MagCon V1 and V2, and here, no problem with magnets coming loose have been experienced.

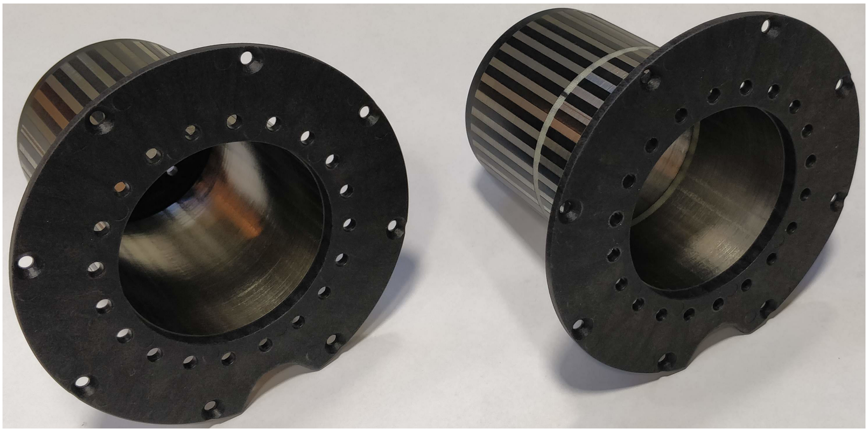

Fig. 4.17: Both versions of the new overmoulded segment ring.

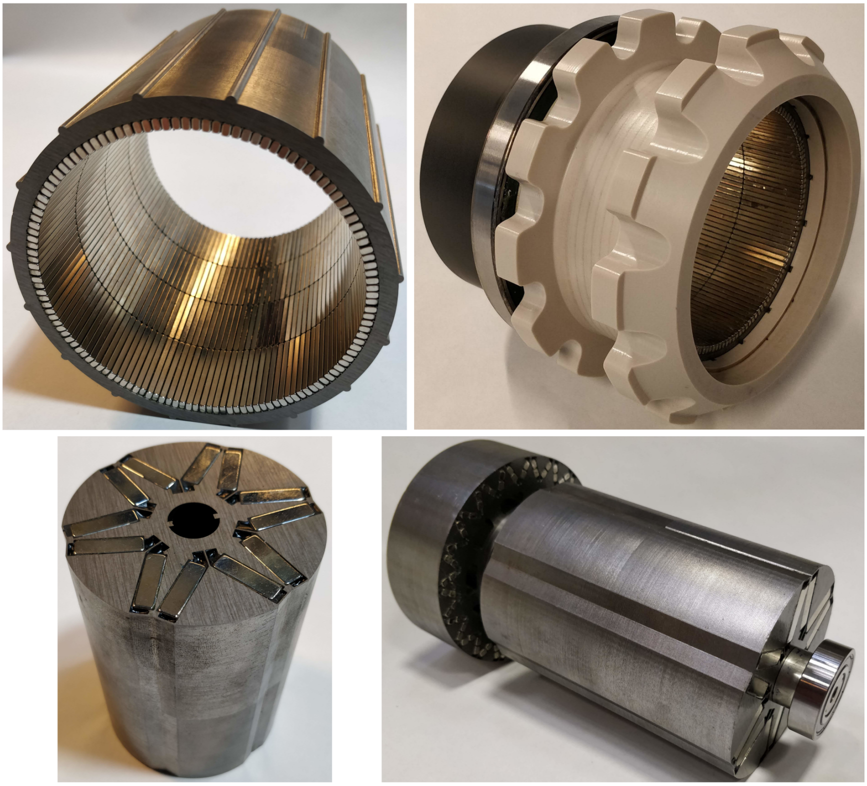

Fig. 4.18: Outer rotor and inner rotor. Both have been assembled by a Chinese magnet manufacturer.

4.3 MagCon V3 test results

This section presents the test results for MagCon V3. Data and results relating to accoustic noise will be treated separately in chapter 5 *Acoustic noise and vibrations*. The following tests are carried out:

- Rotational loss
- Stall torque
- Efficiency
- Running thermal steady state tests

4.3.1 Rotational loss

Two results regarding rotational losses are presented. First, the evaluation of rotational losses in the large bearing and the aluminum dummy flange is repeated to obtain another data point that can confirm the validity of the design rule for B_{pk}. After that the influence of the full-stack and the split-stack segment ring on the rotational loss is evaluated.

Rotational losses are influenced by several parameters such as temperature and total time that a bearing have been running, as bearing losses are often higher for a new bearing compared to a bearing that have been running for a period. Hence, it is important to ensure equal operating conditions in tests where parameters are compared through two or more tests. When doing the tests this is ensured by performing the tests as quickly as possible to reduce the temperature increase in the different components and the tests are done within a relative short time span and without doing any other testing in between which, for instance, could change the friction losses in the bearings.

The result for the large bearing and the aluminum dummy flange is seen in Fig. 4.19. The largest loss is seen in the large bearing, and almost no additional loss is added by the dummy flange. It must be noted though, that the difference seen when the dummy flange is mounted is so small that it might as well be inaccuracies in the measurement. With both bearing and dummy flange, the loss has increased with 2.3 W which is very close to the 2.4 W found from MagCon V2.

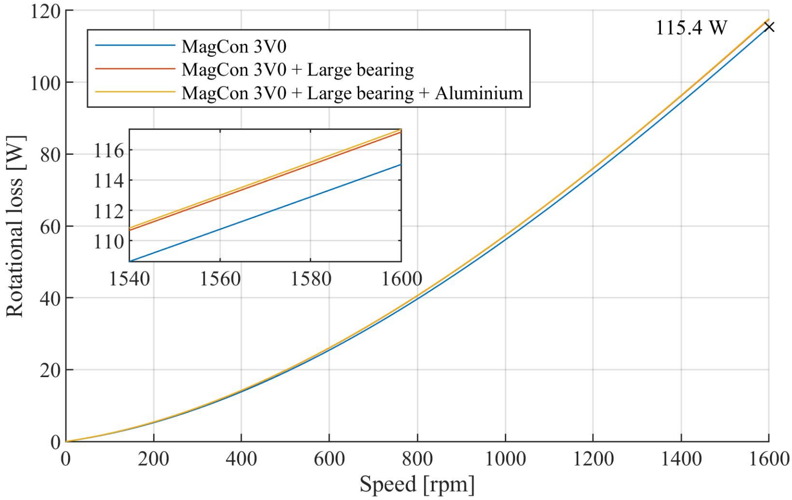

Fig. 4.19: Rotational loss in large bearing and dummy flange.

After the bearing test just described, corrections were made to MagCon V3. It was found, that the large bearing was not seated properly on the sprocket and the PMSM flange was wobbling when the drive unit was running. Also, at this point, the two critical tolerances on the segment rings (indicated on Fig. 4.16) were corrected so that concentricity of the three CMG rotor were ensured. After this, the influence on rotational loss from the split-stack and full-stack segment rings were evaluated, the result is seen in Fig. 4.20.

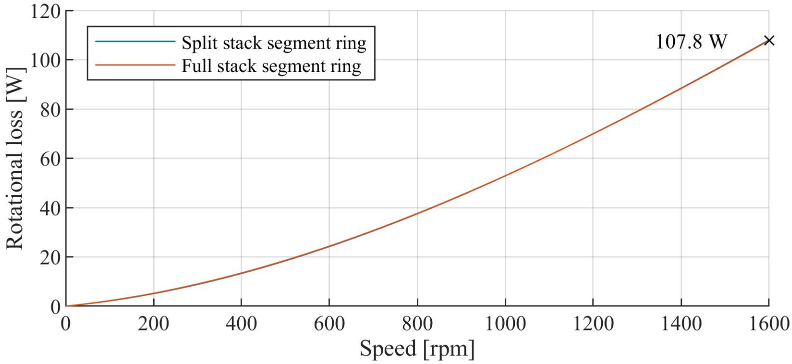

Fig. 4.20: There is no measurable difference between rotational losses with the split-stack segment ring and the full-stack version.

It is evident that the rotational loss has decreased after the corrections made. It furthermore seen, that there is no measurable difference between the two segment rings.

Fig. 4.21 show the rotational losses of MagCon V2 and MagCon V3 and it is seen that the rotational loss of MagCon V3 has been reduced with 23.1 W at the maximum speed of 1600 rpm compared to MagCon V2.

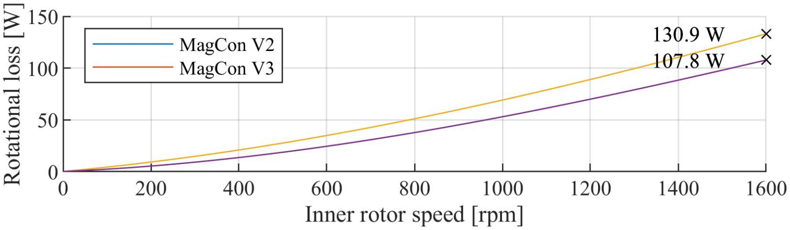

Fig. 4.21: Comparison of rotational losses in MagCon V2 and MagCon V3.

The largest part of the reduction likely comes from the small sprocket bearing. In MagCon V2 the seals in this bearing were standard seals, while in MagCon V3, low friction seals are used. This gives a reduction of up to 14 W for a new bearing according to SKF data. The remaining reduction may come from the slight reduction in CMG iron- and magnet-losses and from the modifications made to the encoder flange, where the distance to the magnetic parts have been increased.

4.3.2 Stall torque

The stall torque obtained with the two segment rings are measured by short circuiting the PMSM used to load the chain conveyor in the test setup and then increase the speed of MagCon V3 until slip occurs while measuring the chain force. Fig. 4.22 shows the force curve with the full-stack segment ring installed, and the force curve with the split-stack segment ring is shown in Fig. 4.23.

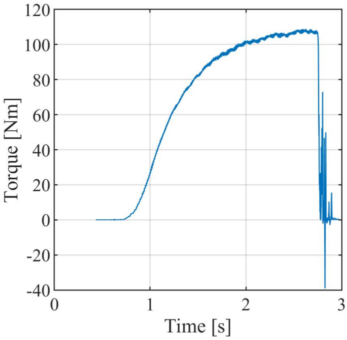

Fig. 4.22: Stall torque measurement for MagCon V3 with the full-stack segment ring.

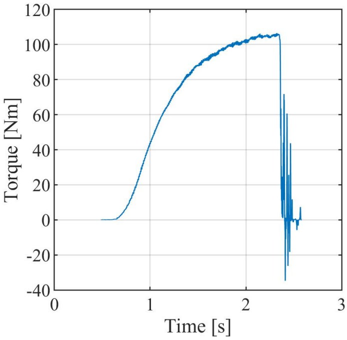

Fig. 4.23: Stall torque measurement for MagCon V3 with the Split-stack segment ring.

The measured stall torque with the full-stack and split-stack segment ring are 109 and 106.5 Nm respectively which yields a torque density of 133 Nm/l and 130 Nm/l for the CMG.

The decrease in stall torque with a magnet temperature of 60°C can be estimated based on the temperature coefficient of B_r of the magnets and the dependency of the stall torque on B^2 in the air gap. The temperature coefficient of B_r of the magnets is -0.1%/°C, hence the flux density in the air gap will decrease approximately -0.1·(60-23) = -3.7 % as the magnet temperature during stall torque tests were 23°C. Hence, the stall torque for the full stack segment ring will decrease to approximately $109 \cdot (1-0.037)^2 = 101$ Nm and hereby actually fulfil the requirement from Flexlink.

4.3.3 Energy efficiency

From the reduced rotational losses of MagCon V3 the energy efficiency is expected to increase as well. In Fig. 4.24 the system efficiency is mapped in the operating area. By comparing it to the efficiency map of MagCon V2 in Fig. 3.6 on page 34 it is seen, that the peak efficiency in the operating area has been increased by 1% to 78.5% at a load point where the output power on the sprocket is 431 W and that the contour curves in general have been moved towards orego which means that a greater energy efficiency is obtained across the whole operating area.

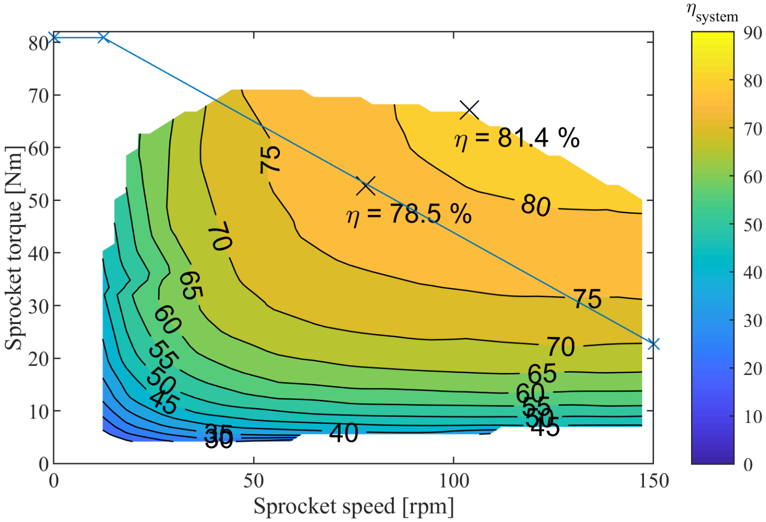

Fig. 4.24: System efficiency with MagCon V3 and Danfoss VLT.

For comparison, the highest required 'minimum efficiency' for a 550 W induction motor with a IE4 efficiency class at 50 Hz is 83.9% for a 4 pole motor, and this is for the motor alone, where the efficiency measured for the MagCon V3 includes inverter, motor and gear.

Again, it must be noticed that the 15 W standby power consumption is included in this efficiency map as it was the case for MagCon V2.

The energy efficiency is one of the parameters that will reduce the lifetime cost of a conveyor system. However, the MagCon V3 uses a total of 1.82 kg of magnet which is expensive compared to steel, aluminum and copper. To get an idea of the time of the return of investment on the MagCon V3 compared to the Movimot, an argument is made, that the magnets are the main difference between the two while the consumption of other materials is equal. It is then investigated how long it will take to pay for the magnets via savings on the electrical bill.

Through several projects where demonstrators of PMSMs and CMGs have been designed and build on the Institute of Energy Technology at Aalborg University, the price paid for the NdFeB magnets have been between 85-110 EUR/kg, depending on grade, size and quantity. A conservative approach is taken, and the highest price is used for all the magnets in MagCon V3, hence the total price for magnets is 200 EUR.

The study is based on the conveyor running for 16 hours per day (two shifts) and 261 days a year which is all days except weekends. Four different load points are studied, where the difference in efficiency for MagCon V3 and Movimot will result in two different power consumptions. The load points are seen in Fig. 4.25, and they are chosen in an area covered by the efficiency map of both drive units.

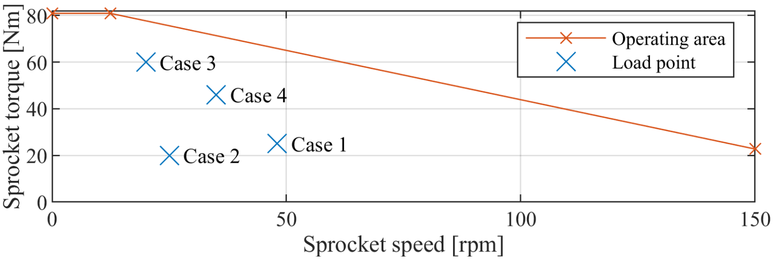

Fig. 4.25: Load points used in the evaluation of energy consumption.

The power consumption is given in kW by Eq. (4.3).

$$P_{electrical} = \frac{\frac{\text{Speed}}{60} \cdot 2\pi \cdot \tau}{1000 \cdot \eta} \tag{4.3}$$

Where *Speed* is sprocket rotational speed [rpm], τ is the sprocket torque [Nm] and η is the system efficiency. The cost of energy (COE) over a given period is then found from Eq. (4.4).

$$\mathrm{COE} = \mathrm{P}_{\mathrm{electrical}} \cdot \text{Energy cost} \cdot \text{Running hours} \tag{4.4}$$

In the last half of 2020 the average energy cost for non-household users in Europe were 0.1254 EUR/kWh including non-refundable taxes. The highest price was found in Germany where they paid 0.1818 EUR/kWh and the lowest were Sweden with 0.0686 EUR/kWh [60].

Tab. 4.4 show the COE [EUR] and the total COE + magnet cost for MagCon V3 as well as the COE of Movimot in the different load points. Each load point is further evaluated for different number of years in operation. The most expensive solution, MagCon V3 or Movimot, is highlighted with orange, and it is seen, that the number of years it takes before the reduced energy cost has paid for the magnets varies with the different load points.

	1 year 4176 h	2 years 8352 h	3 years 12528 h	4 years 16704 h	6 years 25056 h
Case 1					
MagCon V3, power	99	198	297	395	593
MagCon V3, Tot.	299	398	497	595	793
Movimot, power	199	399	598	798	1196
Case 2					
MagCon V3, power	52	104	156	208	312
MagCon V3, Tot.	252	304	356	408	512
Movimot, power	91	183	274	366	548
Case 3					
MagCon V3, power	112	223	335	446	669
MagCon V3, Tot.	312	423	535	646	869
Movimot, power	194	387	581	774	1161
Case 4					
MagCon V3, power	131	261	391	522	783
MagCon V3, Tot.	331	461	591	722	983
Movimot, power	239	477	716	954	1432

Table 4.4: Comparison of cost of energy for MagCon V3 and Movimot, and how many running hours are necessary before the gain in energy efficiency for MagCon V3 has paid for the magnet cost.

Case 2 is the most critical, where it takes almost six years to pay for the magnets, however, in Case 3 the magnets have been paid for after three years, and in case 1 and 4 it only takes two years.

This comparison is based on fairly conservative arguments. The magnet prices have been obtained for very small amounts of magnet for prototype electrical machines, hence in quantity and through negotiation of prices, this cost will be reduced. Fluctuations in magnet price will also have influence on the cost of the drive unit. To somehow set a lower limit for the magnet cost, the cost of neodymium and dysprosium, which have the largest influence on the magnet price, is used. Through the last five years, the price of neodymium have been around 65 EUR/kg [61]. Dysprosium is more expensive with a current price of 408 EUR/kg [62]. If the magnets in MagCon V3 consisted of 30% neodymium and 6.5% dysprosium which is valid for the UH-grade [63], the raw price for the neodymium and dysprosium would be 83 EUR. This gives a good indication that the total price for the magnets can be decreased.

In general, the Movimot uses more material compared to the MagCon V3, so this is also not completely fair for the comparison. It does however show, that it will take a relatively short amount of time before the gain in efficiency has paid for the magnet material.

4.3.4 Thermal steady state tests

MagCon V3 is subjected to thermal steady state tests in the same load points as MagCon V2 to evaluate the effect of the design changes. All tests except one are executed with the full stack segment ring, and the PMSM stator and housing from MagCon V2 is used.

Except for the over-moulded segment ring, only very small details have been changed in the mechanical integration of MagCon V3 compared to MagCon V2, hence the losses are not expected to be dissipated more efficient from V3. However, the drive units are made from machined aluminum. Such a surface has a low emissivity of approximately 0.09 compared to an emissivity of approximately 0.89 for a surface painted with black epoxy [64]. This will reduce the amount of heat that is radiated from the drive unit. To get an idea of the radiated power for the two types of surfaces, the heat removal rate, P_{rad} [W], of the PMSM housing under the conditions for the medium speed test of MagCon V2 is evaluated by (4.5) [65]. The PMSM housing is used for this theoretical experiment as it has a relatively uniform temperature.

$$P_{rad} = A\epsilon\sigma(T_{housing}^4 - T_{amb}^4) \tag{4.5}$$

where A is the exposed surface area of the PMSM housing [m^2], ϵ is the emissivity of a surface [-], σ is the Stefan-Boltzmann constant which is $5.6704 \cdot 10^{-8}$ W/(m^2·K^4), $T_{housing}$ is the surface temperature of the PMSM housing and T_{amb} is the ambient temperature, both in Kelvin.

In the medium speed test of MagCon V2 the PMSM housing temperature reached approximately 80°C, and at this temperature, P_{rad} is 3.5 W for the raw aluminum housing and 34 W for a painted surface. This indicates that a reasonable improvement may be obtained by painting MagCon V3, hence an experimental investigation is conducted.

Five thermal steady state tests are carried out and the load points for each test is given in Fig. 4.26.

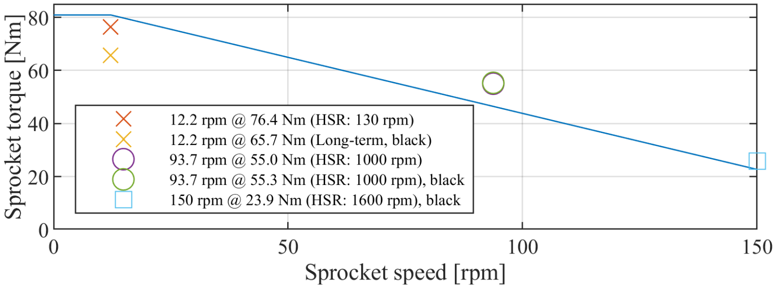

Fig. 4.26: Operating point for thermal steady state tests of MagCon V3.

4.3.5 Thermal tests, raw aluminum

Fig. 4.27 show the result of the first test at 12.2 rpm and 76.4 Nm on the sprocket where no problems were seen.

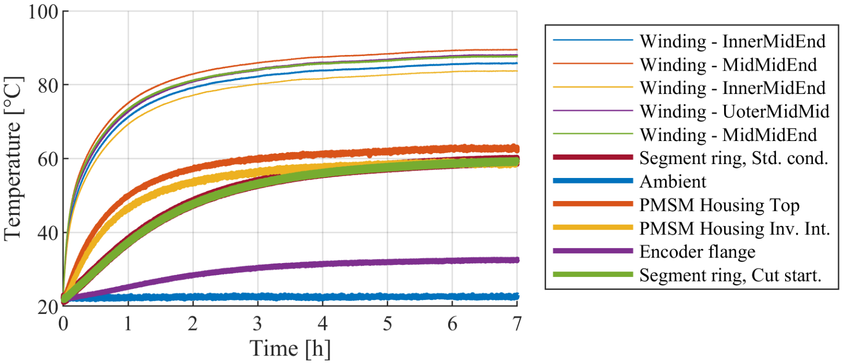

Fig. 4.27: Temperature development during thermal steady state tests of MagCon V3 at 12.2 rpm and 76.4 Nm.

Fig. 4.28 show the result from the test at 93.7 rpm and 55 Nm on the sprocket. This test ran very well until a magnet came loose from the outer rotor after 6 h 45 min. This is seen as a sudden temperature increase on the segment ring caused by the additional friction loss between the magnet and the segment ring. Nothing was damaged, and the magnet was glued back into the outer rotor. However, the temperatures reached steady state and the test results are valid.

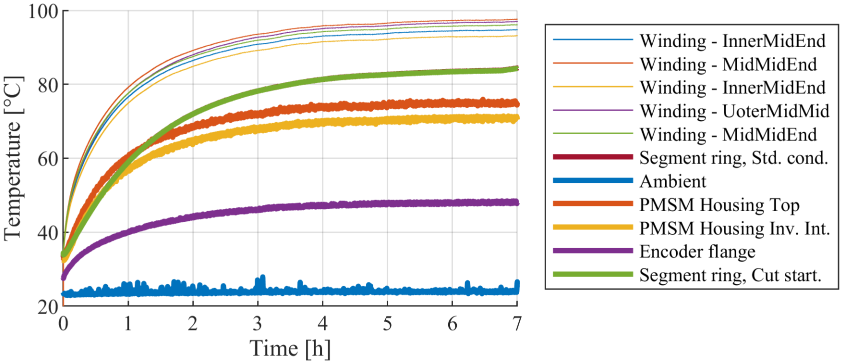

Fig. 4.28: Temperature development during thermal steady state tests of MagCon V3 at 93.7 rpm and 55.0 Nm.

In Tab. 4.5 the steady state temperatures for low- and medium speed for both MagCon V2 and V3 are summarised. At low speed there is not a very big difference in the temperature, although the temperatures in general have decreased a few degrees for MagCon V3. However, at medium speed a more clear tendency is seen where the temperatures in general has dropped 5°C and especially the temperature of the segment ring shows a positive tendency, as this has dropped 9°C in temperature. This suggests that the losses in the segment have indeed been reduced as predicted by the iron loss calculations.

	V3	V2	V3	V2
Sprocket speed	12.2 rpm	12.2 rpm	93.7 rpm	93.7 rpm
Sprocket torque	76.4 rpm	74.4 Nm	55.0 Nm	55.3 Nm
PMSM housing top	63°C	66°C	75°C	80°C
Encoder flange	33°C	35°C	48°C	54°C
Winding (highest)	90°C	93°C	97°C	103°C
Segment ring	60°C	62°C	84°C	93°C
Ambient	23°C	22°C	24°C	23°C

Table 4.5: Comparison of results at low and medium speed between MagCon V2 and V3 with raw aluminum flanges.

Due to the bad experience with MagCon V2 at the high speed load point where the segment ring was deformed, this test has not been done with the non-painted version of MagCon V3 to save the drive unit and secure test data with black paint which is what is described next.

4.3.6 Thermal tests, black paint

In Fig. 4.29 the black version of MagCon V3 is seen. All surfaces have been painted with the exception of the inside end of the PMSM housing because the inner rotor assembly was fixed to this shield by Loctite and to avoid doing too much damage to the bearing and the tolerances where the bearing is seated.

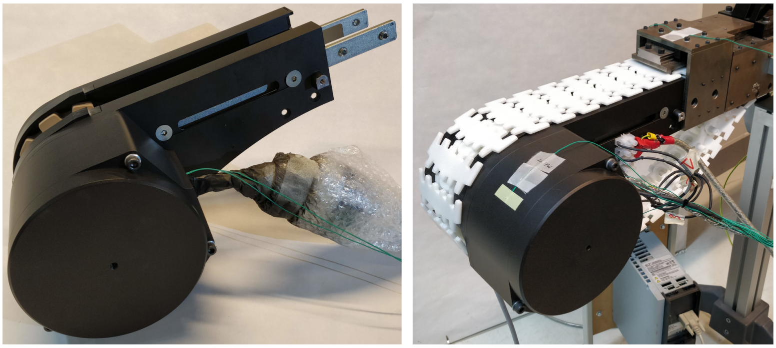

Fig. 4.29: Black, painted version of MagCon V3.

The first thermal test is at medium speed and the result is seen in Fig. 4.30. A test was run just before this one which is why the temperatures are high at the beginning

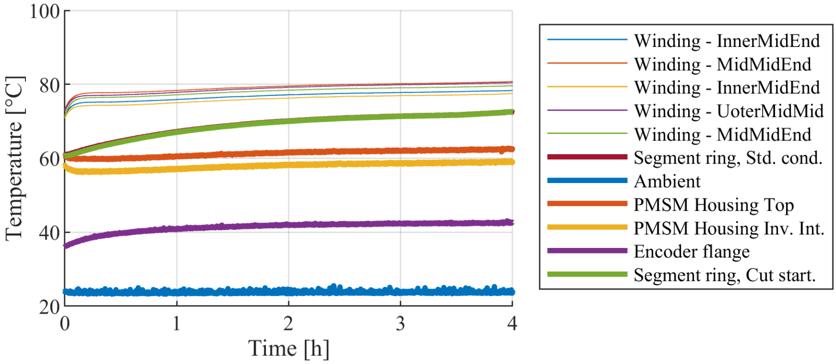

Fig. 4.30: Temperature development during thermal steady state tests of MagCon V3 at 93.7 rpm and 55.3 Nm, painted black.

Again, it is seen that the temperature of the segment ring starts to increase after 3h 30 min. At this point another inner rotor magnet came loose, however, the temperatures had reached steady state and the data were usable. As mentioned earlier, it is not a concern as such that the magnets are coming loose as this is the first outer rotor that has been glued by the Chinese manufacturer, hence they must adopt to the task, and the process of gluing magnets into electrical machines have been done many times before. Hence, it is likely that this issue will be solved.

After re-gluing the magnet, the final test at high speed were initiated. However, as the temperature of the segment ring will reveal, the segment ring failed around 5h 30min where it became oval as it was also seen for MagCon V2.

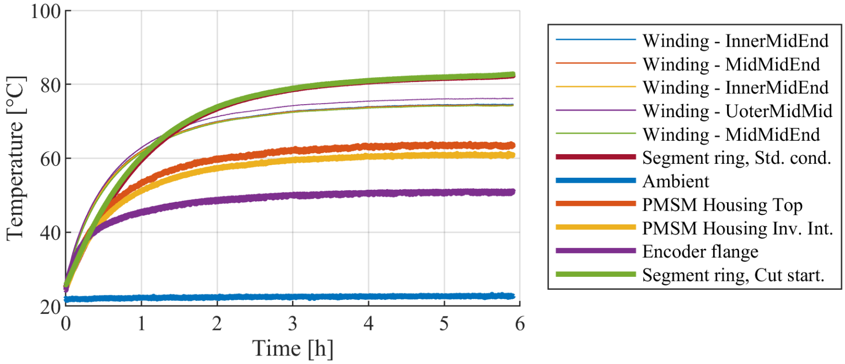

Fig. 4.31: Temperature development during thermal steady state tests of MagCon V3 at 150 rpm and 25.9 Nm painted black.

This is very unfortunate, however, there are some lessons to be learned here. Even though the segment ring has been made much stronger and the losses have been reduced, the segment ring fails, and it fails at a temperature of 82°C compared to the segment ring in MagCon V2 that failed at 110°C. This gives some very strong indications that the problem is related to thermal expansion, and if the data sheets are studied for PEEK and the PA6650GF used for MagCon V2 and V3 respectively, it is seen, that the coefficient of thermal expansion for PEEK is 50 μm/mK while it is 90 μm/mK for the PA6650GF *normal* to the direction of the glass fiber filler but only 15 μm/mK *along* the fiber direction. Due to the way the polymer flows in the mould, the glass fibers in the polymer between the segments are aligned along the length of the stack. Hence, due to the difference in the coefficient of thermal expansion and due to the lower temperature of failure for the new segment ring despite a more rugged design, the failure is strongly suspected to be caused by the difference between thermal expansion of the laminations and the polymer that the cage and segment ring flanges are moulded from. For a future version, a carbon fiber reinforced PPS has been found which has a coefficient of thermal expansion normal to the fiber direction of 18 μm/mK which is much closer to the 12 μm/mK [66] for the lamination material. However, this theory must be validated further through a model where the thermal expansion is studied or by experiments.

Despite the two break-downs, very promising data is obtained through the tests with the black drive unit. Tab. 4.6 shows a comparison of the steady state temperatures at medium and high speed for the aluminium and black version. Since no high speed test was conducted with an raw aluminum version of MagCon V3, the black version is compared to MagCon V2 in this load point.

	V3, black	V3, alu	V3, black	V2, alu
Sprocket rotational speed	93.7 rpm	93.7 rpm	150 rpm	150 rpm
Sprocket torque	55.3 Nm	55.0 Nm	25.9 Nm	26.5 Nm
PMSM housing top	62°C	75°C	63°C	86°C
Encoder flange	42°C	48°C	51°C	64°C
Winding (highest)	80°C	97°C	76°C	103°C
Segment ring	72°C	84°C	82°C	110°C
Ambient	24°C	24°C	23°C	23°C

Table 4.6: Comparison between raw aluminum and black MagCon V3. At full speed, the black MagCon V3 is compared to MagCon V2.

It is seen that the temperatures at medium speed has been decreased by 12-17°C except for the encoder flange which is a little less, but this also had a lower absolute temperature, and hence lower power dissipation via radiation. The comparison between the raw aluminum MagCon V2 and the black MagCon V3 shows a great improvement. Especially the improvement for the segment ring where the temperature have decreased with 28°C indicates that the moulding technique may be feasible with the new carbon fiber reinforced polymer.

The final thermal test is a long-term test. After replacing the broken full-stack segment ring with a split-stack segment ring, MagCon V3 was run for 74 hours at 12.2 rpm and 65.7 Nm on the sprocket without any problems occurring. The resulting temperature during the test is shown in Fig. 4.32.

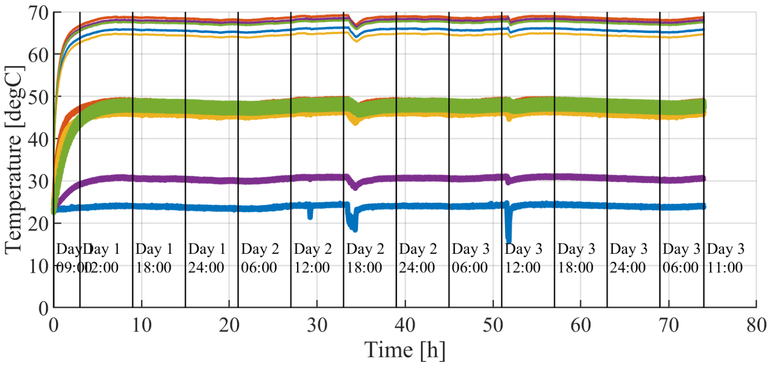

Fig. 4.32: Temperature development during thermal steady state tests of MagCon V3 at 12.2 rpm and 65.7 Nm.

During the test, fluctuations are present in the temperature. Especially two large dips in temperature at Day 2, 18.00 and Day 3, 12.00 where a large door into the laboratory was opened are noticeable. Also, it is seen for all three days, that from 18.00 and until 06:00 the temperature is falling, and then after 06:00 it is increasing again. This is due to the temperature control in the laboratory that decreases the room temperature during the night.

In general, the temperatures from the long-term test are lower than the temperatures seen in Fig. 4.27 where the low speed results with raw aluminum is presented. However, this is not only due to the painted surface, as the load for the long-term test was reduced with 14%, hence the copper loss was reduced as well.

4.4 Inverter

To illustrate the concept of an inverter integrated into the MagCon system with a new idea of a universal input stage and the possibility for customizing the control as well as the amount of data available to the user, an initial demonstrator has been made. The hardware have been roughly designed based on models from component manufacturers and sub-circuits used in earlier work by the author, but adapted to this application and implemented on PCBs designed for this inverter.

The concept of the inverter is based on one of the main goals with the MagCon drive unit: To have as few different variants to do as much as possible. Since the X85H conveyor series is sold to many different markets, the inverter is developed from the ideas of:

- An inverter that operates on 230 VAC - 480 VAC input voltage.
- An inverter that operates on one- or three-phase supply.
- An inverter that can either be used for a stand-alone, fixed speed application or in a more complex environment with a centralised production control structure.

In this first iteration the inverter is designed without an EMI filter. It is well known that the EMI filter will take up additional space, hence, the final inverter will have a larger physical size than what this first iteration will represent.

The inverter is based on an integrated power module with integrated gate drive circuitry which yields a more simple and compact integration on the PCB compared to a solution where discrete components are used. These power modules are made by several manufacturers with 600 V components to service the large sector of white goods applications, air conditioning and so on, hence the price is kept down on these power modules due to the large quantities in which they are sold. The main power circuit is seen in Fig. 4.33.

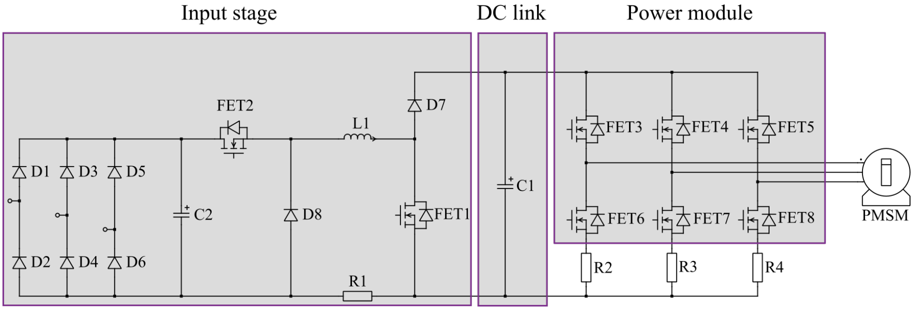

Fig. 4.33: Main power circuit of the MagCon inverter.

The power module is connected to the grid-connected input stage through a 400 V DC-link. To accommodate the requirement of a large span in input voltage to the inverter, the input stage consist of a combination of a buck converter (FET2 and D8) and a boost converter (FET1 and D7) that shares the inductor L1. When the inverter is connected to the, for the inverter, unknown supply, the buck transistor is turned off while the rectified voltage is measured. If the inverter is supplied by a three phase grid, the DC link voltage is maintained by the buck-converter, and if the inverter is supplied by a single phase, the boost converter is used to boost the voltage. When a single phase connection is used, the boost-converter is furthermore used for power factor correction (PFC). This has the dual purpose of reducing the harmonics in the currents that are drawn from the grid and on top of that get the power factor close to unity which will decrease the power loss from reactive currents in the cables that supplies the inverter.

The inverter will primarily utilise sensorless field oriented control (FOC) for the PMSM to reduce the price and the number of components that has to be implemented in the PMSM housing. However, to ensure a reliable start from standstill with load applied to the conveyor, Hall sensors are placed in the stator for position feedback during start-up.

For the first version of the inverter, the control interface is kept simple. The inverter is controlled with a simple RS232 protocol through a galvanically isolated USB interface and a terminal on a PC is used to start and stop the drive unit, change speed and receive basic information such as speed, currents, power etc. This is basically the version of the inverter which can be used for the fixed speed, stand-alone applications where the speed can be set via the USB interface and then an isolated input for a 24 VDC signal can be used to start and stop the drive unit.

The inverter hardware is build into an aluminum enclosure which is mounted to the side of the MagCon V3 next to the PMSM housing. Basically, heat sinks are required for the input stage and for the power module and to distribute heat sources on the enclosure, the bottom is used as heat sink for the power module and the lid is used as a heat sink for the input stage. The IM393-X6E power module from Infineon is used for the inverter stage. To determine the requirements to the heat sink for the power module, a thermal model available from Infineon [67] is used where losses and junction temperatures of IGBTs and diodes in the power module are calculated from switching frequency, rms phase current, rms line-line voltage, DC link voltage, fundamental frequency for the PMSM, ambient temperature and heat sink thermal resistance. With a switching frequency of 16 kHz the total loss in the power module is 24 W, and a heat sink with a thermal resistance to ambient of 3.4°C/W is required to keep the junction temperatures on the limit. By looking at the thermal resistance of the standard heat sink seen in Fig. 4.34 it is found that the bottom of the final aluminum housing for the inverter which measures 166x129 mm can be designed with a thermal resistance of approximately 2°C/W, hence, there is a good margin for the power module. The same heat sink design is used for removing heat from the input stage.

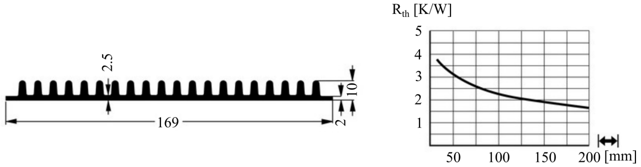

Fig. 4.34: Standard extruded heat sink is used as inspiration for inverter enclosure design [68].

The inverter circuit is divided into a *power PCB* and a *control PCB*. The power PCB contain all power conversion as well as voltage measurement, current measurement and auxiliary power supplies and the control PCB contain the micro processor as well as USB interface, stop/run signal input, a relay and three galvanically isolated I/O channels for the Hall sensors. These channels are isolated because the Hall sensors are placed closely up against the windings, hence if the isolation between stator windings and Hall sensors fail, it should not be able to destroy the inverter.

4.4.1 Inverter demonstrator

In Fig. 4.35 to the left the control PCB is seen and to the right the power PCB is shown. The power module is placed on the bottom of the power PCB so that it can be screwed down to the bottom of the enclosure. The rectifier and buck/boost components are screwed to the aluminum block seen next to the yellow inductor and the large DC link capacitors. This aluminum block is then screwed to the lid to transfer the heat.

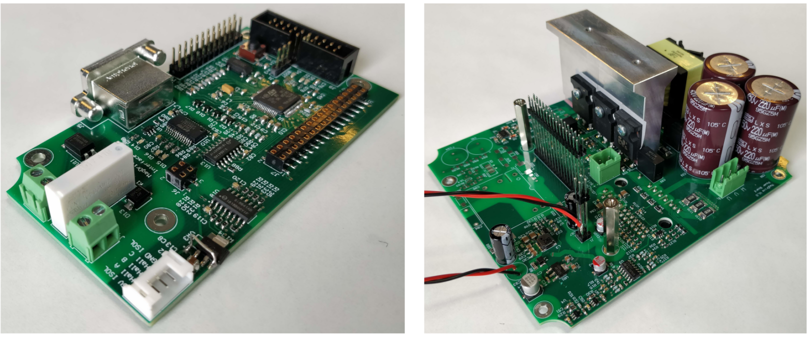

Fig. 4.35: Control PCB (left) and power PCB (right).

To the left in Fig. 4.36 the two PCBs are seen in the enclosures, and to the right the lid is mounted. In the end of the enclosure the USB plug is seen which is used for settings and data extraction.

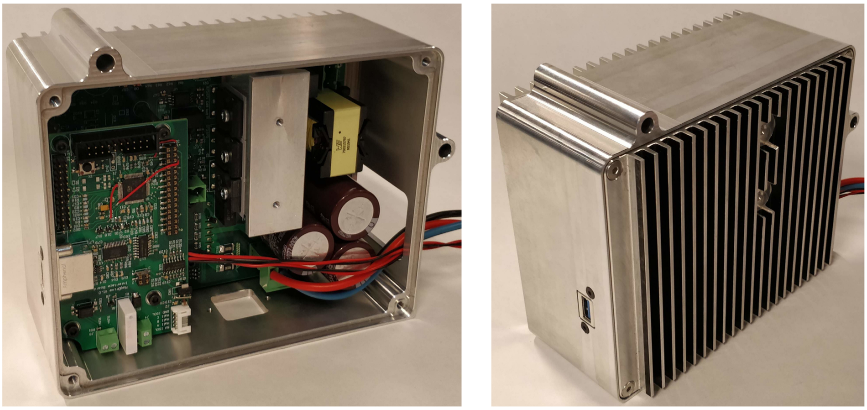

Fig. 4.36: Both PCBs mounted in the inverter enclosure. The control PCB is clicked onto the power PCB..

Fig. 4.37 show how the inverter is attached to the drive unit. Motor phases and Hall sensor signals are connected to the inverter with a plug that is hidden in the small triangular box between the PMSM housing and inverter, which is an integrated part of the PMSM housing. The inverter is placed low on the drive unit as the slot in the PMSM flange is required to be accessible. This slot is used to attach sensors, railing and other equipment to the conveyor in the final application.

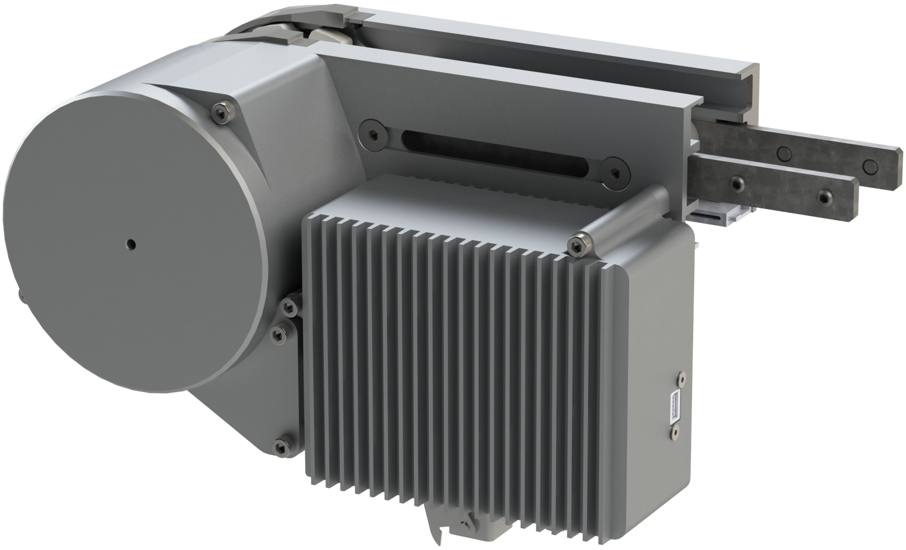

Fig. 4.37: Implementation of inverter on side of drive unit.

4.4.2 Preliminary test results

Only initial tests of the inverter have been conducted at the end of the project, but except the auxiliary power supply, all sub-circuits are up and running. For all test data presented in the following, a filter with a 29 kHz cut-off frequency has been applied to all channels of the oscilloscope as there is no EMI filter to filter out the 120 kHz buck and boost switching frequency from the grid current and -voltage.

Fig. 4.38 show the current drawn from the grid and the DC-link voltage at startup when the inverter is connected to a single phase 230 VAC supply. The buck-converter is used to limit the inrush current by slowly ramping up the duty cycle, starting at 0.2 seconds in the figure. When the duty cycle of the buck-converter has reached 1 at 1.2 seconds, the boost-converter is used to boost the voltage to 400 VDC which is reached at 3.1 seconds after a minor overshoot.

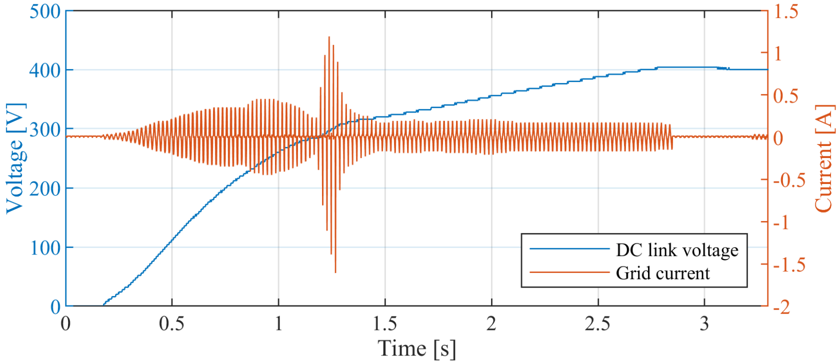

Fig. 4.38: Startup of inverter where the DC link is charged in two stages. First, the buck-converter is used to limit inrush current and secondly the boost-converter is used to reach the targeted DC link voltage of 400 V.

The oscillations in the current follows the pattern that is normally seen for a rectified single phase AC input which can be seen in the first 0.045 seconds Fig. 4.39.

Fig. 4.39 show the change in the grid current waveform when switching from the standard bridge rectified input to the PFC input. At the black **X** the PFC control is enabled where the rectified grid voltage is used as a reference for a current controller which shapes the current to obtain a power factor close to unity. It is clearly seen that the PFC is shaping the current to follow the grid voltage.

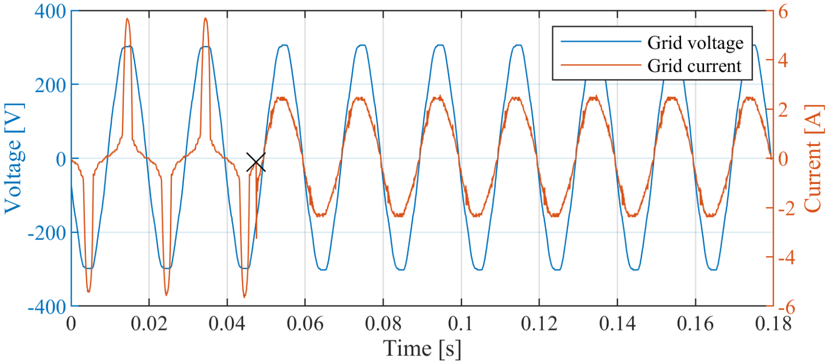

Fig. 4.39: Transition for grid current when the PFC is enabled.

As mentioned earlier, different types of position feedback is used for the FOC. The first method determines the position directly from the combination of the Hall sensor signals. This is shown in Fig. 4.40 where the PMSM in MagCon V3 is running with a fundamental frequency of 20 Hz (120 rpm) without load applied to the drive unit, and the rotor position is shown with the blue line.

Due to the very coarse resolution, the motor current is far from a sinusoid and this also manifests itself as an increase in acoustic noise from the PMSM. In Fig. 4.41 this position is filtered to obtain a more smooth position feedback which improves the waveform of the motor currents.

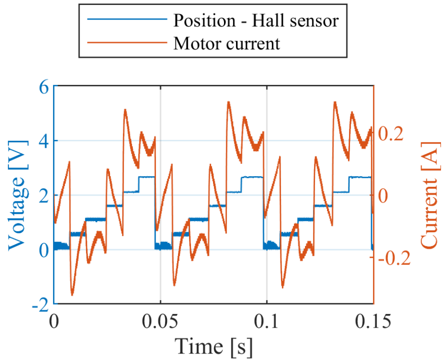

Fig. 4.40: Position signal from Hall sensors and phase current when using the position from the Hall sensors directly as reference for FOC. Fundamental frequency: 20 Hz.

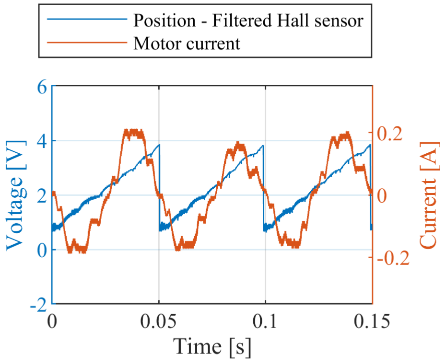

Fig. 4.41: Filtered signal from Hall sensor and improved current waveform. Fundamental frequency: 20 Hz.

Finally, a sensorless position estimation is implemented which is seen in Fig. 4.42. Here the fundamental frequency is 20 Hz as well, and it is seen that the position is more smooth compared to the filtered estimate based on the Hall signals. The MagCon V3 is running at steady state speed with a fundamental frequency of 20 Hz, however, it is seen that the phase current is not consistent from period to period. In Fig. 4.43 the PMSM is running with at fundamental frequency of 80 Hz (480 rpm), and here it is seen that the motor current is more consistent from period to period.

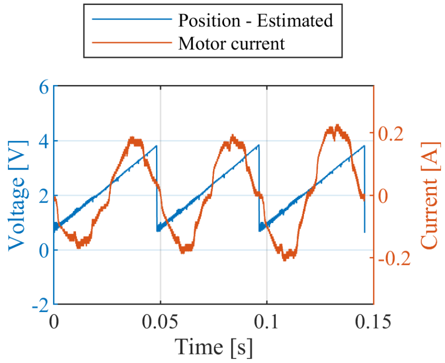

Fig. 4.42: Position estimated by the sensorless FOC algorithm and motor current at 20 Hz fundamental frequency, corresponding to 120 rpm.

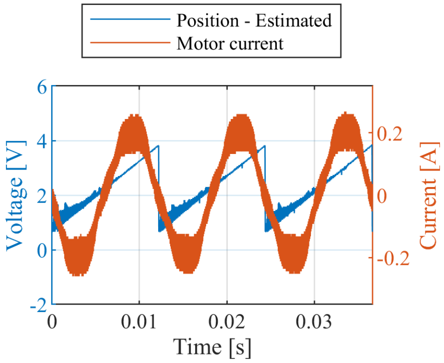

Fig. 4.43: Position estimated by the sensorless FOC algorithm and motor current at 80 Hz fundamental frequency, corresponding to 480 rpm.

In the final implementation of the software, the position which is determined directly from the Hall signals is used from stand-still to 2 Hz fundamental frequency (12 rpm). From 2 Hz to 18 Hz, the filtered version of this position is used, and above 18 Hz fundamental frequency (108 rpm) the sensorless feedback algorithm is used.

It should be clear that more testing is needed at this point as it is interesting to evaluate the system efficiency with the new inverter running MagCon V3 and also, the inverter must be included in the thermal steady state tests. This is left to future work. However, a first version that presents the concept for integrating an inverter on MagCon V3 is presented and the initial tests show that the basic functions are working.

Fig. 4.44 show the overall outer dimensions of MagCon V3 and Movimot (width, length and height).

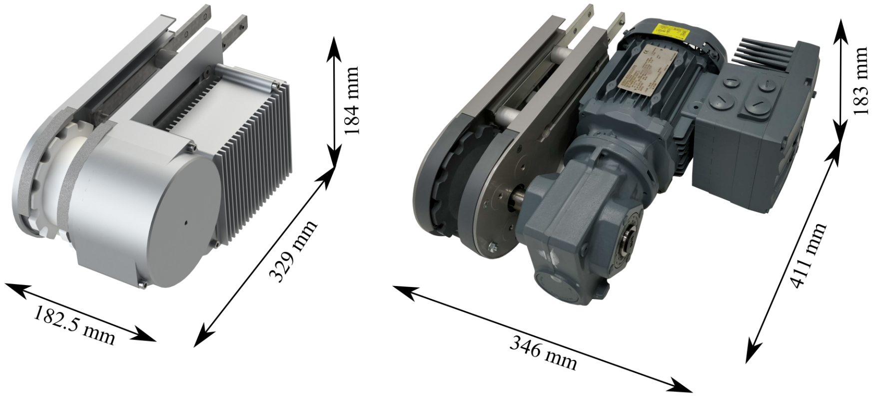

Fig. 4.44: Comparison of size between MagCon V3 and Movimot.

In the final mechanical implementation, MagCon V3 has a mass of 14.4 kg including the inverter. This is a 30% decrease in mass compared to the original Flexlink drive unit with the Movimot gearmotor. Furthermore, the volume placed on the side of the right aluminum flange in Fig. 4.44 has been reduced with 70% from 19.6 L to 5.9 L if the volume is taken as the box that encloses all components on the aluminum flange.

4.5 Summary and conclusions from MagCon V3

The main focus of the updates presented in this chapter have been to continue reducing rotational losses, especially in the segment ring, while increasing the strength and stiffness of the segment ring too, and increasing the air gaps to improve the robustness of the design with respect to mechanical tolerances. Another pole- and segment-combination with 4 inner rotor pole pairs has been explored, but the configuration from MagCon V2 with p_i=3, p_o=32 and n_{seg}=35 is preferred due to minimal rotational losses in the segment ring even though a compromise has been accepted with respect to the stall torque. Through tests it has been shown that MagCon V3 delivers a higher stall torque than expected at 23°C and by estimating the stall torque at steady state temperature of the CMG at the low speed, high torque load point it is seen that the requirement of 100 Nm stall torque is fulfilled. It is further shown that the rotational losses has been decreased as well which entails an increased energy efficiency in the whole operating area. Thermal tests show lower steady state temperatures where the largest improvement is seen in the segment ring. This indicates that the effort and choices made through the design phase has been successful. Furthermore, it has been shown that a significant decrease in temperatures is obtained when increasing the emissivity by simply painting the drive unit.

Thermal test at maximum speed show that the problem with a deforming segment ring continues to exist, however, a strong hypothesis has been presented which suggests, that the problem can be solved by choosing a polymer for the segment ring which has a coefficient of thermal expansion that matches that of the laminations closer. The idea of using injection moulding to add cage and flanges to the segment ring stack has proven successful when considering that the prototypes presented are from a first shot, hence this technique is considered very interesting for future use.

Finally, an initial version of an inverter with a multi-input which enables supplying the inverter from one or three phases over a broad range of voltages has been presented together with some initial test results.

In chapter 3 *MagCon V2* it was briefly mentioned that the acoustic noise coming from MagCon V2 during tests seems to be on a higher level compared to what is experienced with the Movimot mechanically geared motor. The topic of acoustic noise is treated next.

5

Acoustic noise and vibrations

The topic of acoustic noise is a field that to some extend can be hard to put numbers on. Often, some source of acoustic noise can immediately be deemed "loud", "quiet" or "annoying", but to a large extend, acoustic noise is about how humans perceive the sound they hear. Even though the sound pressure level (SPL) is often given as an A-weighted dB value where the purpose of the A-weighting is to match how the different frequencies are amplified or attenuated by the human ear, it is still only *one* number that aims to describe a complex reality. The aim of this chapter is to describe the acoustic noise and vibrations which are experienced from the MagCon drive units in more detail and to analyse the cause of the noise to form some basic theories which can be used to reduce the acoustic noise.

5.1 Paper C, summary

This paper presents a comparison of acoustic noise and vibrations from three different CMGs, each CMG having certain characteristics. The first CMG is the MagCon V1 that had a large cogging torque due to the pole- and segment combination. The second CMG is the MagCon V3 where it is found, that unbalanced radial forces are present on the three rotors due to an odd number of segments in the segment ring. The third CMG is designed for a marine hydrokinetic generator where both cogging torque and unbalanced radial forces have been considered carefully in the design phase.

Both sound pressure from a microphone and accelerations on the CMGs are used for the analysis, and by visually representing the frequency content in the sound pressure and accelerations as a function of speed in waterfall plots, a clear correlation between the two is seen. Several mechanisms of excitation are described, the most important being:

- CMG cogging torque.
- CMG unbalanced radial forces.
- CMG segment passing frequency.

- CMG pole passing frequency.
- PMSM cogging torque.
- PMSM static eccentricity.

It is found, that when a large cogging torque is present, this is one of the, if not *the*, main source of excitation and it dominates the acoustic noise and vibrations. Likewise, when unbalanced radial forces are present, these have a clear impact on the acoustic noise and vibrations. In the third CMG where both cogging torque and unbalanced radial forces are very small, it was not possible to see a clear correlation between the mathematical description of the frequencies of cogging torque and unbalanced radial forces and the experimental data.

It is possible to minimise cogging torque and unbalanced radial forces through the choice of pole- and segment combination. However, in Paper C, it is furthermore shown that certain excitation mechanisms which cannot be mitigated by choice of pole- and segment combination also have an influence. Among these mechanisms are the frequency with which a segment sees a magnetic pole and the frequency with which a magnetic pole sees a segment. Both of these mechanisms were visible in both the acoustic and acceleration data, but with a smaller impact. Hence, it cannot be expected that a completely silent CMG can be designed by eliminating the exciting mechanisms in relation to cogging and unbalanced radial forces, but the results clearly show, that a great improvement can be obtained for the MagCon drive unit with another choice of pole- and segment combination.

5.2 A-weighted sound pressure level

The focus of Paper C is to identify how different excitation mechanisms influence the acoustic noise and vibrations, and the waterfall plots are very good for this purpose. However, the waterfall plot contains a lot of information that can be a challenge to interpret, but by combining the information obtained from a waterfall plot with a simple number like the A-weighted SPL at different speeds, the more simple SPL-plot can to a large extend be used to describe the influence of a limited design change such as segment rings with different stiffness. In the top of Fig. 5.1 the waterfall plot of accelerations on the MagCon V3 with a full-stack segment ring from Paper C is shown, and in the bottom, the SPL from a sound level meter recorded during the same series of tests is represented by the orange curve. The two plots have matching speed on the x-axis. A clear correlation between the vertical bands in the waterfall plot formed by a general increase in amplitude of all FFT bins, and an increased SPL is seen. These peaks represent speeds where a resonance in the system is excited by one of the exciting mechanisms discussed in Paper C.

From 0 to 350 rpm the SPL is at the level of the background noise which is approximately 57 dBA. The first peak around 400 rpm in the SPL plot show that by changing the segment ring, the speed where this resonance is excited is reduced.

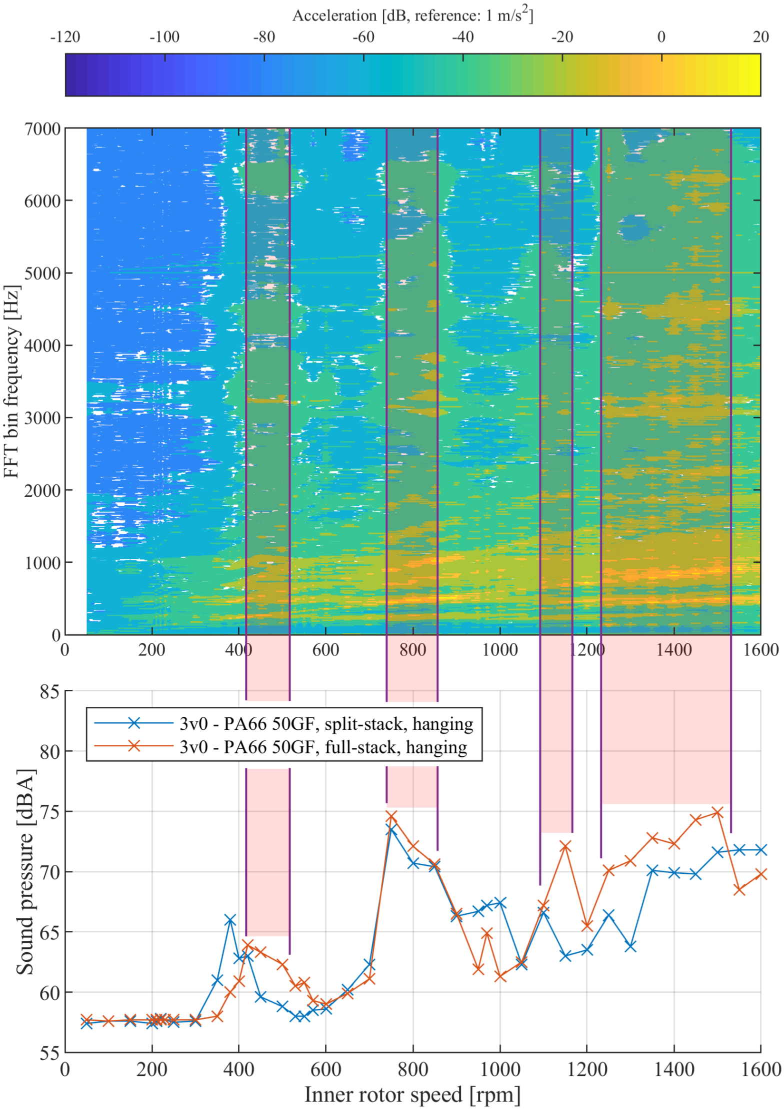

Fig. 5.1: Comparison of 'bands' in waterfall plot of the acceleration where the amplitude in general is increased with the increased SPL from the sound level meter. Waterfall plot based on [69].

This indicates, that this resonance is associated with the segment ring, and it further indicates, that adding the glass fiber ring to the segment ring has actually made it less stiff, as the resonance appears at a lower speed in a system where the segment ring is the only thing that has changed. It is furthermore seen, that the SPL is higher for the less stiff segment ring.

The peak at 800 rpm has not changed significantly, but going further up in speed between 1100 rpm and 1500 rpm it seems that the split-stack segment ring actually reduces the noise slightly, although it is only around 2 dBA in most cases.

To put the SPL in perspective, Danish legislation requires hearing protection if the SPL exceeds 85 dBA, hence the peak SPL for MagCon V3 is 10 dBA lower than this level.

In Fig. 5.2 the SPL measurements of MagCon V2 with the thinner segment ring is added to the plot. A clear and definite conclusion regarding the influence of the stiffness of the segment ring on the SPL cannot be drawn from this figure, however, the tendency at most speeds is that MagCon V2 is louder when evaluated with the A-weighted SPL.

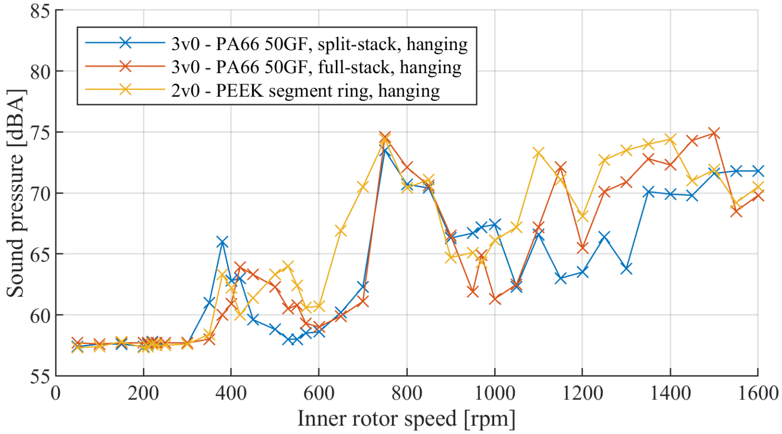

Fig. 5.2: A-weighted sound pressure level for MagCon V2 and MagCon V3 with full- and split-stack segment ring.

In Fig. 5.3 the SPL of the Movimot geared motor is included in the plot for comparison. In this figure the x-axis has been changed to represent the sprocket speed so that the different units can be compared. Like MagCon V2 and V3 the SPL below approximately 28 rpm only slightly exceed the background noise. From this point, the acoustic noise from the Movimot increases and actually exceeds the SPL of the different MagCon units at some points.

There is a difference in how the sound is perceived however. Below 28

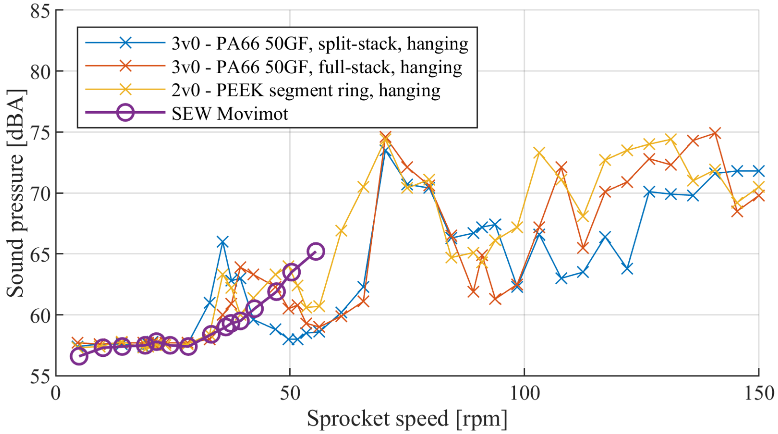

Fig. 5.3: Comparison of Movimot to MagCon V2 and MagCon V3 with full- and split-stack segment ring.

rpm for the Movimot, it is primarily the 8 kHz inverter switching noise that is heard and above 28 rpm, the noise from the cooling fan on the induction machine is the most dominant. The fan noise seems more pleasant compared to the switch noise because it to some degree resembles white noise where the energy in the sound is distributed equally across all frequencies, and to the Author, the fan noise is the preferred noise even though it seems louder when judging from the SPL.

5.2.1 Summary and conclusions regarding acoustic noise

The level of the acoustic noise radiated from a component that is excited by some mechanism does not only depend on the stiffness of the component but also the damping characteristics. This has not been further investigated and is left for future work. However, what is very clear from what is presented in Paper C and from the SPL data in Fig. 5.1 and 5.2 is, that even though it has been possible to increase the stiffness of the segment ring from MagCon V2 to MagCon V3, this does not have a big impact on the measured SPL or the vibrations. What has been shown to be absolutely essential for future versions of the drive unit is to avoid cogging torque and unbalanced radial forces in the CMG as this has been shown to be the source of the majority of the acoustic noise and vibrations. This is done by choosing the pole- and segment combination wisely. To further reduce acoustic noise and vibrations, it would be interesting to try to shape the air gap flux density waveform to reduce the harmonic content, as it is shown in Paper C, that the 2nd and 3rd harmonic of the resulting radial force acting on a segment can be measured in both sound and accelerations.

6

Closing remarks

The work presented in this dissertation is the result of the desire to answer the main research question:

> *Can the advantages of magnetic gearing be utilised to design a compact and energy efficient conveyor drive unit with a wide operating area and how is it integrated with an electric machine and inverter?*

The project has involved extensive experimental work, and because of the complex nature of designing a system such as a complete drive unit for a conveyor application that involves many scientific disciplines, the project has in general followed a process with continued improvement of the relevant theoretical work and models where the special focus points have been determined from the results and learnings from experimental work.

In the following, a conclusion is given on the work presented, and the scientific contributions are outlined. Finally, a number of key topics are recommended for future work.

6.1 Conclusion

MagCon V1 demonstrated that it was feasible to obtain a high measured torque density of 142 Nm/l for the CMG with standard radially magnetised magnets on inner and outer rotor, and through a study on different topologies for CMG/PMSM integration, a very compact drive unit were obtained by integrating the CMG into the sprocket of the drive unit and placing the PMSM on the side of the gear. However, the excessive rotational losses which far exceeded the expectations from simple theoretical calculations on MagCon V1 also made it clear that when packing the CMG and PMSM tightly into an application where the magnetic parts are surrounded by electrically conducting materials, it introduces a limit on the induction level in the CMG to avoid excessive rotational losses and magnetic fields on the conveyor chain, especially when ferromagnetic parts such as the large bearing are placed around the CMG. This limit was substantiated experimentally and used as one of the main constraints in the theoretical models going forward. Detailed experimental work further showed where the rotational losses were induced to help improve the influence of the mechanical integration on the losses by removing material in critical areas. From the results it was clear that moving to an inner rotor PMSM would be an advantage. MagCon V1 had large cogging torque due to the pole- and segment combination of the CMG, and this too was a key learning point.

MagCon V2 presented a substantial re-design of the drive unit. A new pole- and segment combination with three inner rotor pole-pairs reduced the cogging torque and yielded a more torque dense CMG within the given restrictions on induction levels compared to an updated version of the initial design with two inner rotor pole-pairs. Buried magnets were introduced on the inner rotor for improved mechanical rigidity, simpler magnet geometry, fewer unique magnets and to reduce the amount of eddy current losses in inner rotor magnets. The PMSM was redesigned as well, and an inner rotor PMSM made it possible to simplify the mechanical integration and assembly of MagCon V2 significantly compared to MagCon V1. Buried magnets were used on the PMSM rotor as well, and straight stator teeth were introduced to enable the use of pre-wound bobbins to improve manufacturability. The result of the re-design was a reduction of the rotational losses at full speed with a factor of 4.6 and a significantly lower cogging torque compared to MagCon V1 while still maintaining a fairly high measured torque density of 120 Nm/l for the CMG. The rotational loss at the maximum speed for the X85H conveyor system were still 339 W, hence it was decided to split the operating area up and cover it with a low speed and a high speed drive unit, with the low speed unit being the main focus for the remaining work. A strategy for having as many mutual parts between the low- and high-speed drive unit is proposed, where the high speed unit will hold only half the magnet mass on the CMG inner rotor and PMSM rotor, hereby enabling the reuse of PMSM stator and CMG segment ring and outer rotor while still decreasing rotational losses and keeping the back-emf of the PMSM on a level that suits the inverter DC-link voltage.

The efficiency was improved significantly compared to MagCon V1, and thermal steady state tests showed, that MagCon V2 performed well at low to medium speed. At high speed the temperature of the segment ring increased, resulting in a deformed segment ring that came into contact with the outer rotor.

MagCon V3 was developed with focus on the mechanical strength and stiffness as well as the manufacturability of the segment ring. Improved loss models were introduced to evaluate different CMGs for the new drive unit where special focus were on rotational losses in the segment ring. Also, designing the CMG for steady state temperatures was kept in mind due to the reduced remanence of the permanent magnets, which reduces the stall torque of the CMG. To improve on the mechanical aspects, the thickness of the segment ring was increased 33% and both air gaps of the CMG were increased from 0.4 to 0.5 mm. Additionally, the cage and flanges that holds the segment ring laminations were now successfully moulded directly onto the lamination stack in an injection moulding process to reduce the complexity associated with the production of a segment ring. A glass fiber reinforced nylon, PA66-50GF, were used for the cage and flanges.

To increase the stall torque, despite the larger air gaps, without increasing the CMG stack length further, the outer rotor magnets are arranged in a Halbach array with four segments per pole pair. To ensure that the Halbach array is feasible in a commercial context, a Chinese manufacturer who are able to assemble the outer rotor have been found, and two outer rotors were successfully manufactured for the demonstrator. The Halbach array enables a slightly increased measured torque density for the CMG to 133 Nm/l at 23°C, and according to calculations, a stall torque of 101 Nm is possible at steady state temperature for the low speed / high torque operating point, hence the CMG in MagCon V3 meets the requirement.

The rotational loss of MagCon V3 is decreased even further compared to MagCon V2, and this is seen in the efficiency measurement, where the energy efficiency has increased across the entire operating area. MagCon V3 has a maximum energy efficiency from grid to chain of 78.5% at a load point where the output power on the sprocket is 431 W which is quite good. For comparison, a 550 W 4 pole induction machine with an IE4 efficiency class is required to have an efficiency of minimum 83.9%, and this is for the machine only, not including inverter and gear. Through thermal steady state tests it is shown, that temperatures have decreased, especially in the segment ring. It is further shown, that increasing the emissivity of the drive unit by simply painting it results in a considerable decrease in temperature. Hence, at maximum speed, the temperature of the segment ring reaches 82°C compared to 110°C in MagCon V2. However, the segment ring still deforms at the highest speed. It is strongly suspected that the deformation of the segment ring is caused by the difference in the coefficient of thermal expansion between the polymer and the laminations, however, at low to medium speed, MagCon V3 performs well. A carbon fiber reinforced PPS is suggested as a suitable replacement for the PA66-50GF used in MagCon V3.

As the CMG is driven by a PMSM, an inverter is necessary. As this project aims to show a complete system, an inverter is developed to show how this may be integrated with the CMG and PMSM. The inverter features a multi-input stage that enables the inverter to run from single or three phase, 230VAC-480VAC. Initial tests show a functional inverter, however, further tests are needed both for the inverter itself and with the inverter installed into the system.

Through the tests of MagCon V2 and MagCon V3 acoustic noise at a level that seems louder than what is experienced with the benchmark gearmotor is observed. By analysing experimentally obtained acoustic data and acceleration data and comparing it to magnetic excitation frequencies which are described by analytical expressions and through FEA it has been shown, that the unbalanced magnetic forces which are present in these drive units due to the odd number of segments are the main source of the acoustic noise. It has further been shown, that the acoustic noise coming from MagCon V1 can be linked to the cogging torque frequency. Hence, a very tangible proof that both cogging torque and unbalanced magnetic forces must be avoided is given.

To summarise, it has been shown through the work presented in this dissertation, that conveyor applications similar to the X85H series from Flexlink is a feasible application for CMGs. The main challenge at this point is the deformation of the segment ring at high speed, however, a solid idea of how to circumvent this problem is given. Secondly, acoustic noise is an area that can be improved, but here the main source of vibrations and acoustic noise is shown as well, and it is fairly simple to reduce this source significantly. By improving on these main areas, a drive unit which covers a large part of the operating area while reducing the mass with 30% and the volume mounted to the side of the original drive unit with 70%, as well as improving energy efficiency significantly compared to the benchmark gearmotor is obtained. Furthermore, the introduction of the CMG adds an inherent overload protection to the drive unit and removes the mechanical wear and need for lubrication.

6.2 Scientific contributions

Manufacturability and integration

Simple, compact mechanical integration A very simple mechanical implementation has been demonstrated, where most of the end-shields that are traditionally used in CMGs to hold the three concentric rotors are omitted. This enables tighter packaging and simplifies assembly. The lack of these end shields also means that the amount of electrically conducting material that is close to a varying magnetic field is reduced significantly, hence eddy current losses are reduced. Even though close attention is paid to the induction levels in the CMG it has been possible to obtain a high torque density. The fact that the rotational losses has been shown not to bee too far away from what is expected from the loss models further shows that the strategy has been successful.

Manufacturing the segment ring It has been shown, that the cage and flanges can be moulded directly onto the segment ring stack, hereby simplifying the manufacturing process significantly compared to what have been shown earlier. Material choice is crucial for this method.

Halbach array It is shown that the Halbach array is commercially feasible in the context of this conveyor drive unit.

Feasible application for CMGs

A conveyor drive unit has been shown to be a feasible application for the CMG technology as it is a true low speed, high torque application.

Acoustic noise and vibrations in CMGs

Based on correlations between results from FEA, analytical expressions and analysis of experimentally obtained data it has been shown how cogging torque and unbalanced radial forces are directly affecting vibrations and acoustic noise in CMGs.

Balanced design process

A process have been demonstrated where a relatively complicated system is designed by balancing theoretical work, modelling effort and experimental work. The focus of the continued development of theoretical work and modelling effort is guided by experimental results and vice versa. This has ensured continuous progress in the project.

Multi-input inverter

An input stage that is compatible with one- and three-phase AC supply within a voltage range of 230-480 VAC has been proposed.

6.3 Future work

There are a number of interesting points and topics that should be treated in future work. The author especially recommends the following tasks:

Segment ring, thermal properties It must be shown that a stable segment ring at high speed is obtained by using a polymer in the moulding process with a coefficient of thermal expansion closer to that of the laminations. It could be the carbon fiber reinforced PPS which have been suggested. It should be proved experimentally, however, a multi-physics model could be build where thermal expansion is studied to learn more about it.

Segment ring, structural A model that enables structural analysis of a laminated structure would be very helpful in the design of the segment ring. If fatigue is to be studied from a theoretical point of view in the same way that it is done for mechanical gear where the teeth are subject to cyclic loads as well, the stress in the laminations can be obtained from such a model.

Unbalanced radial forces A new pole- and segment combination should be found to avoid both cogging torque and unbalanced magnetic forces in the CMG to decrease acoustic noise and vibrations.

Segment ring, damping characteristics It would be interesting to study the damping in the mechanical structure of the segment ring and how it is influenced by the glass fiber ring. In the acoustic noise measurements, it was seen that the SPL was higher for the segment ring with the glass fiber ring at some speeds compared to the full-stack version, while it was lower at other speeds.

Air gap flux density waveform As it has been shown that the 2^{nd} and 3^{rd} harmonic in the resulting radial force on the segments are visible in the acoustic signature of the CMG, it would be interesting to look at shaping the air gap flux density so that a smooth sinusoidal resulting radial force is obtained.

3D FEM Throughout this PhD project, 2D FEM has been used together with an empirical correction factor for 3D effects to predict the stall torque of the CMG. This is quick to work with, however, besides a more precise estimation of the stall torque, a 3D FE model could provide information on the flux density in surrounding components to gain more knowledge about how to reduce the losses even further here.

Revised outer rotor magnet guides In MagCon V3 small separation tabs have been used to position the magnets and improve the glue joint, however, this has increases the distance between the magnets which have a significant influence on the stall torque. An improved design with a series of pockets in the outer rotor back iron for every second magnet so that it is only the dimensional tolerance on the magnets that determines the distance between them should be investigated.

Optimization algorithm for magnetic design The magnetic design of the CMG is dictated by a series of good constraints, such as the limit on flux density in the large bearing, air gap lengths and segment height. After making three versions of the drive unit a lot of experience is obtained with the design and the factors that has influence, hence it should be investigated how to set up an optimisation algorithm for the magnetic design to get a more systematic approach to the design process. Interesting parameters to investigate in such an algorithm is thickness of outer rotor back iron, outer rotor magnet thickness, inner rotor magnet thickness, inner rotor magnet angle and inner rotor diameter.

Further test of inverter The inverter should go through further stand-alone tests and efficiency tests. Thermal steady state tests are relevant to repeat to see how the additional heat source will affect the total system.

Thermal mapping A thorough mapping of magnet temperatures in relevant load points would enable more accurate modelling of CMG stall torque at elevated temperatures and help to establish a more accurate specification of the magnet grade. This could lead to cheaper and stronger magnets.

Sprocket During the PhD project the sprocket have been milled from POM (MagCon V1) and PEEK (MagCon V2 + V3). Like the segment ring, it should be investigated how to use the over-mould technique to manufacture the sprocket. Also, thermal expansion for the interface to the small sprocket bearing should be studied to mitigate a loose fit while running.

Test of high-speed version Only the high-speed version of the PMSM has been tested. The complete high-speed version of the conveyor drive unit needs to be tested as well.

Speed that defines switch between low- and high-speed drive unit The switch between the low- and high-speed drive unit has been defined as 1600 rpm, however, to find the optimal speed where the transition should occur and what the stall torque of the high-speed version should be depending on efficiency, customer needs, material usage and so on would be an interesting study.

Parking brake Because the CMG is not self locking like the worm gear, a parking brake is needed in applications with inclined conveyor belts. A relay has been included in the inverter to activate such a park brake, however, the design of the parking brake itself has been out of scope for the work done in this PhD.

References

[1] Ford Motor Company, Company timeline, `https://corporate.ford.com/history.html`, accessed May 2021.

[2] T. Miller, Brushless Permanent-magnet and Reluctance Motor Drives, Monographs in electrical and electronic engineering, Oxford University Press, 1989.

[3] Flexlink, `https://www.flexlink.com/en/home/`, accessed May 2021.

[4] Hytrol, `https://hytrol.com/`, accessed May 2021.

[5] Bosch Rexroth, `https://www.boschrexroth.com`, accessed May 2021.

[6] G. Zhou, X. Xu, Y. Xiong, L. Zhang, Design and analysis of low-speed high torque direct-driven permanent magnet synchronous machines(pmsm) with fractional-slot concentrated winding used in coal mine belt conveyor system, in: 2017 20th International Conference on Electrical Machines and Systems (ICEMS), 2017, pp. 1–5. `doi:10.1109/ICEMS.2017.8056054`.

[7] Dorner, `https://www.dornerconveyors.com/europe/products/2x-series/2200-belted-conveyor/universal-drive`, accessed May 2021.

[8] M. R. Harris, G. H. Pajooman, S. M. A. Sharkh, The problem of power factor in vrpm (transverse-flux) machines, in: 1997 Eighth International Conference on Electrical Machines and Drives (Conf. Publ. No. 444), 1997, pp. 386–390. `doi:10.1049/cp:19971104`.

[9] E. Drexler, Conveyor roller, uS Patent 1889173A (Nov. 1932).
URL `https://patents.google.com/patent/US1889173A/en?oq=1889173`

[10] Interroll, `https://www.interroll.us/products/drives-and-controls/belt-drives/`, accessed May 2021.

[11] Interroll, `https://www.interroll.com/drum-motor-service/`, accessed May 2021.

[12] M. Popescu, D. A. Staton, S. Jennings, J. Schnuttgen, T. Barucki, A line-fed permanent-magnet motor solution for drum-motor and conveyor-roller applications, IEEE Transactions on Industry Applications 49 (2) (2013) 832–840. `doi:10.1109/TIA.2013.2241712`.

[13] M. Popescu, D. Staton, A. Boglietti, A. Cavagnino, S. Jennings, T. Barucki, Experimental validation of a simple multiphysics model for drum roller driven by induction motor, in: IECON 2011 - 37th Annual Conference of the IEEE Industrial Electronics Society, 2011, pp. 1848–1853. `doi:10.1109/IECON.2011.6119587`.

[14] Magnetic Innovations, `https://www.magneticinnovations.com/`, accessed May 2021.

[15] M. Turci, E. Ferramola, F. Bisanti, G. Giacomozzi, Worm gear efficiency estimation and optimization, The Journal of Gear Manufacturing (2016) 46–53.

[16] A. Skulić, D. Krsmanovic, S. Radosavljevic, L. Ivanovic, B. Stojanovic, Power losses of worm gear pairs, ACTA TECHNICA CORVINIENSIS - Bulletin of Engineering X (2017) 39–45.

[17] Kyung-Ho Ha, Young-Jin Oh, Jung-Pyo Hong, Design and characteristic analysis of non-contact magnet gear for conveyor by using permanent magnet, in: Conference Record of the 2002 IEEE Industry Applications Conference. 37th IAS Annual Meeting (Cat. No.02CH37344), Vol. 3, 2002, pp. 1922–1927 vol.3. `doi:10.1109/IAS.2002.1043796`.

[18] Misumi, Misumi introduces magnetic transmission drive components, `https://us.misumi-ec.com/news/topics/2009/01/misumi-introduces-magnetic-transmission-drive-components.html`, accessed May 2021.

[19] Nanotech, Magnet gear, `http://www.nanoloy.co.kr/en/sub.php?code=105`, accessed June 2021.

[20] K. Atallah, D. Howe, A novel high-performance magnetic gear, IEEE Transactions on Magnetics 37 (4 I) (2001) 2844–2846. `arXiv:arXiv:1011.1669v3`, `doi:10.1109/20.951324`.

[21] P. O. Rasmussen, T. O. Andersen, F. T. Joergensen, O. Nielsen, Development of a high performance magnetic gear, in: 38th IAS Annual Meeting on Conference Record of the Industry Applications Conference, 2003., Vol. 3, 2003, pp. 1696–1702 vol.3. `doi:10.1109/IAS.2003.1257784`.

[22] C. Armstrong, Power-transmitting device., uS Patent 687,292 (Nov. 26 1901).
URL `http://www.google.co.uk/patents/US687292`

[23] F. T. Jorgensen, T. O. Andersen, P. O. Rasmussen, Two dimensional model of a permanent magnet spur gear, in: Fourtieth IAS Annual Meeting. Conference Record of the 2005 Industry Applications Conference, 2005., Vol. 1, 2005, pp. 261–265 Vol. 1. `doi:10.1109/IAS.2005.1518319`.

[24] S. S. Nielsen, R. K. Holm, P. O. Rasmussen, Conveyor system with a highly integrated permanent magnet gear and motor, IEEE Transactions on Industry Applications 56 (3) (2020) 2550–2559. `doi:10.1109/TIA.2020.2977877`.

[25] P. M. Tlali, R. Wang, S. Gerber, Magnetic gear technologies: A review, in: 2014 International Conference on Electrical Machines (ICEM), 2014, pp. 544–550. `doi:10.1109/ICELMACH.2014.6960233`.

[26] M. B, Magnetic transmission, uS Patent 3,378,710 (Apr. 16 1968).
URL `https://www.google.com/patents/US3378710`

[27] B. Praslicka, M. C. Gardner, M. Johnson, H. A. Toliyat, Review and analysis of coaxial magnetic gear pole pair count selection effects, IEEE Journal of Emerging and Selected Topics in Power Electronics (2021) 1–1`doi:10.1109/JESTPE.2021.3053544`.

[28] T. Frandsen, Motor integrated permanent magnet gear, Ph.D. thesis, The Doctoral School of Engineering and Science, associate Prof. Peter Omand Rasmussen, Aalborg University (2016). `doi:10.5278/vbn.phd.engsci.00107`.

[29] F. William, Electric magnetic gear, uS Patent US1913371A (Jun. 1933).
URL `https://patents.google.com/patent/US1913371A/en`

[30] M. Venturini, F. Leonardi, High torque, low speed joint actuator based on pm brushless motor and magnetic gearing, in: Conference Record of the 1993 IEEE Industry Applications Conference Twenty-Eighth IAS Annual Meeting, 1993, pp. 37–42 vol.1. `doi:10.1109/IAS.1993.298900`.

[31] K. T. Chau, D. Zhang, J. Z. Jiang, C. Liu, Y. Zhang, Design of a magnetic-geared outer-rotor permanent-magnet brushless motor for electric vehicles, IEEE Transactions on Magnetics 43 (6) (2007) 2504–2506. `doi:10.1109/TMAG.2007.893714`.
URL `http://ieeexplore.ieee.org/stamp/stamp.jsp?tp={&}arnumber=4202811`

[32] L. N. Jian, K. T. Chau, D. Zhang, J. Z. Jiang, Z. Wang, A magnetic-geared outer-rotor permanent-magnet brushless machine for wind power generation, in: 2007 IEEE Industry Applications Annual Meeting, 2007, pp. 573–580. `doi:10.1109/07IAS.2007.42`.

[33] R. Royce, Compact electrical machine, uS Patent US6794781B2 (Sep. 2004).
URL https://patents.google.com/patent/US6794781B2/en?oq=6794781

[34] L. Jian, K. T. Chau, J. Z. Jiang, A magnetic-geared outer-rotor permanent-magnet brushless machine for wind power generation, IEEE Transactions on Industry Applications 45 (3) (2009) 954–962. doi:10.1109/TIA.2009.2018974.

[35] A. B. Kjaer, S. Korsgaard, S. S. Nielsen, L. Demsa, P. O. Rasmussen, Design, fabrication, test, and benchmark of a magnetically geared permanent magnet generator for wind power generation, IEEE Transactions on Energy Conversion 35 (1) (2020) 24–32. doi:10.1109/TEC.2019.2951998.

[36] S. Korsgaard, A. B. Kjaer, S. Staal Nielsen, L. Demsa, P. O. Rasmussen, Acoustic noise analysis of a magnetically geared permanent magnet generator, in: 2019 IEEE Energy Conversion Congress and Exposition (ECCE), 2019, pp. 717–723. doi:10.1109/ECCE.2019.8912892.

[37] A. Penzkofer, K. Atallah, Analytical modeling and optimization of pseudo-direct drive permanent magnet machines for large wind turbines, IEEE Transactions on Magnetics 51 (12) (2015) 1–14. doi:10.1109/TMAG.2015.2461175.

[38] Magnetomatics, Wind turbine generator, https://www.magnomatics.com/post/wind-turbine-generator, accessed June 2021.

[39] P. O. Rasmussen, H. H. Mortensen, T. N. Matzen, T. M. Jahns, H. A. Toliyat, Motor integrated permanent magnet gear with a wide torque-speed range, 2009 IEEE Energy Conversion Congress and Exposition, ECCE 2009 (2009) 1510–1518doi:10.1109/ECCE.2009.5316280.
URL http://ieeexplore.ieee.org/stamp/stamp.jsp?tp={&}arnumber=5316280

[40] P. O. Rasmussen, T. V. Frandsen, K. K. Jensen, K. Jessen, Experimental evaluation of a motor-integrated permanent-magnet gear, IEEE Transactions on Industry Applications 49 (2) (2013) 850–859. doi:10.1109/TIA.2013.2242423.

[41] T. V. Frandsen, P. O. Rasmussen, K. K. Jensen, Improved motor intergrated permanent magnet gear for traction applications, in: 2012 IEEE Energy Conversion Congress and Exposition (ECCE), 2012, pp. 3332–3339. doi:10.1109/ECCE.2012.6342334.

[42] T. V. Frandsen, L. Mathe, N. I. Berg, R. K. Holm, T. N. Matzen, P. O. Rasmussen, K. K. Jensen, Motor integrated permanent magnet gear in a battery electrical vehicle, IEEE Transactions on Industry Applications 51 (2) (2015) 1516–1525. `doi:10.1109/TIA.2014.2360016`.

[43] V. Asnani, J. Scheidler, T. Tallerico, Magnetic gearing research at nasa, in: AHS International 74th Annual Forum & Technology Display, 2018.

[44] Z. A. Cameron, T. T. Tallerico, D. J. Scheidler, Lessons learned in fabrication of a high-specific-torque concentric magnetic gear, in: Vertical Flight Society 75th Annual Forum & Technology Dispaly, 2019.

[45] Z. Cameron, D. J. Scheidler, T. Tallerico, Lessons learned in fabrication of a high-specific-torque concentric magnetic gear, `https://ntrs.nasa.gov/citations/20190026449`, slides from 'VFS 75th Annual Forum and Technology Display', May 16, 2019, accessed May 2021.

[46] B. McGilton, M. Mueller, A. McDonald, Review of magnetic gear technologies and their applications in marine energy, in: 5th IET International Conference on Renewable Power Generation (RPG) 2016, 2016, pp. 1–6. `doi:10.1049/cp.2016.0535`.

[47] M. Johnson, M. C. Gardner, H. A. Toliyat, S. Englebretson, W. Ouyang, C. Tschida, Design, construction, and analysis of a large-scale inner stator radial flux magnetically geared generator for wave energy conversion, IEEE Transactions on Industry Applications 54 (4) (2018) 3305–3314. `doi:10.1109/TIA.2018.2828383`.

[48] H. Baninajar, J. Z. Bird, S. Modaresahmadi, W. Williams, Electromagnetic and mechanical design of a hermetically sealed magnetic gear for a marine hydrokinetic generator, in: 2018 IEEE Energy Conversion Congress and Exposition (ECCE), 2018, pp. 4987–4993. `doi:10.1109/ECCE.2018.8557386`.

[49] H. Baninajar, J. Z. Bird, S. Modaresahmadi, W. Williams, Electromagnetic design and assembly analysis of a halbach rotor magnetic gear for a marine hydrokinetic application, in: 2019 IEEE Energy Conversion Congress and Exposition (ECCE), 2019, pp. 732–739. `doi:10.1109/ECCE.2019.8911901`.

[50] F. Jørgensen, Design and construction of permanent magnetic gears, Ph.D. thesis (2010).

[51] S. S. Nielsen, R. Koldborg Holm, N. I. Berg, P. Omand Rasmussen, Magnetically geared conveyor drive unit - an updated version, in: 2020 IEEE Energy Conversion Congress and Exposition (ECCE), 2020, pp. 285–292. `doi:10.1109/ECCE44975.2020.9235375`.

[52] F. Deng, An improved iron loss estimation for permanent magnet brushless machines, IEEE Transactions on Energy Conversion 14 (4) (1999) 1391–1395. `doi:10.1109/60.815078`.

[53] Y. Liu, S. K. Kashif, A. M. Sohail, Engineering considerations on additional iron losses due to rotational fields and sheet cutting, in: 2008 18th International Conference on Electrical Machines, 2008, pp. 1–4. `doi:10.1109/ICELMACH.2008.4800071`.

[54] A. Kraemer, M. Veigel, P. Pontner, M. Doppelbauer, G. Lanza, Influences of separation and joining processes on single tooth laminated stacks, in: 2016 6th International Electric Drives Production Conference (EDPC), 2016, pp. 178–185. `doi:10.1109/EDPC.2016.7851331`.

[55] L. W. Matsch, J. D. Morgan, Electromagnetic and Electromechanical Machines, John Wiley and Sons, 1987.

[56] E. Plastics, Tecapeek natural, `https://www.ensingerplastics.com/en/shapes/products/peek-tecapeek-natural`, accessed June 2021.

[57] EMS-GRIVORY, Grivory gvn-5h black 9915, `https://ems.materialdatacenter.com/eg/material/pdf/datasheet/?mdc5=anm5h285cf6pipf6u05gaeehm7`, accessed June 2021.

[58] S. Modaresahmadi, D. Barnett, H. Baninajar, J. Z. Bird, W. B. Williams, Structural modeling and validation of laminated stacks in magnetic gearing applications, International Journal of Mechanical Sciences 192 (2021) 106133. `doi:https://doi.org/10.1016/j.ijmecsci.2020.106133`.
URL `https://www.sciencedirect.com/science/article/pii/S0020740320342387`

[59] S. Gerber, R.-J. Wang, Analysis of the end-effects in magnetic gears and magnetically geared machines, in: 2014 International Conference on Electrical Machines (ICEM), 2014, pp. 396–402. `doi:10.1109/ICELMACH.2014.6960211`.

[60] eurostat - Statistics Explained, Electricity price statistics, `https://ec.europa.eu/eurostat/statistics-explained/index.php?title=Electricity_price_statistics#Electricity_prices_for_non-household_consumers`, accessed June 2021.

[61] Trading Economics, Neodymium, `https://tradingeconomics.com/commodity/neodymium`, accessed June 2021.

[62] SMM, Dysprosium price charts, `https://www.metal.com/Rare-Earth-Metals/201102250389`, accessed June 2021.

[63] Arnold Magnetic Technologies, The important role of dysprosium in modern permanent magnets, `https://www.arnoldmagnetics.com/wp-content/uploads/2017/10/Important-Role-of-Dysprosium-in-Modern-Permanent-Magnets-150906.pdf`, accessed June 2021.

[64] The Engineering ToolBox, Emissivity coefficient materials, `https://www.engineeringtoolbox.com/emissivity-coefficients-d_447.html`, accessed June 2021.

[65] Young, Freedman, Univerity Physics with Modern Physics, Pearson Education, 2008.

[66] Space Material DataBase, Grain-oriented electrical steel, `https://www.spacematdb.com/spacemat/manudatasheets/crgo.pdf`, accessed June 2021.

[67] Infineon, Ipm 3-phase inverter simulator, `https://plex.infineon.com/plexim/ipmmotor.html`, accessed June 2021.

[68] Fisher Elektronik, Standard extruded heatsinks, `https://www.fischerelektronik.de/web_fischer/de_DE/K%C3%BChlk%C3%B6rper/A01/Standardstrangk%C3%BChlk%C3%B6rper/$catalogue/fischerData/PG/SK405/search.xhtml`, accessed June 2021.

[69] S. S. Nielsen, H. Y. Wong, H. Baninajar, J. Z. Bird, P. O. Rasmussen, Pole and segment combination in concentric magnetic gears: Vibrations and acoustic signature, Submitted to IEEE Transactions on Energy Conversion.

Paper A

Conveyor System with a Highly Integrated Permanent Magnet Gear and Motor

S. S. Nielsen, R. K. Holm & P. O. Rasmussen

Department of Energy Technology, Aalborg University,
Pontoppidanstraede 111, 9220 Aalborg East, Denmark

Published in:
Journal: IEEE Transactions on Industry Applications, Vol. 56, No.3, May/June 2020
doi: 10.1109/TIA.2020.2977877

S. S. Nielsen, R. K. Holm & P. O. Rasmussen
"Conveyor System with a Highly Integrated Permanent Magnet Gear and Motor"
IEEE Transactions on Industry Applications
May/June 2020

The layout has been revised.

Conveyor System With a Highly Integrated Permanent Magnet Gear and Motor

Simon Staal Nielsen, Rasmus Koldborg Holm, and Peter Omand Rasmussen

***Abstract*—Magnetic gears have attracted increasing attention in recent years due to many possible advantages over mechanical gears. Many papers have been presented with theoretical proof of the basic properties and topologies of the magnetic gears and their parallels to mechanical counterparts. However, very little work has been done to implement the magnetic gears into actual applications which fully utilizes their desirable properties. This article presents a concept study and physical demonstrator of a magnetic gear and permanent magnet machine highly integrated into a drive unit for chain conveyor systems. Several current mechanical gear/motor combinations are replaced by the new drive unit, which is more compact and potentially more energy efficient. Moreover, the inherent overload protection of the magnetic gear eliminates the need for a mechanical slip clutch in the system, further reducing system complexity and improving reliability. An experimentally measured torque density of 142 N·m/L is obtained for the active magnetic gear volume.**

***Index Terms*—Conveyor, drive unit, industrial application, integration, magnetic gear (MG), torque density.**

I. INTRODUCTION

DURING the last 15 years, the magnetic gears (MGs) have turned into quite a hot topic in academia due to its many advantages of no mechanical wear, physical isolation of load from drive (which can be exploited in e.g., pump applications), reduced maintenance, potentially good efficiency, inherent overload protection, reduced acoustic noise from mechanical contact, and the absence of backlash. Even though MGs have been a known technology the whole 20th century, its potential was first made clearly visible in the paper [1] where a theoretically calculated torque density of 100 N·m/L was presented. The paper uses the wording novel in its title which can be considered unfair since the presented topology was exactly the same as the one described by Martin [2] in a patent from 1968. At that time, strong rare earth magnets were not available making the torque density of the MG impractical for a more widespread use of the technology at that time. In the early years of the technology, the focus was mainly to describe the basic functionality, making demonstrators to prove the principle, compare it to conventional gears, presenting different topologies, etc., [1], [3]–[9]. Since the MG to a very large extent will/can be driven by electrical machines, and the research and the basics of these machines has been covered extensively, many turned into looking to combine/integrate the MG and electric machine. Several papers in that area saw its daylight [10]–[12], while the research of understanding more of its details in the form of optimization, cogging torque, three-dimensional (3-D) effect, etc., continued. Even though a lot of academic work is done in the field, the real commercial breakthrough has not arrived although it could have been expected. The delay may be attributed to recent sky-high magnet costs, and also likely to the fact that the technology has not been demonstrated in real, highly relevant applications. For instance, in [13] very good results were shown in terms of energy efficiency and torque density, but the implementation had drawbacks as solid steel was used for the segments. The result is an operating speed too low for other than a few, very specialised applications. On the other end, [14] presents a motor integrated permanent magnet gear (MIPMG) for a traction application. This MG and motor combination runs at very high speed which leads to large rotational losses. Although a large amount of work has been done to reduce these losses, and better results were obtained, the cost of the MG and motor also increased. If the range between the two examples is considered, several applications which fit the MG very well can be found. One example is conveyor belts where the speed is more appropriate, and the special properties of the MG, such as the inherent overload protection, high torque density, minimal maintenance, and potentially high energy efficiency, are perfect matches.

This article presents a highly integrated implementation of the MG into a chain conveyor application. The MG is driven by a permanent magnet synchronous machine (PMSM) and three different configurations are discussed. Both design, physical tests, and evaluation of the systems are presented. The aim is to replace the existing drive unit with a more efficient and compact drive unit, which also replaces several current combinations of line fed induction machines and mechanical gearboxes covering the speed and torque ranges required by customers. Furthermore, this article contributes to link the extensive academic activities in the MG area to actual industrial applications. Section II discusses the topology of the MG and PMSM configuration and Section III describes the development of the demonstrator. In Section IV, the test results and evaluation of the MG and PMSM are given, and finally, the conclusion is given in Section V. An earlier

---

Manuscript received September 24, 2019; revised January 5, 2020; accepted February 26, 2020. Date of publication March 2, 2020; date of current version April 24, 2020. Paper 2019-EMC-1107.R1, presented at the 2018 IEEE Energy Conversion Congress and Exposition (ECCE), Portland, OR, USA, Sep. 23–27, and approved for publication in the IEEE TRANSACTIONS ON INDUSTRY APPLICATIONS by the Electric Machines Committee of the IEEE Industry Applications Society. *(Corresponding author: Simon Staal Nielsen.)*

The authors are with the Department of Energy Technology, Aalborg University 9220, Aalborg, Denmark (e-mail: ssn@et.aau.dk; rkh@et.aau.dk; por@et.aau.dk).

Color versions of one or more of the figures in this article are available online at http://ieeexplore.ieee.org.

Digital Object Identifier 10.1109/TIA.2020.2977877

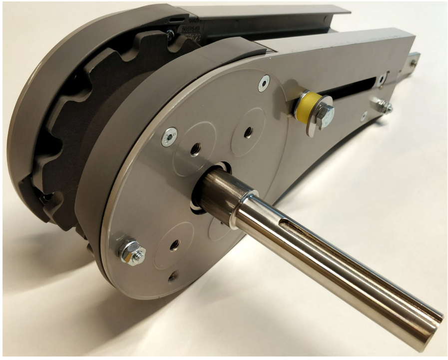

Fig. 1. Current drive unit with polymer sprocket on a shaft, to which an external motor/gearbox combination can be attached.

TABLE I
MAIN CONSTRAINTS AND REQUIREMENTS FOR THE DRIVE UNIT

Max sprocket speed [rpm]	298
Peak sprocket torque [Nm]	100
Nominal sprocket torque (0-12.4 rpm) [Nm]	80.9
Nominal sprocket torque (149-298 rpm) [Nm]	22.7
Max power @ 298 rpm [W]	708
Drive unit width, excl. gear/motor [mm]	85
Max sprocket center diameter [mm]	105
Max diameter of external components [mm]	150
Cooling method	Natural
Target gear ratio	15:1
IP rating	IP65

version of this article was presented on the 2018 IEEE Energy Conversion Congress and Exposition (ECCE) [15].

II. TOPOLOGY OF MG AND PMSM COMBINATION

The new drive unit must fit into a current conveyor system which inevitably introduces some constraints on the system design, such as specific outer dimensions and mechanical interface to conveyor chains. In Fig. 1, the current drive unit is seen. It mainly consists of two aluminum flanges holding a polymer sprocket on a shaft to drive the conveyor chain. An external drive comprised of a motor/gear combination and optionally a frequency converter is attached to the 120-mm long shaft to drive the sprocket.

The new drive unit can only utilize passive cooling, hence, all losses must be dissipated mainly through the aluminum flanges and the units own housing. In Table I, the specifications for the drive unit are outlined.

The target gear ratio is chosen as a compromise between maximum frequencies and the torque requirement of the PMSM. If the rule of thumb for volumetric torque densities of MGs (100 N·m/L) and naturally cooled PMSMs (10 N·m/L) are examined, there is approximately a factor of 10 in favor of the MGs. Hence, to somehow balance the volumetric size of MG and PMSM, there should be a gear ratio of at least 10:1. For the MG topologies with an integrated PMSM, the system may benefit from an even higher gear ratio, as this lowers the torque requirements for the PMSM, which is almost thermally isolated inside the MG and will face difficulties to get rid of the heat generated by losses. The price paid for higher gear ratios is higher frequencies which increases the challenging core- and magnet-losses. With a gear ratio of 15:1, the maximum speed of the PMSM is 4470 r/min. The peak torque requirement is 6.7 N·m and the maximum continuous torque is 5.4 N·m.

The development of the drive unit is divided into two primary stages, where the first stage is used to chose the topology of the MG and motor combination. In this stage, the MGs are designed via 2-D finite-element analysis (FEA) parameter sweeps, and the PMSMs are approximately sized via general sizing rules and motor data from reputable PMSM manufacturers. The topologies which have been considered for the drive unit can be divided into the following three main types:

a) fully integrated, MG is inside sprocket, PMSM is integrated into MG [see Fig. 2(a)];
b) external, MG, and PMSM are on the side of drive unit and designed as an MIPMG [see Fig. 2(b)];
c) semi-integrated, MG is inside sprocket, PMSM is placed on the side of unit [see Fig. 2(c)].

All three topologies have been through several design iterations regarding mechanical integration. Cross sections of the three solutions from the first stage in Fig. 2 are shown in proportion with dimensions in millimeters.

In the fully integrated version, the segment ring is kept stationary, and the sprocket is mounted to the low speed (LS) rotor. The high speed (HS) rotor magnets share back iron with the rotor magnets of the integrated PMSM. This topology has been deemed unfeasible early in the process, despite the very appealing compact form which is the shortest of the three. The gearing ratio is limited to 12:1 due to the size of the magnets and the requirement of a Halbach arrangement of the magnets on the LS rotor to obtain the required torque. This gearing ratio requires a torque density of 27 N·m/L for the passively cooled PMSM which is not manageable for such a small machine which is fully enclosed in the MG. Furthermore, the thermal coupling between MG and PMSM requires a grade of magnets which are rated for higher temperature as the PMSM is pushed very hard.

The external topology has the advantage of a larger diameter and uses the segment ring as output rotor, which increases the gear ratio and torque density. In this particular implementation, it is the volume of the internal PMSM that defines the minimum volume of the combined PMSM and MG. The result is a small required torque density for the MG compared to topology a) and c). For this reason, a Halbach magnet array on the LS rotor is not necessary, making this component more simple. Furthermore, this topology makes it easy to obtain the required IP65 rating, as the LS rotor is stationary. The LS output shaft is easily sealed with a radial shaft seal. The flanges and sprocket can be reused from the existing drive unit. The disadvantages of this topology includes the thermal coupling between MG and PMSM, forces which are transferred through the segment ring and a cup-rotor for the HS rotor/PMSM rotor. The space inside the sprocket is not utilized and the structure placed external to the 85-mm width of the main unit are the widest. It should be mentioned, that the illustration of topology b) in Fig. 2 has not been through

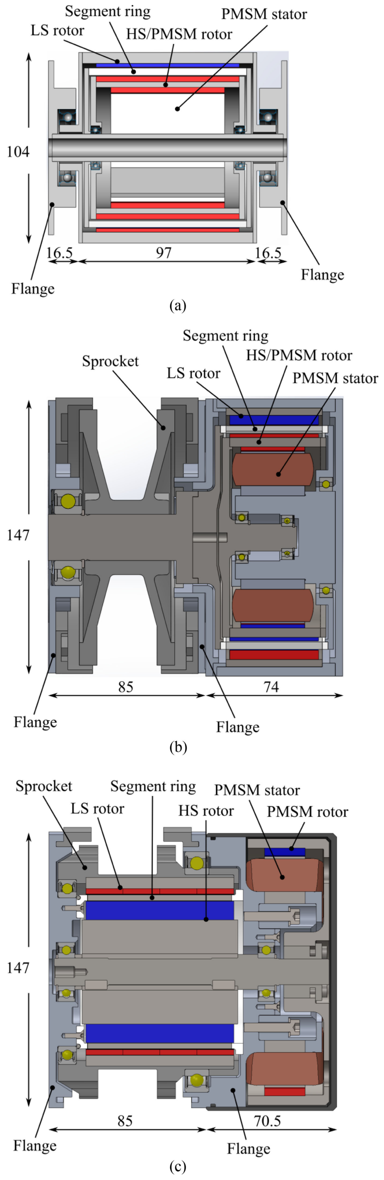

Fig. 2. (a) Fully integrated, (b) external, (c) and semi-integrated topologies. Dimensions are given in mm.

a detailed design phase. A known parameter which would make the final design wider is the space for end windings, at least 8 mm would be added for this reason alone. Also, motor wires must be taken out on the right side of the MIPMG. This increases the effective width of the solution.

The semi-integrated version utilizes the space inside the sprocket for the MG. The segment ring is fixed, and the sprocket is mounted to the LS rotor. The HS rotor shares shaft and bearings with the PMSM rotor, which is an outer rotor machine. This topology introduces a thermal decoupling of the MG and PMSM, hence, the magnet grade of the MG regarding temperature primarily depends on the losses of the MG, and the PMSM may be pushed harder. A better thermal contact can be made to the stator of the PMSM compared to topology a) and b), and the windings are easily accessible for wiring to the inverter through the aluminum flange where the PMSM is mounted. The external placement of the PMSM makes it possible to obtain maximum possible air gap diameter for the given envelope of 150-mm diameter. Finally, this topology does not transfer any load through the segment ring other than the MG torque, and it is mechanically simple. The disadvantages of the topology includes that no existing drive unit components can be reused, large bearings are used which tends to be more expensive compared to some of the bearings used in the other topologies and the design freedom of the MG is reduced compared to the fully external solution.

The semi-integrated solution is chosen. There are few disadvantages to the topology, and they are small compared to the advantages obtained.

III. DEVELOPING THE DEMONSTRATOR

The detailed design of the MG and PMSM is carried out as an iterative process with parameter sweeps. Due to the decoupling between the MG and PMSM, the two designs are made separately. The HS rotor is designed with two pole pairs. This choice has been made to reduce the flux frequency in the MG laminations and to take the constrain on the outer diameter of the MG into account, which causes too small magnets at higher HS pole count at the desired gear ratio when considering mechanical integrity, manufacturability, and flux leakage. With 2 HS pole pairs, the 15:1 gear ratio is obtained with 32 segments and 30 LS pole pairs. The steel segments are connected with a thin bridge as shown in Fig. 3 that improves the segment ring in two areas. First, the bridge has been introduced before in the literature to improve upon mechanical strength and the handling of the segments [11], [16] and second, the bridge reduces the space harmonics of the flux seen by the HS magnets which reduces the eddy current losses induced in these [11], [17].

The primary objective of the parameter sweeps is torque density, although at the same time, manufacturability is important as the drive unit must be feasible in a commercial context. The parameter sweep of the MG is divided into three stages. First, the major dimensions are swept, being radial magnet thickness, radial back iron thickness, and radial segment height. In the second stage, the segment ratio is swept, which defines the relationship between the width of segments and air between the segments, and in the last stage, the HS magnet ratio and the radial thickness of the bridge connecting the steel segments is swept. Finally, demagnetization is investigated by shifting the LS rotor 1 pole which is the most critical position with respect to demagnetization of the LS magnets. To include the influence of end effects on the MG, the final MG is modeled in 3-D FEA.

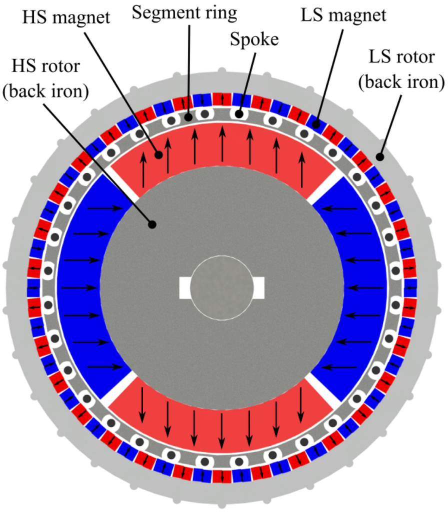

Fig. 3. Cross section of final MG with all practical mechanical aspects applied. Magnetization indicated by arrows.

TABLE II
FINAL DIMENSIONS OF MG

HS pole pairs	2
Nr. of segments	32
LS pole pairs	30
HS radial magnet thickness [mm]	10
HS back iron thickness [mm]	21
LS radial magnet thickness [mm]	3
LS back iron thickness [mm]	5
Segment radial thickness [mm]	3
Segment ratio [-]	0.55
Segment bridge thickness [mm]	0.5
Magnet grades HS/LS	N4520/N4025
HS and LS air gap [mm]	0.4
Stack length, HS + LS [mm]	80
Stack length, Segments [mm]	78
LS outer diameter [mm]	100
Gear ratio	15:1
MG slip torque 2D/3D FEA [Nm]	116/106
MG volume (Active material) [l]	0.628
MG torque density, 3D FEA [Nm/l]	169
External volume added [l]	1.25

Final specifications of the MG are seen in Table II and the cross section of the MG is seen in Fig. 3.

A large challenge in the development of the MG drive is the integration and system design. The most challenging part is the segment ring. The thickness of the bridge in this demonstrator is as small as it is possible to manufacture to minimize the influence on the slip torque although it plays an important role in the structural rigidity of the segment ring. The lamination stack is bonded together with a bonding varnish. By doing this, the segment ring becomes a structural component contributing to a segment ring strong enough to transfer the torque. To fix the segment ring in the MG, the original idea has been to mount the segment lamination stack in an injection molding tool and then overmold the stack, hereby filling the voids between segments with a polymer, and in the same operation mold flanges on each end to attach the segment ring to the aluminum flanges of the drive unit via screws. The segment ring and white polymer flanges are seen in Fig. 2(c). However, due to the high costs related to tooling and the uncertainty of success in the first shot, the alternative construction in Fig. 4 is made. Here, two flanges with fingers fitting in between segments are milled from PEEK, and austenitic stainless steel spokes are used to clamp the lamination stack between the flanges. These spokes are furthermore protruding through the aluminum flange to which this side is mounted and fixed with nuts. Note that the spokes are only electrically short circuited in one end to avoid large circulating currents. This construction is not suitable for manufacturing on a large scale, but it will be sufficient for the demonstrator. The importance of using a nonmagnetic, nonconductive materials for structural parts in the vicinity of the segment ring to avoid reduction in slip torque and excessive rotational losses has been shown in several papers [17], [18]. The slightly shorter stack length of the segment ring is found to yield the highest slip torque, which agrees with the conclusions of [19].

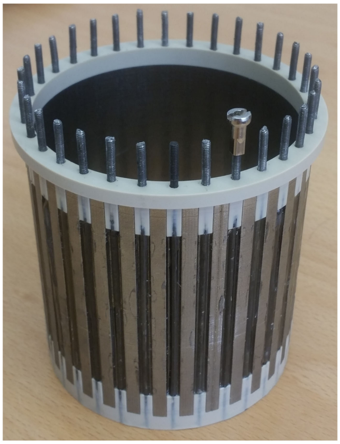

Fig. 4. Segmentring. The spokes are used to clamp the stack between the PEEK end rings and to fix the segment ring to the motor flange.

Like the segment ring, the back iron for the LS rotor is based on a bonded stack of laminations. The outside of this stack is provided with half-round details to transfer the torque from the laminations to the white sprocket made from Polyoxymethylene (POM) (see Fig. 5). The inside is provided with a series of flat sections and protrusions to assist correct placement and a good glue joints between LS magnets and back iron. Each LS pole is divided into four sections in the axial direction as the magnets are very thin, and each pole is furthermore segmented in the tangential direction for reduced magnet loss. Fig. 5 further shows the direction of magnetization for five LS magnets with arrows.

In addition to the construction and manufacturing of the segment ring itself, having three concentric rotors are further complicating the mechanical design of an MG compared to a traditional electrical machine. If all three rotors are positioned

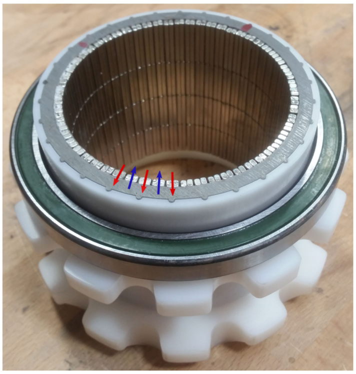

Fig. 5. LS rotor is fixed inside the white POM sprocket, and the torque is transferred via the half round details seen on the outside of the back iron. Direction of magnetization is shown for five LS magnets with arrows.

TABLE III
Final Dimensions of PMSM

Outer rotor diameter [mm]	144
Inner stator diameter [mm]	74
Pole pairs	5
Number of slots	12
Slot opening [mm]	4
Magnet thickness [mm]	4
Magnet ratio	0.96
Back iron thickness [mm]	5
Stator teeth thickness [mm]	10
Stator yoke thickness [mm]	6.5
Stack length [mm]	22
Magnet grade	N3830
Air gap [mm]	0.4
Slot area [mm^2]	300
Fill factor	0.39
Nominal torque @ 5 A/mm^2 [Nm]	6.7
Nominal torque density @ 5 A/mm^2 [Nm/l]	18.7

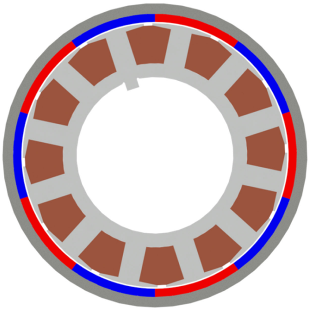

Fig. 6. Cross section of PMSM.

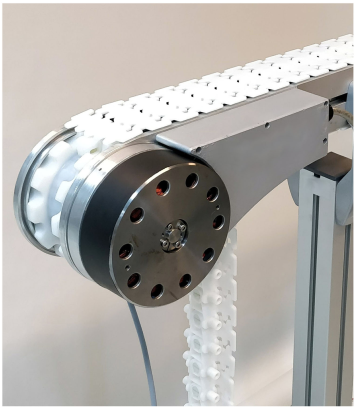

Fig. 7. Demonstrator assembled and mount to the test track. Chain is partly removed to reveal the sprocket.

using a set of end shields, the axial length of the MG which is not actively contributing to torque transfer can become fairly large. In the case of this drive unit, the axial length is reduced by using bearings large enough to enclose the LS rotor and the segment ring. This way, all three rotors can be attached to the two flanges that constitutes the drive unit. As the maximum LS speed is 298 r/min, the mechanical losses in the large bearings will be small. The HS rotor on the other hand can still be suspended in bearings with a smaller diameter to keep these bearing losses low.

The inner diameter of the PMSM stator is kept as large as possible to increase the surface area which transfer the heat generated by the copper- and core-losses in the stator. As the segment ring has been designed with the spokes coming through the motor flange, the depth of the stator slot is limited. If the total length of the drive unit is to be kept as short as possible, the winding will interfere with the spokes if the diameter on the bottom of the slots is to small.

The final motor specifications are seen in Table III and the cross section is seen in Fig. 6. The assembled demonstrator is seen in Fig. 7 with the chain partly removed. The gray enclosure on the side contains the electrical connections for the PMSM. The gray wire hanging below the drive unit is for the rotational encoder which is installed on the left side for test purposes and validation.

IV. Evaluation

In this section, the results of the following tests are presented:
1) rotational loss of PMSM;
2) thermal test of PMSM;
3) rotational loss of drive unit;
4) cogging torque and vibrations;
5) slip torque of MG;
6) efficiency and comparison.

Through these tests, the PMSM is driven by a standard frequency converter with encoder feedback.

A. Rotational Loss and Thermal Test of PMSM

The rotational losses of the PMSM is evaluated via retardation tests. In these tests, the PMSM is accelerated to full speed (4500 r/min) and the power to the PMSM is cut so that the

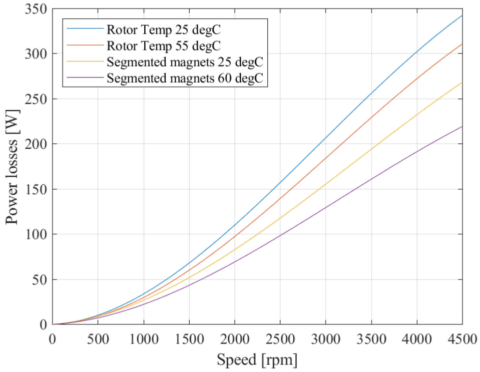

Fig. 8. Rotational loss of PMSM as a function of speed. Original and segmented magnets tested at different temperatures.

TABLE IV
STEADY STATE WINDING TEMPERATURE IN DC TEST

Current density	End winding [°C]	Average [°C]
5 [A/mm^2]	69	78
6 [A/mm^2]	92	104
6 [A/mm^2] w. enclosure	100	112

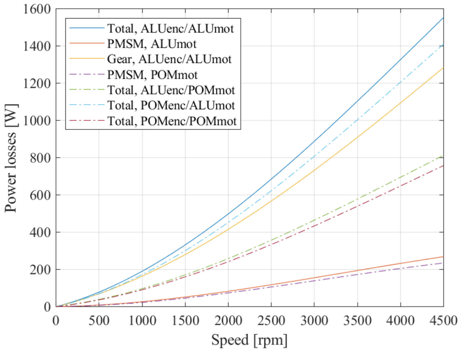

Fig. 9. Losses in surrounding components are separated by retardation tests where different electrically conducting parts are swapped with nonconducting parts.

windings are open circuit. Time and speed are then continuously monitored and logged until standstill of the PMSM and the data are used together with the rotor inertia to calculate the power loss. The results are seen in Fig. 8 and they show rotational losses for the rotor with original magnets which are quite high. To learn more about the location of the rotational losses, the PMSM was run no-load at different speeds while recording the rotor temperature with a thermal camera. The rotor temperature was compared to the temperature of the stator and aluminum flange on which the stator is mounted which were recorded with thermocouples. It was seen that the temperature of the rotor was high compared to the other components, indicating large eddy current losses in the rotor magnets. Another rotor has been build where the magnets are segmented axially into five pieces, and the retardation tests are repeated. The segmentation reduces the rotational losses with 75–90 W at 4500 r/min, depending on magnet temperature, which very strongly indicates that significant eddy current losses are present in the original magnets. The sensitivity to eddy current losses is further shown by a test where the PMSM is running without load at 1000 r/min with the original rotor until steady state temperature is reached. The test is performed with two different inverter carrier wave frequencies of 5 and 10 kHz, where the rotor reaches a temperature of 53 °C and 45 °C, respectively. As the inductance of the PMSM is quite low, the overlaying current ripple of the motor currents is large enough to induce noticeable additional eddy current losses.

To get an indication of the thermal properties of the PMSM stator with respect to dissipation of copper loss, thermal tests are performed with a dc current through the series connected phase windings. The copper temperature is measured with two different methods, one being a thermocouple in an end winding and the other being an indirect method where the temperature rise is found from the increase in winding resistance. The first gives a point temperature in the end winding and the latter gives an average winding temperature. The first test is performed with a current density of 5 A/mm^2 which corresponds to the peak torque of 6.7 N·m that must be delivered during a limited start-up period. The second test is performed at 6 A/mm^2. As the PMSM rotor and electrical connections must be enclosed for safety on the final drive unit the test with 6 A/mm^2 is repeated with printed ABS dummy enclosures installed to see the influence. The measured steady state temperatures are given in Table IV.

The average temperatures in Table IV are higher than the temperature of the end winding which is unusual. However, the thermocouple is placed on the outside of the end winding, hence, a lower temperature must be anticipated compared to a measurement in the center of the end winding. The resulting average temperature of 78 °C at nominal current is promising, and although more sources of loss are added under real operating conditions, the additional frequency dependent losses under maximum torque conditions are limited, as maximum torque is only required below an input speed of 186 r/min. Hence, the 155 °C temperature limit of a class F winding leaves a good margin.

B. Rotational Loss of Drive Unit

To find the rotational losses of the MG, retardation tests are repeated for the complete drive unit, and in Fig. 9, the rotational loss of the PMSM, the MG, and total (PMSM + MG) is shown by solid lines. The test reveals a total rotational loss of 1553 W at the maximum PMSM speed of 4500 r/min, constituted by 269 W in the PMSM and 1284 W in the MG.

The large losses are likely to be caused by eddy currents in the components surrounding the MG, induced by a magnetic leakage field. The leakage field is caused by very strong magnets on the HS rotor configured with only four poles and a fairly thin LS back iron which is highly saturated, and hereby not able to contain the magnetic field. Especially the flange to which the PMSM is mounted is heating up rapidly, and in Fig. 2(c), it

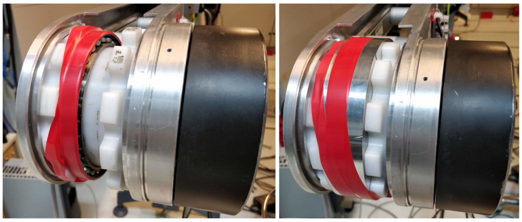

Fig. 10. Two tests performed to locate losses in motor flange. One with extra bearing and one with extra bearing + aluminim.

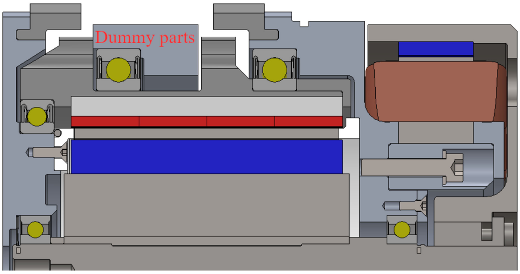

Fig. 11. Cross-sectional view of upper half of the drive unit showing the additional bearing and aluminum section on the sprocket.

TABLE V
Rotational Loss at Full Speed (PMSM @ 4500 r/min) for Different Flange Material Configurations

Configuration	Loss [W]
Total, ALUenc/ALUmot	1553
Total, POMenc/ALUmot	1410
Gear, ALUenc/ALUmot	1284
Total, ALUenc/POMmot	813
Total, POMenc/POMmot	758
PMSM, ALUmot	269
PMSM, POMmot	235

TABLE VI
Derived Rotational Losses in Drive Unit Components at Full Speed (PMSM @ 4500 r/min)

Component	Loss [W]
Aluminium motor flange	666
Aluminium encoder flange	143/55
Bearing, induced	74
Bearing, mechanical	1
PMSM, on POM flange	235
Active MG parts	522

is seen that this flange is overlapping the MG. To demonstrate the leakage field thesis, tests are designed to separate the loss induced by MG and PMSM in each of the major surrounding components by substituting the aluminum flanges with flanges made from POM.

In Fig. 9, the results of these tests are also shown. In the legend the motor flange in aluminum is called ALUmot and the encoder flange in aluminum is called ALUenc. Likewise, POM is used when a POM flange is introduced.

In addition to the large volume of aluminum placed radially outside the MG, this space also features a large bearing. To further separate the rotational loss in the motor flange, two tests are made where an additional bearing and an additional bearing together with a piece of aluminum is placed on the sprocket to determine how much the rotational loss increase, see Fig. 10 for experimental setup and Fig. 11 for a cross-sectional cut. From these tests it is found, that at full speed, 74 W of loss is induced in the bearing and that 72 W of loss is located in the material located radially outside the LS rotor. Table V shows the rotational loss at full speed for different flange material configurations. Gear, PMSM, and total denote that the loss is present in the MG, PMSM, or the combined unit. Table VI shows losses in each drive unit component derived from the tests. The rotational loss in the active MG parts, being laminations and magnets, is found by subtracting losses in flanges, bearings and PMSM from the total loss. The mechanical loss of the large bearing is found through a bearing calculator from the manufacturer, SKF. It is clearly seen that the majority of the rotational loss is found in the motor flange and the active MG parts. From the tests with additional aluminum placed on the sprocket it was found that only 72 W of loss was induced in this section. Also, in Table V, results are shown from two tests with the PMSM mounted on an aluminum flange and a POM flange. These tests show that the PMSM is inducing 34 W of loss in the aluminum flange. These losses are assumed to be induced in the same part where the 72 W were induced by the MG, as the windings are open circuit during retardation tests, hence, no current is running in the windings to induce losses in the aluminum nearby. Also, the PMSM rotor back iron is quite saturated, hence, leakage fields must be anticipated. If the assumptions above are correct, the remaining loss must be induced in the central parts of the motor flange between MG and PMSM.

An interesting observation is made when comparing the encoder flange loss at full speed from tests in different flange material configurations. In Table VI, two different losses are given, depending on how the number is derived. When comparing the rotational loss with two aluminum flanges with the rotational loss were the encoder flange is made from POM (“Comparison 1”), there is a difference of 143 W. However, if the rotational loss in a configuration with aluminum encoder flange/POM motor flange is compared with a configuration with both flange made from POM (“Comparison 2”), a difference of 55 W is obtained. The difference may be explained by losses induced in a current-loop constituted by motor flange, two spacers between flanges, encoder flange, HS shaft, and bearings. As this loop goes though the HS rotor, it links a varying flux which induces a voltage in the loop. To investigate this theory, retardation tests are performed with one spacer in POM and the other changing between aluminum and POM to break the electrical path. A configuration with to different spacer materials is seen to the left in Fig. 12. Three tests in each configuration are made, and at full speed, the average loss of the tests with electrically isolated flanges is 17 W lower compared to the average loss with electrically connected flanges. To further confirm this result, the two otherwise electrically isolated flanges are connected with a

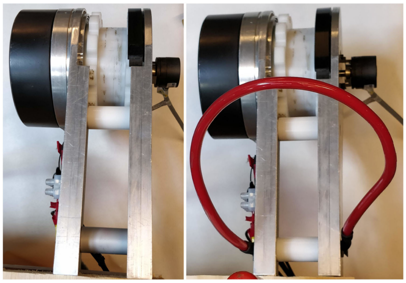

Fig. 12. Left: Upper spacer in POM and lower spacer in aluminum. Right: Both spacers in POM, flanges connected electrically by wire.

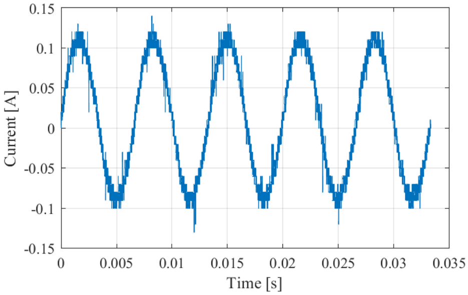

Fig. 13. Current in spacer at full speed.

wire in which the current is measured at full speed, the wire is seen to the right in Fig. 12 and the measured waveform is seen in Fig. 13. The frequency of the current matches the frequency of the magnetic field on the HS rotor. This confirms the hypothesis with a current induced in the path described, and the retardation tests indicate that a loss due to this current is present. This observation is not only relevant to reduce the rotational losses in the MG. It also shows that a current is running through the HS bearings which may be even more important, as bearing currents are known to reduce bearing life and hence, must be avoided [20].

C. Cogging Torque and Vibrations

Turning the HS shaft of the MG reveals a large cogging torque. The cogging torque has an amplitude of 2.5 N·m which is measured by mounting an arm to the HS rotor and pulling at a certain radius with a force transducer. This is very close to what can be predicted by the FE model with the LS rotor in neutral position (see Fig. 14). The cogging torque is directly transferred as vibrations and acoustic noise to the conveyor system. The correlation between cogging frequency and vibrations is established by measuring the vibrations on the main beam on which the conveyor chain is riding, as well as on the chain itself. The vibrations are measured by a 2-axis accelerometer with a sample frequency of 10 kHz. From an FFT analysis of the vibrations, it is clearly seen that the main component in the spectrum is coinciding with the cogging frequency. This is not acceptable and must be avoided on a future version. The cogging torque is a result of the pole configuration and the integer gear ratio. The least common denominator between HS pole pairs and number of steel segments in the segment ring is 32 which is too low, and this issue must be seen as an inadvertent mistake during design. If the number of segments is altered to 33 and the number of LS pole pairs is increased to 31, the torque ripple is decreased to 0.05 N·m. According to 2-D FEA, the slip torque is reduced by 0.49 N·m which is acceptable. According to [21], the use of an uneven number of segments may result in unbalanced radial forces. This is indeed the case, as an unbalanced radial force on the segment ring of 75 N appears, however, this is low and may be allowable. In any case, by changing the pole and segment configuration there is a straight forward solution to the problem in a future version.

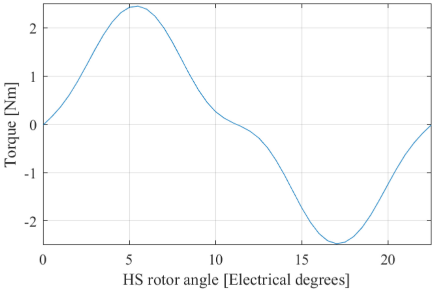

Fig. 14. Calculated cogging torque of HS rotor from the 2-D FE model.

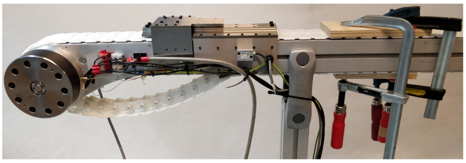

Fig. 15. Test setup for measuring slip torque.

D. Slip Torque of MG

The slip torque of the MG is not readily measurable as no shaft is present on the LS rotor. However, the LS torque can be derived from the chain tension. The test setup seen in Fig. 15 has been build to measure the slip torque.

A linear guide rail constrains the motion of the drive unit in relation to the main beam of the conveyor system. Only movement in the chain direction is possible, and the forces in this direction between drive unit and main beam goes through a load cell. The chain is fixed on the main beam by the clamps, and the HS rotor is rotated until slip occurs. In Fig. 16, the torque from the test of slip torque is seen. Maximum torque achieved is 89 N·m.

From 3-D FEM, 106 N·m was expected and the deviation may be attributed to a couple of sources of error. The BH curve for the

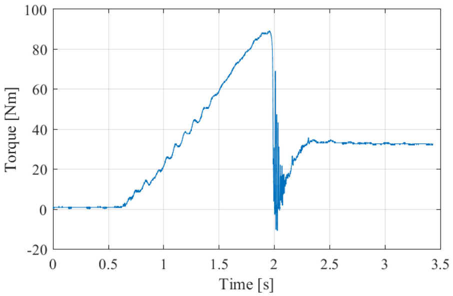

Fig. 16. Measured LS torque from slip torque test.

laminations in the MG is only known up to 2.1 T. As especially the LS back iron is under very hard saturation, above 2.4 T, the extrapolation of the BH curve has influence on the result. Also, when modeling the MG, a homogeneous air gap of 0.4 mm has been used. However, in the demonstrator, half of the air gap is 0.4 mm and the other half is 0.5 mm due to the segmented LS magnets and the way they are physically positioned (see Fig. 5). Also, as the LS magnets have a rectangular cross section, air pockets are formed between the LS poles, hence, less magnet material is present in the real world. When modeling the exact LS rotor geometry in 2-D, the slip torque is reduced by 4.5 N·m

A measured slip torque of 89 N·m yields an actual torque density of 142 N·m/L for the active part of the MG. To close the loop and to compare the chosen semi-integrated topology to the external topology in Fig. 2(b), the volume which is essentially added to the original drive unit in Fig. 1 is evaluated. The semi-integrated solution adds 1.25 L which primarily consist of PMSM and aluminum structure. The torque density of this external volume is 71.2 N·m/l which can be used to compare the semi-integrated topology to the external topology. To the best knowledge of the authors, an actual torque density of 71.2 N·m/L for the total volume has not been published for an MIPMG. As an example, the MIPMG in [14] has a torque density of 99.7 N·m/L for the active materials, however, the torque density decreases to 63.9 N·m/l when the total volume is taken into account. Hence, by choosing topology c) the most compact solution is obtained. On top of that, topology c) has a large benefit of the thermal decoupling between MG and PMSM as discussed.

E. Efficiency and Comparison

The efficiency is measured for the demonstrator and compared to the efficiency of an existing commercial low speed/high torque drive. The efficiency is measured as a system efficiency, given by

$$\eta = \frac{P_{\text{chain}}}{P_{\text{grid}}}. \tag{1}$$

P_{chain} is obtained as the product of the chain force and the chain speed, which is measured with an encoder wheel. P_{grid} is measured with a power analyser.

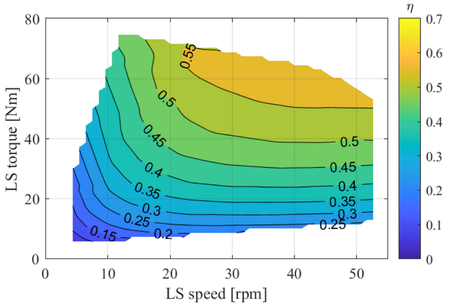

Fig. 17. Efficiency map of demonstrator.

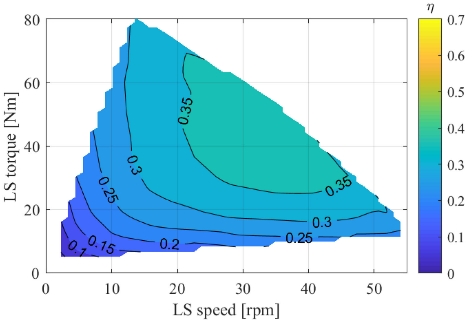

Fig. 18. Efficiency of current LS/high torque drive unit.

The commercial drive consists of an induction machine geared with a worm gear. The induction machine is driven by a frequency converter directly mounted to the motor. The standby power consumption of this combination is 3 W while the standby power consumption of the frequency converter used to drive the demonstrator is 15 W due to many additional functionalities. Hereby, the commercial drive in the comparison will have some advantages.

Fig. 17 shows the efficiency map for the demonstrator. The large rotational losses of the demonstrator makes it undesirable to run it at high speed, hence, the maximum LS speed is limited to 52 r/min which is the same as the maximum speed of the commercial drive. The peak efficiency of the demonstrator is 59.9%. The negative slope of the contour lines at low speed show the low dependence of MGs on load.

Fig. 18 shows the efficiency map of the commercial drive. The peak efficiency in the operating area of this drive is 37.7%. Even though the rotational losses of the magnetically geared demonstrator has been shown to be very large, the efficiency is overall significantly higher than the commercial drive, and the peak efficiency of the demonstrator is 22.2 percentage points, or 58.9%, higher. In addition, when mounted to the shaft of the drive unit seen in Fig. 1, the commercial drive adds 11.6 L of volume to the system compared to 1.25 L for the demonstrator. Both volumes exclude the frequency converter.

V. CONCLUSION

This article presents an MG highly integrated with a PMSM into a conveyor chain drive unit with the aim of replacing the existing solution comprised of several combinations of line fed induction machines and mechanical gears required to obtain the torque and speed characteristics for specific applications. A semi-integrated solution is chosen where the MG is inside the sprocket driving the chain, and the PMSM is on the side of the drive unit. The new drive unit is much more compact than the current motor/gear combination and a measured output torque of 89 N·m is obtained which fulfills the continuous torque requirement of 80.9 N·m, but is 11 N·m lower than the peak torque requirement of 100 N·m. A measured volumetric torque density of 142 N·m/L is obtained for the active parts of the MG.

Large rotational losses are present in the MG and PMSM. The origin of these losses are mainly surrounding aluminum flanges and MG components. Also, a bad pole configuration has been chosen with a large cogging torque as a result. However, despite the large losses, the efficiency map of the drive unit show good tendencies compared to a presently used commercial drive unit. The efficiency of the demonstrator in general is significantly better, and the peak efficiency is 22.2 percentage points higher compared to the commercial drive unit, while reducing the additional volume added to the original drive unit from 11.6 to 1.25 L. The issues with losses and cogging torque can be solved, and the highly integrated drive unit generally shows promising results.

REFERENCES

[1] K. Atallah and D. Howe, “A novel high-performance magnetic gear,” *IEEE Trans. Mag.*, vol. 37, no. 4, pp. 2844–2846, Jul. 2001.

[2] T. B. Martin, “Magnetic transmission,” U.S. Patent 3378710, Apr. 16, 1968.

[3] P. O. Rasmussen, T. O. Andersen, F. T. Joergensen, and O. Nielsen, “Development of a high performance magnetic gear,” in *Proc. 38th IAS Annu. Meeting Conf. Rec. Ind. Appl. Conf.*, 2003, vol. 3, pp. 1696–1702.

[4] K. Atallah, S. D. Calverley, and D. Howe, “Design, analysis and realisation of a high-perfomance magnetic gear,” *IEEE Proc. Elect. Power Appl.*, vol. 151, no. 2, pp. 135–143, Mar. 2004.

[5] S. Mezani, K. Atallah, and D. Howe, “A high-performance axial-field magnetic gear,” *J. Appl. Phys.*, vol. 99, 2006, Art. no. 08R303.

[6] C.-C. Huang, M.-C. Tsai, D. G. Dorrell, and B.-J. Lin, “Development of a magnetic planetary gearbox,” *IEEE Trans. Mag.*, vol. 44, no. 3, pp. 403–412, Mar. 2008

[7] F. T. Jørgensen, T. O. Andersen, and P. O. Rasmussen, “The cycloid permanent magnetic gear,” *IEEE Trans. Ind. Appl.*, vol. 44, no. 6, pp. 1659–1665, Nov./Dec. 2008.

[8] J. Rens, K. Atallah, S. D. Calverley, and D. Howe, “A novel magnetic harmonic gear,” *IEEE Trans. Ind. Appl.*, vol. 46, no. 1, pp. 206–212, Jan./Feb. 2010.

[9] L. Jian and K. T. Chau, “A coaxial magnetic gear with Halbach permanent-magnet arrays,” *IEEE Trans. Energy Convers.*, vol. 25, no. 2, pp. 319–328, Jun. 2010.

[10] K. T. Chau, D. Zhang, J. Z. Jiang, C. Liu, and Y. Zhang, “Design of a magnetic-geared outer-rotor permanent-magnet brushless motor for electric vehicles,” *IEEE Trans. Mag.*, vol. 43, no. 6, pp. 2504–2506, Jun. 2007.

[11] P. O. Rasmussen, H. H. Mortensen, T. N. Matzen, T. M. Jahns, and H. A. Toliyat, “Motor integrated permanent magnet gear with a wide torque-speed range,” in *Proc. IEEE Energy Convers. Congr. Expo.*, 2009, pp. 1510–1518.

[12] K. Atallah, J. Rens, S. Mezani, and D. Howe, “A novel “pseudo” direct-drive brushless permanent magnet machine,” *IEEE Trans. Mag.*, vol. 44, no. 11, pp. 4349–4352, Nov. 2008.

[13] K. K. Uppalapati, W. Bomela, J. Z. Bird, M. Calvin, and J. Wright, “Construction of a low speed flux focusing magnetic gear,” in *Proc. IEEE Energy Convers. Congr. Expo.*, 2013, pp. 2178–2184.

[14] T. V. Frandsen *et al.*, “Motor integrated permanent magnet gear in a battery electrical vehicle,” *IEEE Trans. Ind. Appl.*, vol. 51, no. 2, pp. 1516–1525, Mar./Apr. 2015.

[15] S. S. Nielsen, R. K. Holm, and P. O. Rasmussen, “Conveyor system with a highly integrated permanent magnet gear and motor,” in *Proc. IEEE Energy Convers. Congr. Expo.*, 2018, pp. 2359–2366.

[16] N. W. Frank and H. A. Toliyat, “Analysis of the concentric planetary magnetic gear with strengthened stator and interior permanent magnet (IPM) inner rotor,” *IEEE Trans. Ind. Appl.*, vol. 47, no. 4, pp. 1652–1660, Jul./Aug. 2011.

[17] S. Gerber and R.-J. Wang, “Evaluation of a prototype magnetic gear,” in *Proc. IEEE Int. Conf. Ind. Technol.*, 2013, pp. 319–324.

[18] T. V. Frandsen and P. O. Rasmussen, “Practical investigation of end effect losses in a motor integrated permanent magnet gear,” in *Proc. IEEE Energy Convers. Congr. Expo.*, 2015, pp. 4425–4432.

[19] S. Gerber and R.-J. Wang, “Analysis of the end-effects in magnetic gears and magnetically geared machines,” in *Proc. Int. Conf. Elect. Mach.*, 2014, pp. 396–402.

[20] P. L. Alger and H. W. Samson, “Shaft currents in electric machines,” *J. Amer. Inst. Elect. Engineers*, vol. 42, no. 12, pp. 1325–1334, Dec. 1923.

[21] M. Johnson, M. C. Gardner, H. A. Toliyat, S. Englebretson, W. Ouyang, and C. Tschida, “Design, construction, and analysis of a large-scale inner stator radial flux magnetically geared generator for wave energy conversion,” *IEEE Trans. Ind. Appl.*, vol. 54, no. 4, pp. 3305–3314, Jul./Aug. 2018.

Simon Staal Nielsen received the M.Sc. degree in electromechanical systems design from Aalborg University, in 2015. Thereafter, he worked as a Research Assistant for three years with switched reluctance machines, power electronics and magnetic gears. He is currently working toward the Ph.D. degree in systems design and implementation of magnetic gears, electric machines and power electronics with the Department of Energy Technology at Aalborg University.

Rasmus Koldborg Holm was born in 1986. He received the M.Sc. degree in electromechanical engineering from Aalborg University, Aalborg, Denmark, in 2012 and the title of his master’s thesis project was “Design of a Magnetic Lead Screw for Wave Energy Conversion.”

Since then, he continued his work on magnetic lead screws and has also done some work regarding magnetic gears. He is currently working in the field of magnetic lead screws with the Department of Energy Technology, Aalborg University.

Peter Omand Rasmussen received the M.Sc.E.E and Ph.D. degrees from Aalborg University, Aalborg, Denmark, in 1995 and 2001 respectively.

In 1998, he became an Assistant Professor, and in 2002 he became an Associate Professor with the Department of Energy Technology, Aalborg University. His research interests include design and control of switched reluctance machines, permanent magnet machines, and magnetic gears.

Paper B

Magnetically geared conveyor drive unit - an updated version

S. S. Nielsen, R. K. Holm, N. I. Berg & P. O. Rasmussen
Department of Energy Technology, Aalborg University,
Pontoppidanstraede 111, 9220 Aalborg East, Denmark

Published in:
Conference Proceedings: 2018 IEEE Energy Conversion Congress and Exposition (ECCE), 11-15 October 2020, Detroit, MI, USA
doi: 10.1109/ECCE44975.2020.9235375

S. S. Nielsen, R. K. Holm, N. I. Berg & P. O. Rasmussen
"Magnetically geared conveyor drive unit - an updated version"
2020 IEEE Energy Conversion Congress and Exposition (ECCE)
October, 2020

The layout has been revised.

Magnetically geared conveyor drive unit - an updated version

1st Simon Staal Nielsen
Department of Energy Technology
Aalborg University
Aalborg, Denmark
ssn@et.aau.dk

2nd Rasmus Koldborg Holm
Dansk Ingeniørsservice A/S
Skanderborg, Denmark
rasmus.holm@d-i-s.dk

3rd Nick Ilsøe Berg
Silkeborg, Denmark
nickibberg@gmail.com

4th Peter Omand Rasmussen
Department of Energy Technology
Aalborg University
Aalborg, Denmark
por@et.aau.dk

***Abstract*—This paper presents an updated design of a magnetically geared drive unit for chain conveyor applications. The magnetic gear is placed partially inside the sprocket that drives the chain, and the permanent magnet synchronous machine driving the gear is placed axially next to the gear. The first version suffered from very large rotational losses leading to poor efficiency and thermal problems which limited the drive unit to a very low speed if continuous operation were to be sustained. Furthermore, due to a bad pole configuration, large cogging torque was seen on the HS rotor. This paper presents an updated version where the primary focus is to show, that both cogging torque and rotational losses can be reduced to an acceptable level. With a reduction of the rotational losses by a factor of 4.6 and a peak-to-peak cogging torque which has been reduced substantially, the main goals have been achieved. The mechanical integration is also simplified and manufacturability is improved.**

***Index Terms*—Magnetic gear (MG), conveyor, integration, torque density, drive unit, industrial application.**

I. INTRODUCTION

Since 2001, magnetic gears (MGs) have seen increasing interest in academia [1] due to many advantages such as physical isolation of load from drive, inherent overload protection, potentially good energy efficiency, reduced maintenance, no mechanical wear, reduced acoustic noise from mechanical contact and no backlash [2]. In 2001 a milestone paper demonstrated a theoretical torque density of 100 Nm/l [3] which was a cornerstone in MG research as it was an indicator for the impact that the technology could have. Recent results have demonstrated measured torque densities on physical demonstrators as high as 238.7 Nm/l [4] which further shows that the technology has its merits when it comes to competing with the torque density of mechanical gears. To transfer MG technology from academia to real applications, more work needs to be done regarding the implementation of MGs into these applications, as the physical implementation plays a large role with respect to losses, slip torque, cost and construction of the different gear parts etc. In [5] a magnetically geared drive unit for a chain conveyor application is presented (MagCon V1). MagCon V1 has a maximum output speed of 300 rpm which is an interesting speed range with the specific pole configuration used, as the first harmonic of the magnetic frequency is kept at 150 Hz. In [6] a motor integrated permanent magnet gear (MIPMG) designed for traction applications is presented. Good results were obtained, but a lot of expensive materials and intricate design work went into the MIPMG to limit the rotational losses and obtain a thermally feasible design, as the maximum output speed is 1200 rpm at which the fundamental magnetic frequency is 720 Hz [7].

MagCon V1 from [5] is mechanically well functioning but during tests it was only able to deliver a slip torque of 89 Nm. This is enough for the required nominal slip torque of 81 Nm, but short of the 100 Nm peak torque requirement. MagCon V1 inherently has high cogging torque on the high speed rotor (HSR) due to the specific pole configuration which was chosen during design. This translated into acoustic noise and vibrations in the conveyor system during tests. The largest concern, however, with MagCon V1, is the large rotational losses which prevent higher operating speeds for any extended time period due to thermal issues. This paper presents a redesign of the drive unit to reduce cogging torque, increase slip torque and to reduce rotational losses. In Section II, supplementary tests and conclusions on MagCon V1 is presented. Section III presents designs of a new MG and permanent magnet synchronous machine (PMSM). In Section IV, the mechanical implementation is introduced, and in Section V the experimental test results are presented. Finally, Section VI gives the conclusion.

II. EXTENDED TESTS OF MAGCON V1

In [5] it is found, that from a total 1553 W of rotational loss at a HSR speed of 4500 rpm, 666 W are induced in the aluminium flange to which the PMSM stator is mounted, see Fig. 1. 55 W are induced in the encoder flange and 522 W are induced in the active gear parts. 74 W are induced in a large bearing mounted on the outside of the low speed rotor (LSR).

978-1-7281-5826-6/20/$31.00 ©2020 IEEE

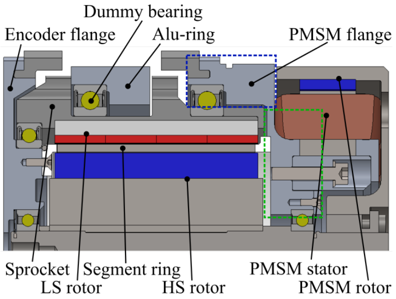

Fig. 1. MagCon V1 cross section with dummy bearing and -flange used during loss tests [5].

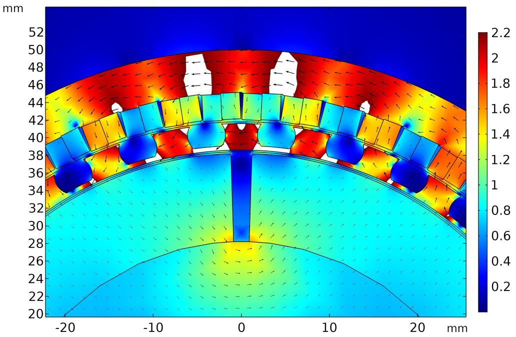

Fig. 2. Flux density in the HS magnets between the segments is different from the flux density directly under the segments which shows a varying flux density in the HS magnets. Color scale is limited and white areas exceed 2.2 T.

This bearing, and a dummy bearing, is seen in Fig. 1 (based on a figure from [5]). The remaining 235 W is rotational losses in the PMSM.

In [5] it is stated, that these large loss components are the result of a very high induction level in the gear parts. In addition to high losses in the active gear parts, the saturated LSR back iron allow large, varying magnetic leakage fields to enter the electrically conducting surrounding components which causes eddy current losses herein. Finally, in [5] large eddy current losses were seen in the surface mount PMSM magnets. As the HS gear magnets are large, solid magnets as well, which rotates inside a segment ring resembling stator teeth with slot openings, it is suspected that eddy current losses are present in the HS magnets. In Fig. 2 a surface plot of the flux density in part of MagCon V1 is shown. It is clearly seen that the flux density in the HS magnets between the segments is different from the flux density directly under the segments. This is especially true near the corners of the HS magnets.

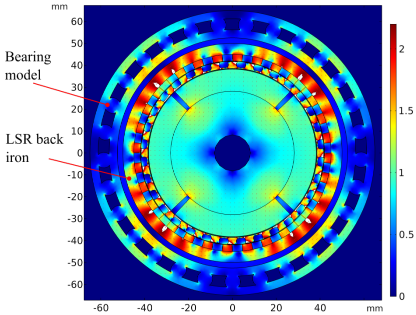

Fig. 3. Flux density plot of first version of the HSR, HSR V1.0.

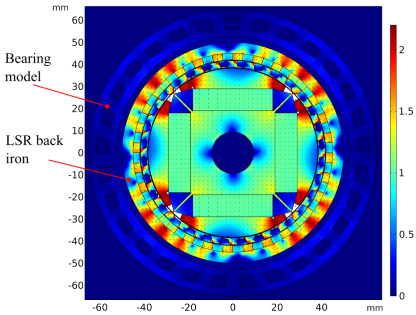

Fig. 4. Flux density plot of the updated version of the HSR with buried magnets and reduced induction level, HSR V1.1.

To prove the hypothesis just stated, a new HSR (HSR V1.1) with buried magnets has been designed to reduce the induction level and eliminate the changing field seen by the HS magnets. HSR V1.1 is made from 0.5 mm M400-50A lamination and the magnets are standard N35 NdFeB magnet blocks. Fig. 3 and 4 show flux density plots of the original (HSR V1.0) and HSR V1.1 with the large bearing added to the model. The bearing is modeled as a magnetic linear material with a relative permeability of 4000, similar to the linear range of electrical steel. As long as the induction in the bearing is kept low, the linear material model will not have influence on the result of the magnetostatic model.

It is clearly seen that the flux density in the LSR back iron and bearing has been reduced. The peak flux density in the bearing has been reduced from 2.37 T with HSR V1.0 to 0.49 T with HSR V1.1. The same sequence of retardation tests that was used in [5] is carried out with HSR V1.1. This entails systematically substituting aluminium flanges with polymer flanges and conducting tests with and without dummy bearing and the additional aluminium ring on the sprocket. The results are summarised in Tab. I, where loss data for HSR V1.0 is obtained from [5]. The measured slip torque of the MG with HSR V1.1 is 43 Nm which is 52% less than HSR V1.0, hence this obviously has to be improved. However, what is important to note from the results in Tab. I is the large reduction in loss for all parts of the gear. What is especially important is losses

TABLE I
ROTATIONAL LOSSES IN DRIVE UNIT COMPONENTS WITH HSR V1.0 AND HSR V1.1 AT A HSR SPEED OF 4500 RPM.

Part	HSR V1.0 [W]	HSR V1.1 [W]
Total loss with alu flanges	1553	487
Alu PMSM flange	740	116
PMSM, on POM flanges	235	235
Bearing, induced	74	0
(Aluminium ring, induced)	(72)	(0)
Alu encoder flange	55	24
Bearing 61821-2RZ, Friction	1	1
Magnetic losses in gear	448	111

in the bearing and the part of the PMSM flange marked by the blue square in Fig. 1. From tests with a dummy bearing and an aluminium ring on the sprocket, it has been determined that no loss is induced in these parts with HSR V1.1. This means that 0.49 T can be used as a reference for the flux density in the bearing when modeled as seen in Fig. 4. This knowledge is applied during the development of the new MG. Finally, in [5] it is noted that only a small part of the losses in the PMSM flange is induced in the area marked by the blue square (approximately 72 W), hence the majority of the loss in this flange must be induced in the part marked by the green square.

III. REVISED MAGNETIC DESIGN

Two approaches are followed to reduce the magnetic stray fields outside the gear in the initial design stage. In the first approach, the low torque requirement for the PMSM is maintained with a 4 HS pole configuration and high gear ratio. The second approach investigates a 6 HS pole configuration. If every dimension in the gear is kept constant, the induction level in the LSR back iron will be lower with 6 HS poles compared to 4 HS poles, hence with the same LSR back iron thickness, the stray fields will be reduced. However, to avoid excessive core losses, the gear ratio must be reduced with 1/3 to keep the same fundamental frequency of the flux, which is 150 Hz at 4500 rpm for MagCon V1.

In [8] it is shown how the torque density can be increased with higher HS pole numbers, and a similar trend is seen in Fig. 5 where results from simulations of MG's for the application of this paper is shown. For the simulations behind Fig. 5 only the pole numbers have been changed while all other dimensions have been kept constant. The LSR back iron is also kept constant, but thick enough to eliminate the influence of saturation at low HS pole count. Hence, Fig. 5 is not representing optimised designs, but it shows tendencies with respect to pole number and gearing ratios. It is seen that the optimal gearing ratio for a 4 HS pole configuration is 13-14 which matches the gearing ratio of 15:1 for MagCon V1 well. It is also seen, that for a 6 HS pole design, the optimal gearing ratio is around 9, hence, reducing the gear ratio of MagCon V1 with 1/3 to around 10:1 to maintain the fundamental frequency fits very well with the optimum gear ratio where the highest torque density is obtained.

A 2D FE model is used for the MG design. To account for end effects the targeted slip torque in the 2D FEM model is increased with 30 % based on the results from [5], hence 130 Nm is required in the simulations. All the initial simulations are performed with ideal LS magnets without any air between and square segments in the segment ring. The segments are connected with a bridge on the inner diameter. Other common parameters are seen in Tab. II. These simulations are used to compare the tendencies seen in the different MG topologies. Before the final design is locked, more details are added to the geometry of the model, and smaller details of the design are investigated.

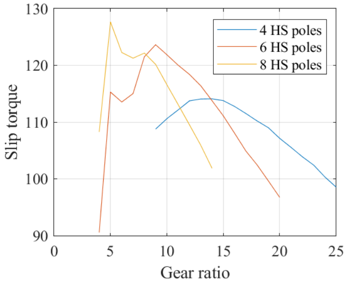

Fig. 5. Sweep of gear ratios with different HS pole number.

TABLE II
COMMON PARAMETERS FOR INITIAL INVESTIGATIONS OF MG TOPOLOGIES.

LSR radial magnet thickness [mm]	3
Segment radial thickness [mm]	3
Segment ratio (outer diameter) [-]	0.55
Segment bridge thickness [mm]	0.5
Magnet grades HS/LS	N4520/N4025
HS and LS air gap [mm]	0.4
Stack length (All rotors) [mm]	80
LSR outer diameter [mm]	100

A. *4 HS poles*

The MG in MagCon V1 suffered from a cogging torque of 5 Nm peak-to-peak on the HS rotor due to the pole configuration. To remedy this in the new design, the number of segments is decreased from 32 to 31, and the number of LS poles is decreased from 60 to 58, hereby obtaining a gear ratio of 14.5:1 for which a continuous torque of 5.6 Nm is required from the PMSM. With all other parameters than the pole numbers being identical to the MG in MagCon V1, this reduces the HSR cogging torque to 0.034 Nm at maximum load which is less than 0.5%.

The parameters with the largest influence on the induction level in the LSR back iron is the back iron thickness and the strength of the HS magnets. Fig. 6 shows a surface plot of the gear slip torque (80 mm stack length has been maintained) as a function of the two parameters. The white isocurve indicates the limit for the flux density in the bearing which was found in Sec. II, and every design point to the right of this isocurve is

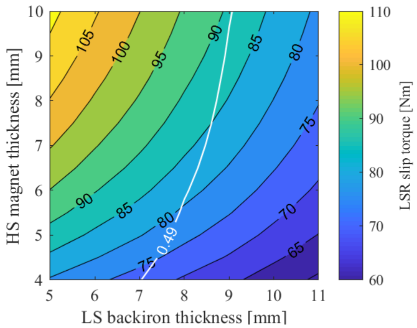

Fig. 6. Sweep of radial LSR back iron thickness and radial HS magnet thickness.

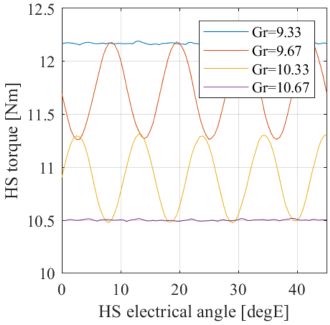

Fig. 7. HS cogging torque of the considered pole configurations.

feasible. It is clearly seen that from the feasible design points, the highest slip torque is obtained by maintaining 10 mm HS magnet thickness and increasing the LSR back iron thickness to 9.1 mm. At this design point, the slip torque is 88 Nm, hence the stack length is increased from 80 mm to 118 mm to reach the design target of 130 Nm.

B. 6 HS poles

Two different MG's with 6 HS poles have been considered. The first MG is designed with surface mounted HS magnets to obtain a direct comparison to the surface mounted 4 HS pole design. The second MG is designed with buried HS magnets like the additional HS rotor which were tested in Sec. II. MG's with buried HS magnets in different configurations have been build and tested with success in prior art, [9] [10], and advantages such as very good mechanical retention of the magnets and simple, square magnets which reduces the number of unique parts for the MG have been highlighted. More recently, the flux concentrating properties of buried magnets in the form of a spoke type arrangement has been utilised to obtain as high a torque density as possible with very good results [11]. As mentioned in Sec. II, eddy current losses in the HS magnets are furthermore reduced as the flux variations introduced by the segment ring is minimised, which is a significant reason why buried magnets are introduced in the MG described in this paper.

1) Surface mount HS magnets: The starting point for the MG with surface mount HS magnets is dimensions identical with the MG in MagCon V1 as seen in Tab. II, an LSR back iron thickness of 5 mm and a HS magnet thickness of 10 mm. Only the pole configuration is changed. Four gear ratios between 9.33:1 and 10.67:1 has been considered, and in Fig. 7 the HS torque ripple for the different ratios are seen. A gear ratio of 10.67:1 were chosen as a compromise between low cogging torque, highest possible gear ratio to reduce the torque requirement for the PMSM and to limit the magnetic fundamental frequency of the gear. With this gear ratio, the maximum HS speed is 3200 rpm at which the magnetic fundamental frequency is 160 Hz. This gear ratio results in a continuous torque of 7.6 Nm from the PMSM. With 5 mm back iron thickness however, the maximum induction in the bearing is 0.88 T which is too high. Following the same trend which is seen in Fig. 6 with the 4 HS pole MG, the back iron thickness is increased to 6 mm which reduces the maximum flux density in the bearing to 0.43 T which is below the limit. With a stack length of 94 mm the 130 Nm design target is obtained. From this result it is clear that the 6 HS pole design offers an advantage from the perspective of torque density.

2) Buried HS magnets: Fig. 8 shows the MG with buried HS magnets. The MG is shown with the simplified LSR magnets and square segments used for the initial simulations. The model is set up with two main variables: Angle between the two magnets in a V-shape and thickness of the magnets. The remaining geometry is given from these parameters and from a number of fixed constrains. The distance between the two corners of the magnets in the bottom of the V-shape and the distance between the two top-corners of neighboring V-shapes is kept constant at 0.5 mm. The thickness of thin bridges that links the different parts of the HSR laminations are also kept constant at 0.5 mm. This dimension is based on a compromise between structural integrity, minimising leakage flux and manufacturability. From preliminary simulations it is found, that by retracting the corners of the magnets closest to the air gap radially by 2.5 mm, flux variations in the HS magnets are avoided. Lastly, the lamination steel on top of the HS magnets is retracted from the air gap to form small air pockets. This is done to minimise the flux variation this steel is seeing from the slotting effects on the segment ring, hereby reducing HSR core loss. The HS magnet thickness and angle are swept to find a suitable combination. In Fig. 9 HS magnet mass is plotted in a surface plot together with a white isocurve indicating the limit for maximum flux density in the bearing and two red punctured isocurves for an LS slip torque of 100 and 102 Nm. Every design point to the right of the white isocurve is a feasible design point. A HS magnet thickness

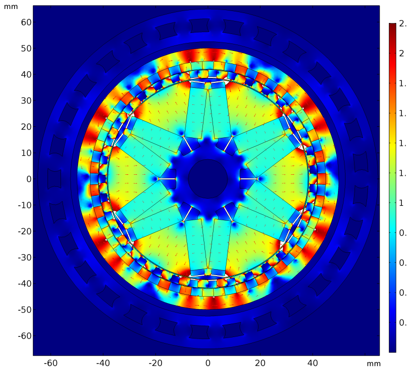

Fig. 8. Flux density plot of MG with 6 HS poles constituted by buried magnets in a flux concentrating V-shape.

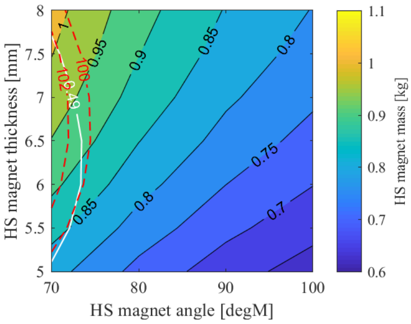

Fig. 9. Sweep of HS magnet angle and thickness.

of 6.5 mm with an angle of 74 degrees is choosen as a good compromise between HS magnet consumption and torque. The HS magnet mass could be increased by 100 gr. but only 1 Nm would be gained. On the other hand, one could argue that 70 gr. could be saved while only sacrificing 1 Nm. However, if Fig. 8 is studied, it is seen, that if a smaller magnet angle is used to obtain either of the two cases, not much space would be left for the shaft in the middle, and the V-shape would begin to resemble a spoke-type implementation, hence a compromise between torque, HS magnet mass and a sound geometry is found with the chosen configuration. This configuration yields a slip torque of 101 Nm, hence the stack length is scaled to 104 mm to reach the 2D FEM design target of 130 Nm.

It is noteworthy that this design need a stack length of 104 mm compared to 94 mm with the 6-pole surface mount version. However, due to the advantages which are obtained with buried magnets, this is what has been chosen as the final HSR topology.

For the final MG the real LS magnets are modelled, and modifications have been done to the segment ring. The LS magnets are implemented as rectangular magnets divided into two which is seen in Fig. 10. The magnet pair is glued together with a 0.1 mm radial shift such that they can be installed correctly on a small matching ridge on the LSR back iron. There is also an air gap between the magnets to take the dimensional tolerance on the magnets into account. The segments have been modified such that a mechanical interlock can be obtained with the cage in which the lamination stack is installed. This is elaborated further upon in Sec. IV. Through a parameter sweep of the inner and outer duty ratio of the segments, their geometry is modified into a trapezoidal shape which increases the slip torque. Finally the thickness of the bridge is increased from 0.5 mm to 0.6 mm to increase the stiffness and structural rigidity of the segment ring. Implementing these modifications have decreased the slip torque slightly from 130 Nm to 125 Nm, but at the point in time where these modifications were made, the mechanical design had already been frozen, hence it was not possible to increase the stack length further. With 125 Nm from the 2D FE model, the expected *measured* slip torque will be 96 Nm. According to the 2D FE model the HS cogging torque at full load is 0.01 %. The final dimensions of the MG is given in Tab. III.

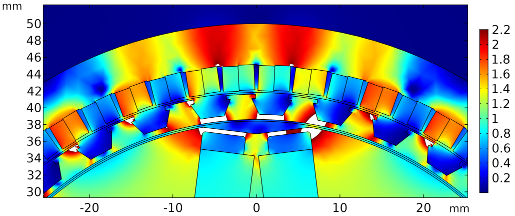

Fig. 10. Flux density plot, final details on segment ring and LSR.

TABLE III
FINAL DIMENSIONS OF MG.

HS pole pairs	3
Nr. of segments	35
LS pole pairs	32
HS magnet thickness [mm]	6.5
HS magnet angle [degrees]	74
LS radial magnet thickness [mm]	3
LS back iron thickness [mm]	5
Segment radial thickness [mm]	3
Segment ratio, inner/outer [-]	0.6/0.28
Segment bridge thickness [mm]	0.6
Magnet grades HS/LS	N45SH/N40UH
HS and LS air gap [mm]	0.4
Stack length, HS + LS [mm]	104
Stack length, Segments [mm]	102
LS outer diameter [mm]	100
Gear ratio	10.67:1
MG slip torque (20 °C), 2D FEA [Nm]	125
MG volume (Active material) [l]	0.817
MG torque density, 2D FEA [Nm/l]	153

3) PMSM: MagCon V1 had a 10 pole, 12 slot PMSM with surface mount magnets, concentrated windings and an outer rotor. This machine were able to deliver the required continuous torque without overheating, however, the efficiency

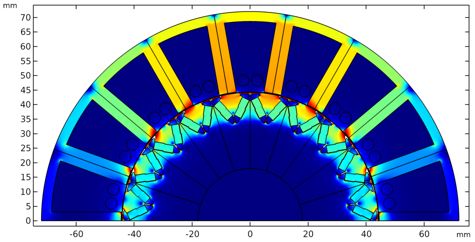

Fig. 11. Flux density in PMSM without stator excitation.

TABLE IV
FINAL DIMENSIONS OF PMSM

Pole pairs	10
Number of slots	18
Outer stator diameter [mm]	144
Stator bore [mm]	89
Stator teeth thickness [mm]	6
Stator yoke thickness [mm]	3.4
Stack length [mm]	30
Magnet grade	N45SH
Air gap [mm]	0.35
Copper fill factor	0.34
Inductance, L_q/L_d [mH]	10.4/7.07
Nominal torque @ 4.1 A/mm^2 (20 °C) [Nm]	7.8
Cogging torque [%]	0.6
Nominal torque density @ 4.1 A/mm^2 [Nm/l]	16

was not very good. Also, from the tests of rotational losses it was clear, that a considerable amount of losses were induced by the MG in the PMSM flange which was necessary to mount the PMSM stator. Finally, for safety reasons, it was necessary with a shield around the rotor which deteriorated the heat dissipating properties, whereas the outer surface of an inner rotor machine either has direct thermal contact to the surroundings or direct contact through the housing. These key points are the motivation for introducing an inner rotor PMSM. The lower speed of the 6 HS pole MG allows for a PMSM with more poles which helps to increase the torque of the machine, hence the PMSM is changed to a 20 pole, 18 slot inner rotor machine with buried V-shaped magnets which is a configuration with very low cogging torque. The buried magnets are introduced for the same reasons as in the gear. Also, the buried magnets allows for an L_q/L_d characteristics that enables sensorless injection techniques. The stator teeth are designed as straight teeth without shoes to enable the use of pre-wound bobbins which will improve the manufacturability of the machine. The PMSM has been designed in MotorCAD which is a commercial motor design software. A flux density plot without any current applied to the stator windings is seen in Fig. 11. Key specifications are given in Tab. IV.

IV. MECHANICAL IMPLEMENTATION

Just like the introduction of bobbins in the PMSM stator, the mechanical integration of MG and PMSM into the new drive unit is done with manufacturing in mind, hence a more modular system with fewer screw connections and less assembly tools compared to MagCon V1 has been a focus point.

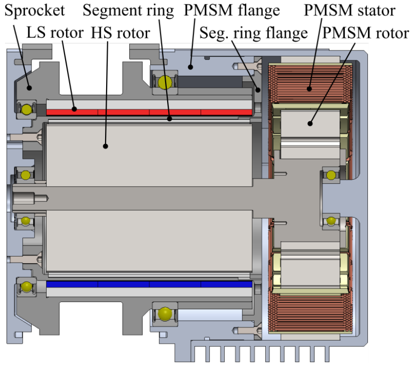

Fig. 12. Cross section of drive unit.

Fig. 13. Segment ring. A cage has been milled from PEEK, and the bonded segment stack is glued in place.

In Fig. 12 it is seen that the centre of the PMSM flange has been removed compared to the PMSM flange seen in Fig. 1 which is important to reduce the eddy current losses. The central part of the PMSM flange is now substituted with a polymer flange to retain the segment ring. As described in Sec. III-B2 the segments are designed with a notch at the outer diameter to enable mechanical interlock to the polymer cage in which it is installed. Fig. 13 shows the segment ring for the demonstrator which is assembled from a bonded lamination stack glued into a cage milled in one piece from PEEK. The glue is a heat curing epoxy with a high operating temperature. The segment ring assembly is then secured to the two aluminium flanges with 6 austenitic stainless screws in each flange.

The demonstrator of MagCon V2 is seen in Fig. 14 where it is mounted in the test stand and the conveyor chain is installed. The final width of the drive unit has been increased with 27 mm to 182.5 mm compared to MagCon V1, primarily due to

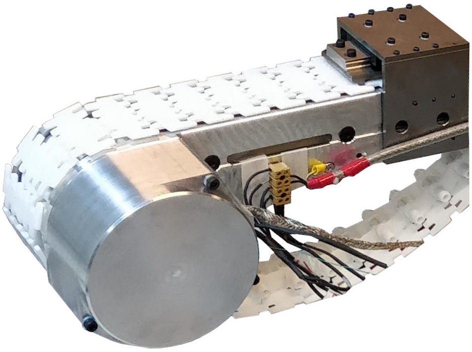

Fig. 14. Demonstrator with conveyor chain mounted in test stand.

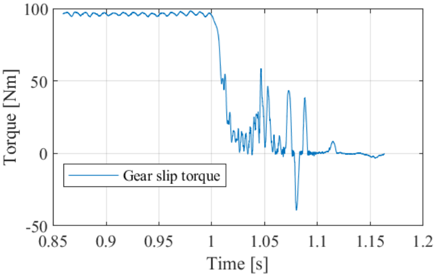

Fig. 15. Measured slip torque. The drive unit is running under load which is increased until slip occurs. Only data close to slip is included in figure.

the longer stack length of the MG.

V. EXPERIMENTAL RESULTS

Fig. 15 shows the LSR torque in a slip torque test. The test is performed by running the drive unit at low speed and increasing the load until slip occurs. The measured slip torque is 98 Nm which is slightly more than expected. This leads to a measured torque density of 120 Nm/l. The torque is measured by logging the chain force with a force transducer in the test stand which is then multiplied by the pitch diameter of the sprocket. Hence, the torque spikes seen during recovery is a result of the dynamics in the test system including stiffness of chain, load machine dynamics and so on.

It is one of the main tasks for MagCon V2 to demonstrate, that the large rotational losses seen in MagCon V1 can be reduced. The rotational losses in MagCon V2 are evaluated with a retardation test where the windings of the PMSM are disconnected from the inverter at full speed, and speed and time is logged. From deceleration and a known inertia of the rotors and gearing, the rotational power loss is calculated as a function of speed. Rotational loss for MagCon V1 and MagCon V2 is seen in Fig. 16. It should be noted that different gear ratios are used, hence rotational losses are shown as a function of chain speed in Fig. 16. The rotational loss for MagCon V2 at full speed, 3200 rpm, is reduced with a factor of 4.6 compared to MagCon V1 at 4500 rpm which is a huge improvement. Even compared to the rotational losses of MagCon V1 with HSR V1.1 where the slip torque was significantly lower, the rotational losses has been reduced by 148 W.

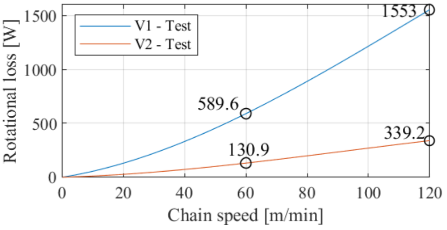

Fig. 16. Rotational losses for first and second version of the magnetically geared drive unit.

339 W of rotational loss is still high, and it is very likely to cause thermal problems, as both LSR back iron and magnets, as well as the segment ring, is embedded in thermally isolating polymer parts. One of the main targets is to make the magnetically geared drive unit as compact as possible which is why it is not desired to increase the physical size to decrease losses and improve heat dissipation. Hence, it is interesting to consider splitting the operating area of the drive unit into a low speed region and a high speed region. The exact speed at which the transition occur is an interesting optimization problem in itself, however, for now, MagCon V2 is considered as a low speed drive unit with an operating speed up to 60 m/min on the chain, corresponding to a PMSM speed of 1600 rpm. In Fig. 17 the rotational loss is separated into MG loss and PMSM loss. The rotational loss in the PMSM is obtained from a separate retardation test, and the MG loss is found as the difference between drive unit loss and PMSM loss. At full speed the bearings for the LSR have combined losses of 15 W according to the bearing models available at SKF. If LSR bearing losses are subtracted from the MG losses it is seen that there are 73.3 W of loss in the active MG parts and the

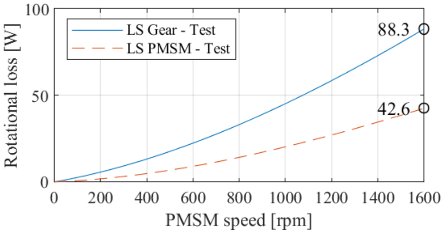

Fig. 17. Rotational losses in MG and PMSM.

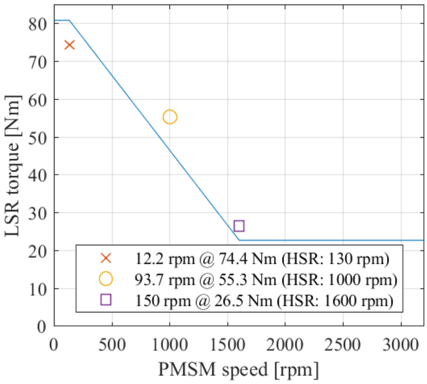

Fig. 18. Thermal steady state tests are performed 3 three different operating points.

surrounding components.

Thermal steady state tests are carried out in three relevant load points indicated in Fig. 18. All tests are at 23 °C ambient. The red cross is low speed and high torque where rotational losses are minimal and copper losses are close to maximum. The test setup is not able to apply full load at this speed due to passive ohmic load on the load machine. As expected the highest temperature is found in the windings which reaches 93 °C after almost 7 hours of running. This is not critical and no sign of failure or additional noises were experienced.

The next load point at 1000 rpm on the HSR is a point where the load is still high and the rotational losses begins to increase. At this point, the highest temperature is still found in the windings which reaches 103 °C. It is notable though, that the second highest temperature is found in the segment ring, measured ind the end of the lamination stack towards the PMSM. Here, the temperature reaches 93 °C. This test did not show any sign of failure either.

The last load point is at 1600 rpm on the HSR, and here the drive unit experienced a break down after 5.5 hours. The highest temperature was found in the segment ring which had reached more than 110 °C at the time the test was stopped. Immediately after stopping the test, the temperature on the outside of the LSR back iron was measured to 79 °C, and the HS shaft temperature was measured to 94 °C. The drive unit was allowed to cool down, and through a retardation test it was found, that the rotational loss had increased with 25 W at 1600 rpm on the HSR. A test of back-emf and MG slip torque revealed that no demagnetization had occurred. After these tests the drive unit was taken apart and it was clear that there was contact between the LSR and the segment ring.

The successful low speed / high torque tests indicate that the structural strength of the segment ring is sufficient. As the segment ring fails in the test at the highest speed where the temperature is the highest strongly suggests that it is a thermal problem. This means that either the cooling must be improved or the losses must be reduced.

VI. CONCLUSION

This paper presents an updated design of a magnetically geared drive unit. The main concerns for the first version of the drive unit, MagCon V1, was large cogging torque on the HSR and large rotational losses. The second version, MagCon V2, has improved these areas substantially, as the HSR cogging torque is very low according to the 2D FE model and the experimentally measured rotational losses has been reduced with a factor of 4.6. The improvements have been obtained through an extensive redesign of the drive unit, where pole configuration, reduced induction levels, buried magnets and strategic removal of surrounding materials have been key factors. The measured torque density of the new MG is 120 Nm/l which is lower than MagCon V1 but still very good compared to what has been obtained in literature. As rotational losses are still deemed too high for the drive unit to operate in the whole operating area it is suggested to split this into a low speed and high speed region. MagCon V2 is covering the low speed region. Thermal tests at low to moderate speed in this region shows promising results, however, at full speed, thermal problems are found.

REFERENCES

[1] P. M. Tlali, R. Wang and S. Gerber, “Magnetic gear technologies: A review, ” 2014 International Conference on Electrical Machines (ICEM), pp. 544–550, September 2014.

[2] P. O. Rasmussen and T. O. Andersen and F. T. Joergensen and O. Nielsen, “Development of a high performance magnetic gear,” 38th IAS Annual Meeting on Conference Record of the Industry Applications Conference, vol. 3, pp. 1696–1702, October 2003.

[3] K. Atallah and D. Howe, “A novel high-performance magnetic gear,” IEEE Transactions on Magnetics, vol. 37, pp. 2844–2846, July 2001.

[4] K. K. Uppalapati and J. Z. Bird and J. Wright and J. Pitchard and M. Calvin and W. Williams, “A magnetic gearbox with an active region torque density of 239Nm/L,” 2014 IEEE Energy Conversion Congress and Exposition (ECCE), pp. 1422–1428, September 2014.

[5] S. S. Nielsen and R. K. Holm and P. O. Rasmussen, “Conveyor System With a Highly Integrated Permanent Magnet Gear and Motor,” IEEE Transactions on Industry Applications, vol. 56, pp. 2550–2559, March 2020.

[6] T. V. Frandsen and L. Mathe and N. I. Berg and R. K. Holm and T. N. Matzen and P. O. Rasmussen and K. K. Jensen, “Motor Integrated Permanent Magnet Gear in a Battery Electrical Vehicle,” IEEE Transactions on Industry Applications, vol. 51, pp. 1516–1525, March 2015.

[7] T. V. Frandsen and P. O. Rasmussen, “Practical investigation of end effect losses in a Motor Integrated Permanent Magnet Gear,” 2015 IEEE Energy Conversion Congress and Exposition (ECCE), pp. 4425–4432, September 2015.

[8] T. V. Frandsen and P. O. Rasmussen, “Slip torque investigation and magnetic redesign of motor integrated permanent magnet gear,” 18th International Conference on Electrical Machines and Systems (ICEMS), pp. 929–935, 2015.

[9] P. O. Rasmussen and T. O. Andersen and F. T. Jorgensen and O. Nielsen, “Development of a high-performance magnetic gear,” IEEE Transactions on Industry Applications, vol. 41, pp. 764–770, 2005.

[10] N. W. Frank and H. A. Toliyat, “Analysis of the Concentric Planetary Magnetic Gear With Strengthened Stator and Interior Permanent Magnet Inner Rotor,” IEEE Transactions on Industry Applications, vol. 47, pp. 1652–1660, 2011.

[11] K. K. Uppalapati and M. D. Calvin and J. D. Wright and J. Pitchard and W. B. Williams and J. Z. Bird, “A Magnetic Gearbox With an Active Region Torque Density of 239 N·m/L,” IEEE Transactions on Industry Applications, vol. 54, pp. 1331–1338, 2018.

Paper C

Pole and Segment Combination in Concentric Magnetic Gears: Vibrations and Acoustic Signature

S. S. Nielsen[a], Ho Yin Wang[b], Hossein Baninajar[b], Jonathan Z. Bird[b] & P. O. Rasmussen[a]

[a] *Department of Energy Technology, Aalborg University,*
Pontoppidanstraede 111, 9220 Aalborg East, Denmark

[b] *Department of Electrical and Computer Engineering, Portland State University,*
1825 SW Broadway, Portland, OR 97201

Submitted to:
Journal: IEEE Transactions on Energy Conversion

Not published, submitted to:

IEEE Transactions on Energy Conversion

The layout has been revised.

Pole and Segment Combination in Concentric Magnetic Gears: Vibrations and Acoustic Signature

Simon Staal Nielsen, *Member, IEEE,* Ho Yin Wong, *Member, IEEE,* Hossein Baninajar, *Member, IEEE,*
Jonathan Z. Bird, *Member, IEEE,* and Peter Omand Rasmussen, *Member, IEEE*

***Abstract*—This paper studies the influence of cogging torque and unbalanced radial magnetic forces on vibrations and acoustic noise properties in concentric magnetic gears. The study involves three physical demonstrators, each with unique properties that make them interesting study cases. The first magnetic gear have pronounced cogging torque due to the pole configuration. In the second magnetic gear very low cogging torque is obtained by choosing an odd number of segments, but at the expense of unbalanced radial magnetic forces. The third gear is designed with a pole configuration that has a good balance between minimizing cogging torque and avoiding unbalanced radial forces. Acoustic and vibrational signatures are presented and the characteristics are discussed in each case. It is shown that both cogging torque and unbalanced radial forces in concentric magnetic gears dominate both acoustic and vibrational properties and it is shown how it makes the magnetic gears very sensitive to the eigenfrequencies of the system.**

***Index Terms*—Cogging torque, unbalanced forces, magnetic forces, vibration, acoustic noise, magnetic gear**

I. INTRODUCTION

CONCENTRIC magnetic gears (CMGs), consisting of an inner rotor, a segment ring and an outer rotor, have seen continuously increasing interest since the turn of the millennium, and the progress made in the field seems to continue to inspire new research on an increasingly higher level. An area that to some degree has received attention from the start is cogging torque which is sought to be minimized. This interest can be seen as a natural consequence of the decades of research and development of electric machines that has preceded magnetic gears (MGs), where cogging is well understood. Cogging torque was actually observed experimentally in what is believed to be the first physical demonstrator of a CMG ever build [1]. It was based on the pole configuration presented in [2] with 4 pole pairs on the inner rotor, p_i, a stationary segment ring with 26 segments, Q, and 22 pole pairs on the outer rotor, p_o. The measured torque curve clearly showed a cogging torque with a fundamental given by the number of segments. A year later, [3] considered the pole configuration in greater depth for a CMG with a stationary segment ring. It was shown via finite element (FE) models, that the pole configuration have large influence on the level of cogging torque, and the cogging torque factor for permanent magnet synchronous machines (PMSMs) introduced by [4] was modified to (1) with $2p_x$ being the pole count (either inner rotor or outer rotor) and Q being the number of segments, and a correlation between the cogging torque and the cogging torque factor was shown.

$$C_T = \frac{2p_xQ}{LCM(2p_x,Q)} = GCD(2p_x,Q) \qquad (1)$$

A lower C_T gives a smaller cogging torque, hence, with a low pole count and a high least common multiplier (LCM) for pole number and segment number, the cogging torque is minimized. Further, [3] showed that the fundamental order of the cogging torque is given by (2) and hence the frequency [Hz] is given by (3).

$$n_{CogMG,x} = LCM(2p_x,Q) \qquad (2)$$

$$f_{CogMG,x} = n_{CogMG,x} \cdot \frac{\omega_x}{2\pi} \qquad (3)$$

Where ω_x is the rotational speed of rotor x $[\frac{rad}{s}]$. This is supported by [5] where an analytic model of the torque in a CMG with stationary segment ring is developed and analyzed. The results from the analytic model are further supported by an FE model and experimental results where n_{cogMG} and the 2$^{\text{nd}}$ harmonic are shown. Reference [5] further shows a cogging torque component related to the segment passing frequency seen from a magnet pole. This fundamental can be related to both the inner and outer rotor, and the fundamental order is given by (4). The frequency is given by (5). This is the cogging torque component which was observed in [1].

$$n_{SegPass} = Q \qquad (4)$$

$$f_{SegPass,x} = n_{SegPass} \cdot \frac{\omega_x}{2\pi} \qquad (5)$$

Finally, [5] show a cogging torque component related to the pole passing frequency seen from a segment. As with (2) and (4), this component can be related to the inner and outer rotor. The fundamental is given by (6) and the frequency is given by (7).

$$n_{PolePass,x} = 2p_x \qquad (6)$$

$$f_{PolePass,x} = n_{PolePass,x} \cdot \frac{\omega_x}{2\pi} \qquad (7)$$

The frequency of (3) and (7) are independent of which rotor is considered, while the frequency of (5) is depending on whether it is the inner rotor or the outer rotor that is considered.

In the academic literature it is well documented that choosing a fractional gear ratio will result in minimal cogging torque [3] [6]. The cogging torque factor, C_T, has been a common

Simon Staal Nielsen (e-mail: ssn@et.aau.dk) and Peter Omand Rasmussen (e-mail: por@et.aau.dk) are with the Institute of Energy Technology at Aalborg University, Denmark.

Ho Yin Wong (e-mail: h28@pdx.edu), Hossein Baninajar (e-mail: hossein@pdx.edu) and Jonathan Z. Bird (e-mail: bird@pdx.edu) are with the Department of Electrical and Computer Engineering at Portland State University, USA.

way to evaluate the cogging torque properties of a given pole configuration, and choosing $C_T = 1$ yields the lowest cogging torque, as this means, that there is no symmetry in the magnetic circuit. One way of obtaining this is to use an odd number of segments. However, it is also well known, that a pole configuration without symmetry results in unbalanced radial forces in the MG. Unbalanced radial forces can be avoided by fulfilling $C_T \geq 2$, hence a compromise between cogging torque and unbalanced radial forces must be found [7] [8]. This metric is fulfilled with an equal number of segments which is often recommended as a starting point for gear designs to avoid unbalanced radial forces [7] [8] [9].

Intuitively, the various cogging torque components and unbalanced radial forces are undesirable for several reasons, including increased mechanical stress on the MG component, vibrations and acoustic noise. In [10] forces on the different rotors in a magnetic gear are obtained through an FE model and used as input to an analytical mass-spring-damper model to predict the deflection of the different rotors. This MG has an odd number of segments, and strong unbalanced radial forces are shown, however, the vibration analysis is focused on maximum deflection and not on the correlation between single exciting mechanisms and the system response. In [11] a theoretical study shows that the segment passing frequency described by (5) induce vibrations in the outer rotor which is generating acoustic noise. [12] also presents a theoretical study on a magnetically geared PMSM for an in-wheel traction application. By coupling a model of forced vibrations with an acoustic model, the acoustic response of the different components are simulated. However, not many details regarding the exciting frequencies and the system response are mentioned, and the results are only given as sound pressure in dB on a sphere.

In [13] it is shown that the segment passing frequency (5) and the pole passing frequency (7) are some of the dominant frequencies in the acoustic frequency spectrum obtained for a physical demonstrator. However, the frequency spectrum is divided in 1/3 octave bands, hence it is difficult to observe the exact frequencies available in the spectrum. More detailed results are shown in [8] where the vibrations of two MGs are measured by an accelerometer placed on the housing. Again, a correlation between the dominating frequencies in the frequency spectrum and the segment passing frequency is seen.

In [14], a combination of A-weighted sound pressure level (SPL) and waterfall plots are used to illustrate the frequency response in the sound of a magnetically geared generator for a small wind turbine as a function of speed. It is shown that a large part of the acoustic noise is originating inside the gear, and it is shown, that the SPL can be reduced by increasing the stiffness of the segment ring by increasing the thickness of the bridge between the segments. What is really interesting in this study is that very distinct, speed dependent frequencies are seen in the frequency spectrum of the sound, and these frequencies are to some degree correlated with the frequency spectrum of the magnetic force between the rotors.

In this paper a detailed analysis of the consequence of cogging torque and unbalanced radial forces with respect to vibrations and acoustic noise is presented. Focus is on each individual exciting mechanisms and how they are seen as vibrations and acoustic noise. The analysis is based on experimental data from three different magnetic gears that are presented in Section II and in Section III the test setup is described. In Section IV the acoustic and vibration signature of the three MGs are illustrated and analyzed and finally, the conclusions are presented in Section V.

II. CASE STUDIES AND TEST SETUP

This study is based on three different MGs. Each MG has distinct properties which are interesting in the analysis of the origin of vibration and acoustic noise.

A. *MagCon V1*

MagCon V1 is the first version of a magnetically geared drive unit for a chain conveyor system [15], seen in Fig. 1. The drive unit is designed with the MG integrated into the white sprocket that drives the conveyor chain.

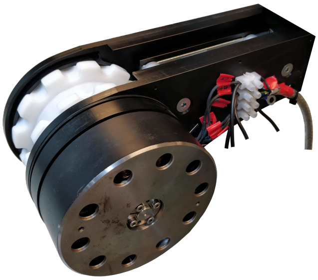

Fig. 1. MagCon V1 drive unit.

The sprocket is placed between two flanges. The flange in the front where the wiring is fixed is termed the *motor flange*, as the motor is mounted here. The flange behind that is termed *encoder flange* as an encoder can be connected to the inner rotor through a hole (not visible in the figure).

The segment ring is stationary, and the inner rotor is sharing the shaft with the rotor of the outer-runner PMSM that is seen next to the sprocket. The main parameters for the MG and PMSM are given in Table I and in Fig. 2 the cross sections of the MGs in this study are shown.

TABLE I
MAIN PARAMETER FOR MGS IN THE STUDY.

	MagCon V1	MagCon V3	Marine generator
MG p_i	2	3	6
MG Q	32	35	46
MG p_o	30	32	40
Gear ratio	15:1	10.67:1	6.67:1
MG C_T	4	1	2
MG stack length	80 mm	104 mm	50 mm
Outer diameter	100 mm	100 mm	340 mm
Slip torque, measured	89 Nm	109 Nm	1147 Nm
PMSM n_{pp}	5	10	-
PMSM n_{slots}	12	18	-

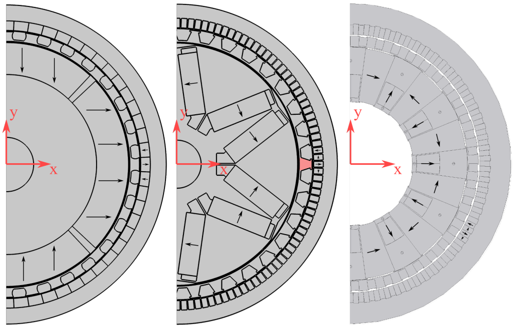

MagCon V1 MagCon V3 MHG MG

Fig. 2. Cross sections of the MGs in this study. MagCon V1 and MagCon V3 are in neutral position, MHG MG is in maximum torque position. Magnetisation direction is shown by black arrows.

MagCon V1 had severe cogging torque which should also be expected from the integer gear ratio and the high C_T. The amplitude of the cogging torque on the inner rotor is 42 % of the rated torque. On the other hand the unbalanced radial forces are minor, and this combination of cogging torque and minor unbalanced radial forces makes the MG interesting in this study.

B. *MagCon V3*

MagCon V3 is a slight evolution of MagCon V2 [16] which was developed to solve the problems with the first version. Besides cogging torque, a large problem with MagCon V1 was huge rotational losses. Because the main focus when designing MagCon V1 was on torque density, the MG was driven in hard magnetic saturation, and large stray fields were inducing eddy current losses in the surrounding components of the gear. These problems were corrected in MagCon V2 by using a new inner-rotor PMSM with buried magnets to decrease eddy current losses and an updated MG with a modified pole configuration to avoid cogging torque. Also, buried magnets on the inner rotor were used to reduce the eddy current losses and to have a mechanical retention of the magnets. In general, the induction level was decreased in the MG while increasing the stack length to reach the design target of the slip torque. The difference between MagCon V2 and MagCon V3 primarily consisted in using a larger air gap, a thicker and more rigid segment ring and the introduction of a Halbach magnet array on the outer rotor. The MagCon V3 is seen in Fig. 3 and the main parameters for the MG and PMSM are given in Table I.

With a C_T of 1 the cogging torque is very small in this gear and this was also one of the focus points during the design. However, as could be expected, the MG does have unbalanced radial forces. The combination of very small cogging torque and unbalanced radial forces makes this MG the second interesting case for this study.

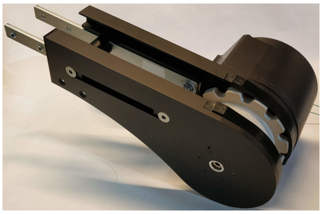

Fig. 3. MagCon V3 drive unit.

C. *Marine Hydrokinetic Generator, Stage 1*

In [17] the first stage of a two-stage Marine Hydrokinetic Generator (MHG) is designed. Due to the integration with the second stage, the first stage is designed with a stationary segment ring which makes it suitable for comparison to MagCon V1 and MagCon V3. During the design phase in [17] both cogging torque and radial forces have been considered. The starting point is an MG with p_i=3, Q=23 and p_o=20 which yields a C_T of 1, i.e. low cogging torque. To avoid unbalanced radial forces, the number of poles and segments are doubled, thereby obtaining a C_T of 2 and a good compromise between cogging torque and unbalanced radial force. This makes this MG an interesting third case in this study. The main parameters are given in Table I. Fig. 4 shows the MG mounted in the test setup. The inner rotor of MG is coupled to a mechanically geared servo motor through a torque transducer on the left. The outer rotor is also coupled to an electric machine on the right side through a torque transducer. During the acoustic tests, the right side is decoupled and the MHG MG is driven by the mechanically geared servo motor.

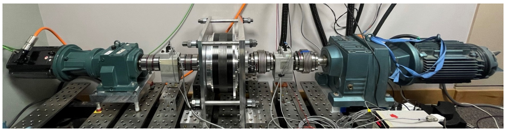

Fig. 4. MHG MG mounted in the test setup. In the left side the mechanical gear and load servo motor is seen and in the right side the mechanically geared driving motor is seen.

III. TEST SETUP

The acoustic and vibrational characteristics of the MagCon drive units are analyzed via sound pressure and acceleration data at a number of fixed speeds. Eigenfrequencies of the outer rotor and segment ring of the MGs are determined by using a hammer test where the components are excited with a hammer blow and the response is measured by accelerometers.

The sound pressure and vibration data was collected with a GRAS PH40 microphone with 20 kHz frequency range and two Brüel & Kjaer 4503 single axis accelerometers with a frequency range of 23 kHz. The data is sampled at 51.2 kHz in a LabVIEW application through a NI9234 module that features an anti aliasing filter. Besides recording the sound with the GRAS microphone, the A-weighted sound pressure level (SPL) is logged with a Brüel & Kjaer 2230 sound level meter.

In the intended application for MagCon V1 and V3, the drive unit is mounted to an aluminum beam on which the conveyor chain glide. However, to minimize the influence of resonances in the aluminum beam, the drive units are suspended in two strings while testing as seen in Fig. 5.

The microphone is placed 1 meter from the motor housing. One accelerometer is placed on the encoder flange and the other accelerometer is placed on the end of the motor housing, hence both accelerometers are measuring accelerations in the axial direction of MG and PMSM. The PMSM is driven by a Danfoss VLT at a switching frequency of 10 kHz, and since the drive units are hanging by two strings, they are not loaded during tests.

The MG for the MHG is evaluated by sound only due to availability of equipment. However, as will be shown in Section IV, both acoustic and vibrational data are suitable for the purpose of this study. The sound pressure is logged at 96 kHz with a Zoom H1n sound recorder placed 300 mm from the MG.

IV. ACOUSTIC AND VIBRATIONAL SIGNATURE

To illustrate the frequency spectrum of some physical quantity as a function of time, speed or other parameters of interest, waterfall plots are a useful tool. For the study in this paper, the varying parameter is the speed of the inner rotor. The waterfall plots are formed by measuring some physical quantity (sound-pressure and acceleration) at several different speeds. An FFT is then performed on the data associated with each test point, and the resulting frequency spectra are plotted in a surface plot with the FFT bin-frequency on the y-axis, the speed of the inner rotor on the x-axis and the amplitude of each frequency bin indicated by color.

A. MagCon V1 - Signature

In Fig. 6 the waterfall plot for the sound pressure of MagCon V1 is shown and several straight lines constituted by peaks in amplitude are seen in the figure.

Lines showing a change in frequency as function of speed shows the frequency of various exciting mechanisms in the system, and in Fig. 6, four of these lines are particularly clear. Horizontal lines show eigenfrequencies of the system or other constant frequencies from the environment. Besides the clear horizontal lines at low frequency, two lines between 1000 Hz and 1200 Hz, where sound pressure increase in amplitude when they are crossing the speed dependent lines, are clearly seen. A good amount of information can be gained from Fig. 6, however, sound data is sensitive to the environment in which it is recorded. To isolate the vibrations associated with the drive unit, the supplementary acceleration data is used. Fig. 7 shows a waterfall plot for the acceleration measured on the encoder flange. It is seen that acceleration and sound are closely related as many of the horizontal lines and speed dependent lines are present in both plots, however, the sound pressure data is influenced by background noise in the low frequency range while the acceleration data only show information relating to the actual acceleration of the gear in this area. Furthermore, more horizontal lines or bands are visible in the acceleration data.

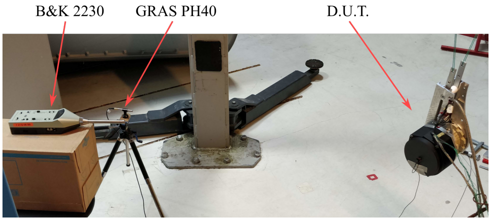

Fig. 5. Test setup used when logging data for the two MagCon drive units. This picture is taken before the two flanges were painted black.

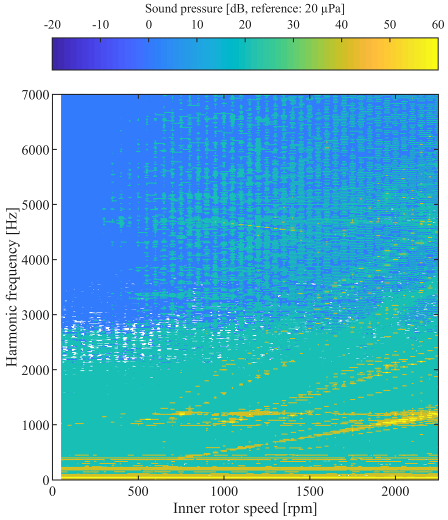

Fig. 6. Waterfall plot based on *sound pressure* for MagCon v1.

In Fig. 8 various reference lines are added to the waterfall plot of the acceleration. Eigenfrequencies of the rotor for the PMSM is indicated by the red, horizontal dot-dash lines. Speed dependent exciting frequencies are indicated with black lines. Each black line is identified by a letter and a number on the right side of the figure to indicate which exciting mechanism and what harmonic number they belong to. The letter key is given in Table II.

TABLE II
EXCITING MECHANISMS IN MAGCON V1.

a	MG cogging torque frequency, Eq. (3)
b	MG segment passing frequency, Eq. (5)
c	PMSM cogging torque, Eq. (9)
d	PMSM static eccentricity, Eq. (11)

For the specific pole configuration used in MagCon V1 the

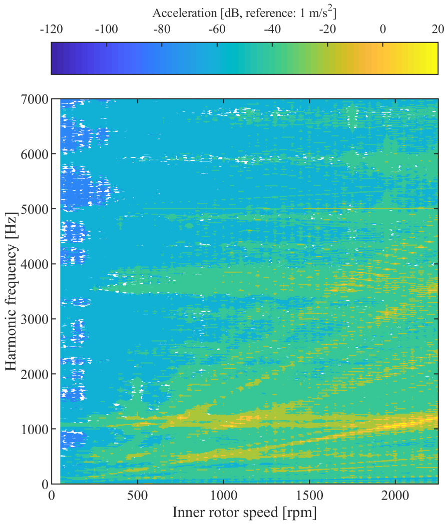

Fig. 7. Waterfall plot from *acceleration* on encoder flange for MagCon v1.

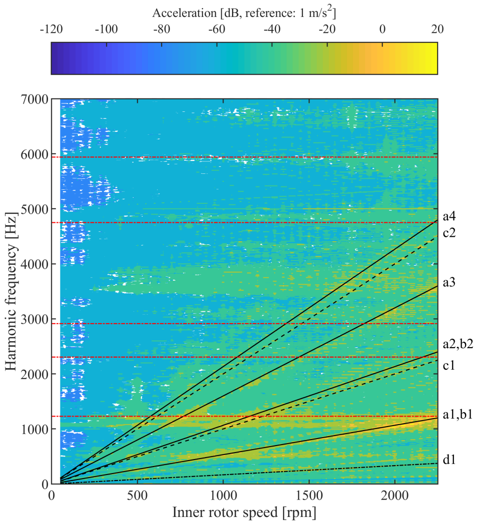

Fig. 8. Frequency references included in acceleration waterfall plot for MagCon v1.

frequency of cogging torque and segment pass-frequency are identical, hence no independent lines are present for the segment pass-frequency. The dominating excitation mechanisms in this MG are clearly related to the lines describing MG cogging torque and segment pass-frequency. Especially the cogging torque frequency is expected due to the very evident presence of this in MagCon V1. From what was found in [5] it is not unlikely that the segment pass-frequency have some influence as well, however, naturally it is not possible to distinguish between the two in this specific case.

The fundamental of the PMSM cogging torque is given as (8) and the frequency is given as (9).

$$n_{CogPMSM} = LCM(n_{pp}, n_{slots}) \tag{8}$$

$$f_{CogPMSM} = n_{CogPMSM} \cdot \frac{\omega_i}{2\pi} \tag{9}$$

In Fig. 8 it is seen that the fundamental and 2$^{\text{nd}}$ harmonic fits two lines very well. Finally, a correlation is seen between a line in the waterfall plot and the frequency related to static eccentricity of the PMSM. When the PMSM rotor is eccentric with the stator, additional cogging is introduced every time a rotor pole passes the stator tooth that is close to the rotor, hence the fundamental of static eccentricity in the PMSM is given by (10) and frequency by (11).

$$n_{PMSMstatEcc} = 2n_{pp} \tag{10}$$

$$f_{PMSMstatEcc} = n_{PMSMstatEcc} \cdot \frac{\omega_i}{2\pi} \tag{11}$$

However, the static eccentricity is not significant compared to the PMSM cogging torque, and it is very small compared to MG cogging torque and segment pass-frequency.

In Fig. 8 it is seen that some of the eigenfrequencies of the PMSM rotor coincides with the horizontal lines in the waterfall plot, and particularly high amplitudes are seen around the horizontal line at approximately 1200 Hz. It is furthermore seen that when the frequency of an exciting mechanism crosses this eigenfrequency, the accelerations are amplified which can be expected.

The majority of the accelerations with high amplitudes occur around a relatively narrow band of frequencies between 1000-1200 Hz. This corresponds well to what was experienced in the lab during testing where the acoustic noise was perceived as being concentrated within a relatively narrow frequency band which would hit clear resonances when changing the speed.

B. MagCon V3 - Signature

Fig. 9 shows the waterfall plot for the sound pressure of MagCon V3, and similar to MagCon V1, different lines are present in the plot. Fig. 10 shows a waterfall plot of the acceleration measured on the encoder flange of MagCon V3. The speed range for the waterfall plot is lower compared to MagCon V1. This is due to the lower gearing ratio of this gear as the speed range of the waterfall plots cover the same output speed for both MagCon drive units. Again the dominating amplitudes are following linear patterns. Notice how the peak values of similar amplitude are present at several different frequencies at a given speed. This is different from the signature of MagCon V1 where the peak values were concentrated around a very narrow frequency band. It corresponds well to how the sound was perceived during tests of MagCon V3 where the noise seemed to be distributed over a broader spectrum.

Both sound pressure and acceleration data show several vertical lines where the amplitude at *all frequencies* increase.

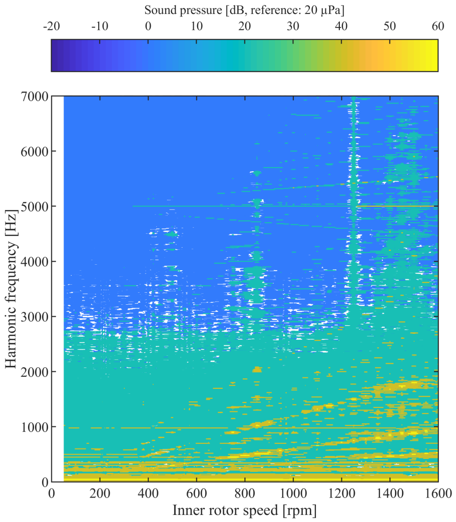

Fig. 9. Waterfall plot for sound data from MagCon v3.

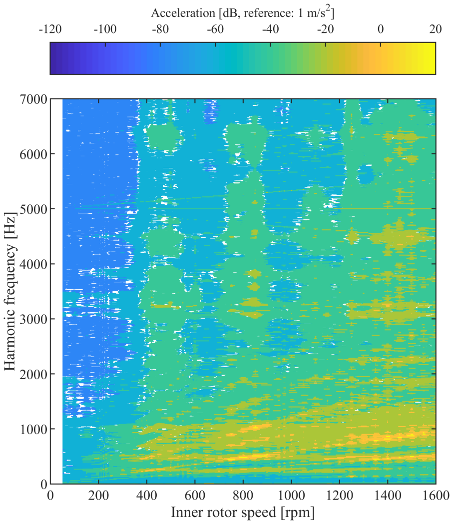

Fig. 10. Waterfall plot for acceleration data from MagCon v3.

These vertical lines appear when a resonance is excited at some speed, which creates vibrations powerful enough to excite all components in the system.

In Fig. 11 reference lines for the exciting frequencies are added to the waterfall plot. Again, speed dependent exciting frequencies and their harmonics are indicated by black lines identified by letters and numbers. The letter key is given in Table III.

TABLE III
EXCITING MECHANISMS IN MAGCON V3.

a	MG cogging torque frequency, Eq. (3)
b	MG unbalanced radial force
c	MG segment passing frequency, Eq. (5)
d	MG Pole passing frequency, Eq. (7)
e	PMSM cogging torque, Eq. (9)
f	PMSM static eccentricity, Eq. (11)

a) MG cogging torque From line *a1* in Fig. 11 it is clear that the vibrations due to cogging torque in the MG have been reduced significantly compared to MagCon V1 as the convergence between line *a1* and peak values in the acceleration data is much less pronounced.

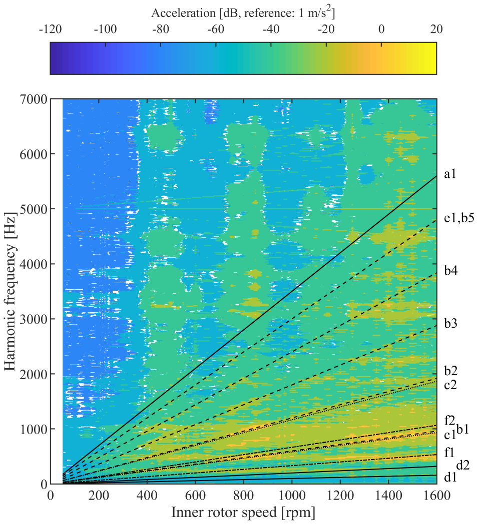

Fig. 11. Frequency references included in acceleration waterfall plot for MagCon v3.

b) MG unbalanced radial forces The new significant source of vibrations in the MagCon V3 is the unbalanced radial forces. Fig. 12 show the *y*-component of the forces on each MG rotor evaluated in the *xy*-plane shown in Fig. 2 while rotating the inner rotor one full mechanical rotation with the MG in neutral position. The results are obtained from COMSOL and a matching result with respect to amplitude and number of cycles were obtained from a JMAG model. Each rotor is going through 36 cycles, hence this is the fundamental for the reference lines in Fig. 11. The FFT of the acceleration from both accelerometers at an inner rotor speed of 1100 rpm is shown in Fig. 13. This speed is chosen as few resonances exist here, hence a cleaner impression of the vibration is obtained. At 1100 rpm the fundamental frequency of the unbalanced radial forces is 660 Hz and it is clear, that this frequency and the 2nd and 3rd harmonics are dominating. Also, a peak is seen at 366.75 Hz, which is the static eccentricity

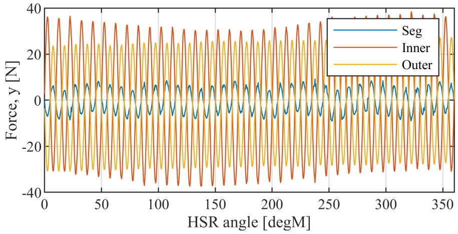

Fig. 12. Y-component of forces in xy-plane on MG rotors for MagCon V3.

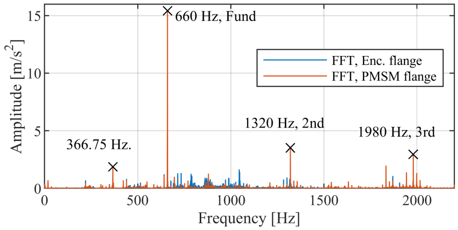

Fig. 13. FFT of accelerations at 1100 rpm inner rotor speed.

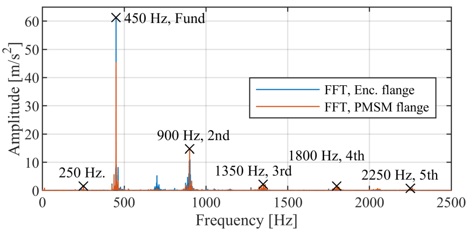

Fig. 14. FFT of accelerations at 750 rpm inner rotor speed.

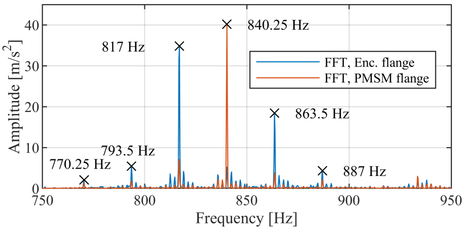

Fig. 15. Side lobes on unbalanced radial forces. Inner rotor speed: 1400 rpm.

of the PMSM.

In Fig. 14 an FFT of the acceleration at an inner rotor speed of 750 rpm is shown. At this speed, a resonance is excited and the SPL increases to 74 dBA compared to 62 dBA if the speed is decreased by 50 rpm to 700 rpm. At 750 rpm the peak values in the FFT continues to be concentrated around the fundamental frequency of the unbalanced radial forces as well as the harmonics. Note that the static eccentricity of the PMSM at 250 Hz is also seen at this speed.

In Fig. 14 a great deal of frequency content is seen around the unbalanced radial force frequency and its harmonics. To illustrate what is going on, Fig. 15 shows the FFT at an inner rotor speed of 1400 rpm with focus on the fundamental frequency of the unbalanced radial force at 840.25 Hz. Side lobes equally spaced around the fundamental frequency are clearly seen. The distance between the side lobes are approximately the frequency of the inner rotor, which at 1400 rpm is 23.33 Hz. If Fig. 12 is studied, it is seen that the force on the inner rotor is varying slowly with one period for the mechanical revolution represented in the figure hence the side lobes in Fig. 15 are similar to the side lobes seen on inverter switch frequencies which are spaced with the fundamental electrical frequency of the electric machine that is driven [18]. In the case of the MG, the fast varying radial force, 36 periods per revolution, corresponds to the switching action in the inverter and the slow variation in the radial forces, 1 period per revolution, resembles the fundamental frequency of the electric machine.

In Fig. 15 it is further seen that the fundamental of the radial force and primary side lobes actually have small secondary side lobes. The spacing of these side lobes approximately corresponds to the frequency of the outer rotor which at an inner rotor speed of 1400 rpm is 2.19 Hz. Due to the 0.25 Hz resolution in frequency bins, the FFT is not able to represent the spacing of the primary and secondary side lobes exactly.

c) MG segment pass-frequency In Fig. 11 it is seen that the segment pass-frequency is close to the frequency of the unbalanced radial forces, hence they are not easy to distinguish between in the waterfall plots. Depending on the inner rotor speed, the segment pass-frequency has a significant amplitude when looking at the FFT for a single speed, but *how* significant depends on how close the segment pass-frequency is on one of the system eigenfrequencies. In the FFT for 1400 rpm in Fig. 15 the fundamental of the segment pass-frequency is 816.67 Hz, and it is seen, that the primary side lobe at 817 Hz is higher than the opposite primary side lobe at 863.5 Hz. This indicates that even though the unbalanced radial forces are dominating, the segment pass-frequency cannot be ignored.

d) MG pole pass-frequency Even though it is not the most dominating frequency, the pole pass-frequency is visible in Fig. 11. The fundamental, 2nd harmonic and 3rd harmonic are visible, but only the first two are shown with a line in the figure to make the figure more clear to interpret. The origin of the pole pass-frequency can be analyzed by studying the resulting radial magnetic force on a single segment as a function of inner rotor position. This has been done in JMAG and the result for 60 mechanical degrees (*one* inner rotor pole) is seen in the upper part of Fig. 16. The initial position is shown in Fig. 2 where the inner rotor pole oriented to the right is aligned with a red segment which is the segment on which the resulting radial force is evaluated. A negative force indicates that the segment is pulled towards the inner rotor. Below the radial force in Fig. 16, the frequency spectrum up to the 10th harmonic is shown. From the FFT it is clear, that especially the 2nd and 3rd harmonic have significant amplitudes. Hence, a clear correlation between pole pass-frequency, magnetic forces on the segments and acoustic noise as well as vibration is seen.

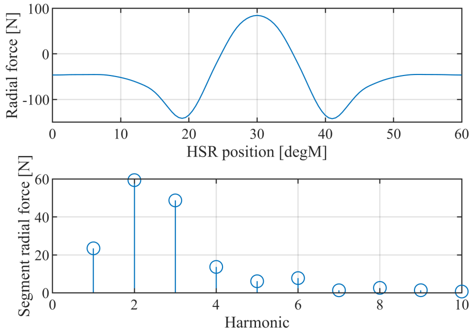

Fig. 16. Top figure shows radial force on a single segment during 60 mechanical degrees on inner rotor (*one* pole) and bottom figure shows the frequency spectrum.

e) PMSM cogging torque The PMSM cogging torque frequency is identical to the 5th harmonic of the unbalanced radial forces. This makes it difficult to distinguish between the two, but some activity is seen around this frequency, both in the waterfall plot, but also in Fig. 14. Accelerations at this frequency are not significant compared to unbalanced radial forces in MagCon V3 though.

f) PMSM static eccentricity The frequencies related to static eccentricity of the PMSM rotor is clearly visible and have been seen in all the single speed FFTs that have been shown for MagCon V3. Even though only the fundamental frequency have been indicated, a peak is clearly seen at the 2nd harmonic too. It makes sense that the PMSM is eccentric to some degrees. The bearings of the inner rotor shaft is placed on an aluminum shaft in the PMSM-end, and because the MagCon V3 has been assembled and disassembled several times during tests, the fit between shaft and bearing is not tight. Hence, when assembling the drive unit, the bearing is mounted with Loctite, and while the Loctite dries, the rotor will be pulled to one side by the magnetic forces.

C. Marine Hydrokinetic Generator - Signature

The waterfall plot based on sound pressure for the MHG MG is seen in Fig. 17. It is seen that the inner rotor speed is low compared to the two prior MGs but as the pole count is higher for the MHG MG, the relevant exciting frequencies still comes into a range where they can be distinguished from the background noise. The maximum harmonic frequency is reduced to 2 kHz as nothing of interest to this paper is visible above this frequency. For MagCon V1 and V3 it is possible to distinguish acoustic background noise from MG noise by using the acceleration data. As acceleration data is not available for the MHG MG the influence of background noise is identified from sound data recorded without the MG running. The FFT of the background noise is shown in Fig. 18 and it is seen, that the frequency of the peaks identified by a black *X* is also seen as a horizontal lines in Fig. 17. One source of background noise is the air conditioner in the laboratory which emits noise at frequencies around 1500 Hz.

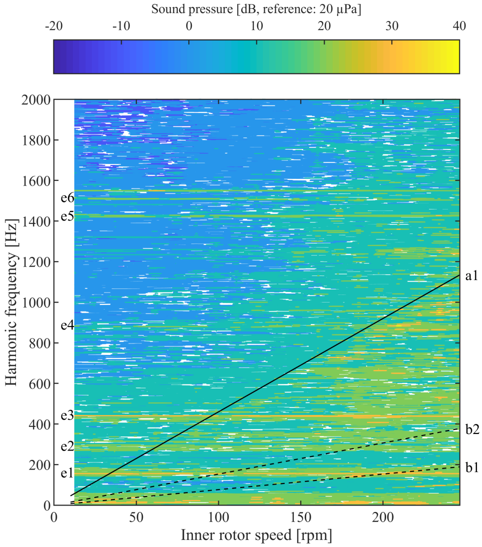

Fig. 17. Waterfall plot based on sound from the first stage of the MHG MG.

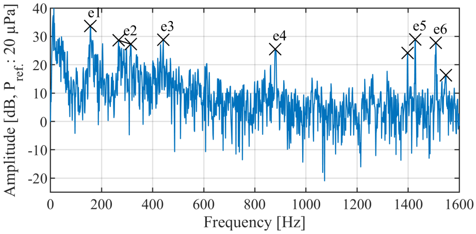

Fig. 18. FFT of acoustic background noise.

The reference lines in Fig. 17 are identified in Table IV. Because this is a stand-alone MG, frequencies associated with an electric machine are not included in the frequency references.

In Fig. 17 a few resonances related to cogging torque and segment pass-frequency are seen but not nearly to the

TABLE IV
EXCITING MECHANISMS IN MHG MG.

a	MG cogging torque frequency, Eq. (3)
b	MG segment passing frequency, Eq. (5)

same extent as with the MagCon drive units, and they are only just visible in Fig. 17. There is no clear influence from the unbalanced magnetic forces either. Fig. 19 show the y-components of the forces on each MG rotor, evaluated in the xy-plane defined in Fig. 2. It is seen that the unbalanced magnetic forces are small, especially when considering that the slip torque of this MG is close to 13 times higher compared to the MagCon V3. This is consistent with the perception of the sound during testing, where the MG runs silent with no distinct frequencies that dominates the sound picture. Only one clear speed-dependent line is seen, just below the cogging torque line. During testing the most dominant acoustic noise source that changed pitch with speed was the mechanical gearbox through which the MG was driven, hence it is very likely that this line can be attributed to the mechanical gear.

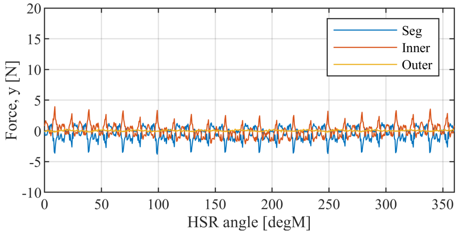

Fig. 19. Y-component of forces in xy-plane on each MG rotor for the MHG MG.

V. Conclusion

By studying three physical concentric magnetic gears with different pole configurations it has been shown how cogging torque and unbalanced radial magnetic forces have a significant impact on the acoustic and vibrational signature of the magnetic gears. MagCon V1 have well balanced radial forces but a large cogging torque and it is seen that the cogging torque frequency and the harmonics are dominating in the waterfall plots based on sound pressure and acceleration data. MagCon V3 has minimal cogging torque but the radial magnetic forces are unbalanced, and in this case it is the unbalanced radial forces which dominate the waterfall plots. It is further shown that by having unbalanced radial forces, primary and secondary side lobes to the fundamental and harmonic frequencies of the radial forces are introduced. The first stage for the MG used in an MHG were designed with a pole configuration that features a good balance between balanced radial forces and cogging torque, and from the waterfall plot it is clear that there are no directly dominating frequencies related to the MG. One speed-dependent line is seen but this is attributed to the mechanical gear through which the MG is driven. This study confirms that from a practical point of view the choice of pole configuration is very important in the early design stage of a concentric magnetic gear.

It has furthermore been shown how the segment pass-frequency and pole pass-frequency will add to vibrations and acoustic noise, especially when they cross the eigenfrequency of various components in the magnetic gear. These exciting mechanisms cannot be avoided through the choice of pole- and segment-configuration so, when possible, resonances should be avoided by designing the gear components with eigenfrequencies that will not interfere with the these specific exciting mechanisms.

Acknowledgment

The authors would like to thank JMAG for the use of their FEA software.

References

[1] P. Rasmussen, T. Andersen, F. Joergensen, and O. Nielsen, "Development of a high performance magnetic gear," in *38th IAS Annual Meeting on Conference Record of the Industry Applications Conference, 2003.*, vol. 3, 2003, pp. 1696–1702 vol.3.

[2] K. Atallah and D. Howe, "A novel high-performance magnetic gear," *IEEE Transactions on Magnetics*, vol. 37, no. 4, pp. 2844–2846, 2001.

[3] S. C. K. Atallah and D. Howe, "Design, analysis and realisation of a high-performance magnetic gear," in *IEE Proceedings - Electric Power Applications*, vol. 151, no. 2, 2004, pp. 135–143.

[4] Z. Zhu and D. Howe, "Influence of design parameters on cogging torque in permanent magnet machines," *IEEE Transactions on Energy Conversion*, vol. 15, no. 4, pp. 407–412, 2000.

[5] N. Niguchi and K. Hirata, "Cogging torque analysis of magnetic gear," *IEEE Transactions on Industrial Electronics*, vol. 59, no. 5, pp. 2189–2197, 2012.

[6] N. W. Frank and H. A. Toliyat, "Gearing ratios of a magnetic gear for marine applications," in *2009 IEEE Electric Ship Technologies Symposium*, 2009, pp. 477–481.

[7] G. Jungmayr, J. Loeffler, B. Winter, F. Jeske, and W. Amrhein, "Magnetic gear: Radial force, cogging torque, skewing, and optimization," *IEEE Transactions on Industry Applications*, vol. 52, no. 5, pp. 3822–3830, 2016.

[8] C. J. Agenbach, D. N. J. Els, R.-J. Wang, and S. Gerber, "Force and vibration analysis of magnetic gears," in *2018 XIII International Conference on Electrical Machines (ICEM)*, 2018, pp. 752–758.

[9] M. Johnson, M. C. Gardner, H. A. Toliyat, S. Englebretson, W. Ouyang, and C. Tschida, "Design, construction, and analysis of a large-scale inner stator radial flux magnetically geared generator for wave energy conversion," *IEEE Transactions on Industry Applications*, vol. 54, no. 4, pp. 3305–3314, 2018.

[10] S. Modaresahmadi, K. Li, W. B. Williams, and J. Z. Bird, "Vibration analysis of the first stage of a multi-stage coaxial magnetic gearbox," in *SoutheastCon 2018*, 2018, pp. 1–8.

[11] J. Y. Lee and J. H. Chang, "Vibration and noise characteristics of coaxial magnetic gear according to low-speed rotor structure," *Journal of Mechanical Science and Technology*, vol. 31, no. 6, pp. 2723–2728, 2017.

[12] C. V. Pop, D. Fodorean, C. Husar, and C. Irimia, "Noise and vibration analysis of an in-wheel motor with integrated magnetic gear dedicated for light electric application," in *2019 8th International Conference on Modern Power Systems (MPS)*, 2019, pp. 1–5.

[13] J. Lee and J. Chang, "Analysis of the vibration characteristics of coaxial magnetic gear," *IEEE Transactions on Magnetics*, vol. 53, no. 6, pp. 1–4, 2017.

[14] S. Korsgaard, A. B. Kjaer, S. Staal Nielsen, L. Demsa, and P. O. Rasmussen, "Acoustic noise analysis of a magnetically geared permanent magnet generator," in *2019 IEEE Energy Conversion Congress and Exposition (ECCE)*, 2019, pp. 717–723.

[15] S. S. Nielsen, R. K. Holm, and P. O. Rasmussen, "Conveyor system with a highly integrated permanent magnet gear and motor," *IEEE Transactions on Industry Applications*, vol. 56, no. 3, pp. 2550–2559, 2020.

[16] S. S. Nielsen, R. Koldborg Holm, N. I. Berg, and P. Omand Rasmussen, "Magnetically geared conveyor drive unit - an updated version," in *2020 IEEE Energy Conversion Congress and Exposition (ECCE)*, 2020, pp. 285–292.

[17] H. Baninajar, J. Z. Bird, S. Modaresahmadi, and W. Williams, "Electromagnetic and mechanical design of a hermetically sealed magnetic gear for a marine hydrokinetic generator," in *2018 IEEE Energy Conversion Congress and Exposition (ECCE)*, 2018, pp. 4987–4993.

[18] N. Mohan, T. M. Undeland, and W. P. Robbins, *Power Electronics. Converters, Applications and Design*, 3rd ed. John Wiley and Sons, Inc, 2003.

Simon Staal Nielsen Simon Staal Nielsen received his M.Sc. degree in Electromechanical Systems Design in 2015 from Aalborg University. He since worked as a research assistant for 3 years with switched reluctance machines, power electronics and magnetic gears. He is currently working towards his Ph.D. degree concerning systems design and implementation of magnetic gears, electric machines and power electronics at the Department of Energy Technology on Aalborg University.

Ho Yin Wong David Wong received his B.S. degree in Electrical and Computer Engineering from Syracuse University, New York in 2015, and his M.S. degree in Electrical and Computer Engineering with a focus in Power Engineering from Portland State University, Oregon in 2017. He is currently pursuing his Ph.D. degree at Portland State University. His research interests are in the area of design and analysis of magnetic gears and permanent magnet machines for renewable energy and electrified transportation drivetrain applications.

Hossein Baninajar Hossein Baninajar received the B.S. and M.S. degrees in electrical engineering from the Chamran University of Ahwaz, Iran, and University of South Carolina, Columbia, USA, in 2007 and 2017 respectively. He is currently pursuing his Ph.D. degree in electrical machinery design at Portland State University, Portland, OR, USA. His research interests include finite element analysis and design of electric machines, magnetic gears, and renewable energies.

Jonathan Z. Bird Jonathan Z. Bird (M'02) received the B.S. degree in electrical and computer engineering from the University of Auckland, Auckland, New Zealand, in 2000, and the M.S. and Ph.D. degrees in electrical and computer engineering from the University of Wisconsin–Madison, Madison, WI, USA, in 2004 and 2006, respectively.,From 2006 to 2008, he was a Senior Design Engineer with the General Motors Advanced Technology Center, Torrance, CA, USA. From 2009 to 2015, he was an Assistant then Associate Professor with the University of North Carolina at Charlotte, Charlotte, NC, USA. He is currently an Associate Professor with the Portland State University, Portland, OR, USA. His research interests include electric machine design, electromagnetics, and control.

Peter Omand Rasmussen Peter Omand Rasmussen received his M.Sc.E.E and Ph.D. degrees from Aalborg University, Aalborg, Denmark, in 1995 and 2001 respectively. In 1998 he became Assistant Professor, and in 2002 he became Associate Professor at the Department of Energy Technology at Aalborg University. His research areas are the design and control of switched reluctance machines, permanent magnet machines, and magnetic gears.

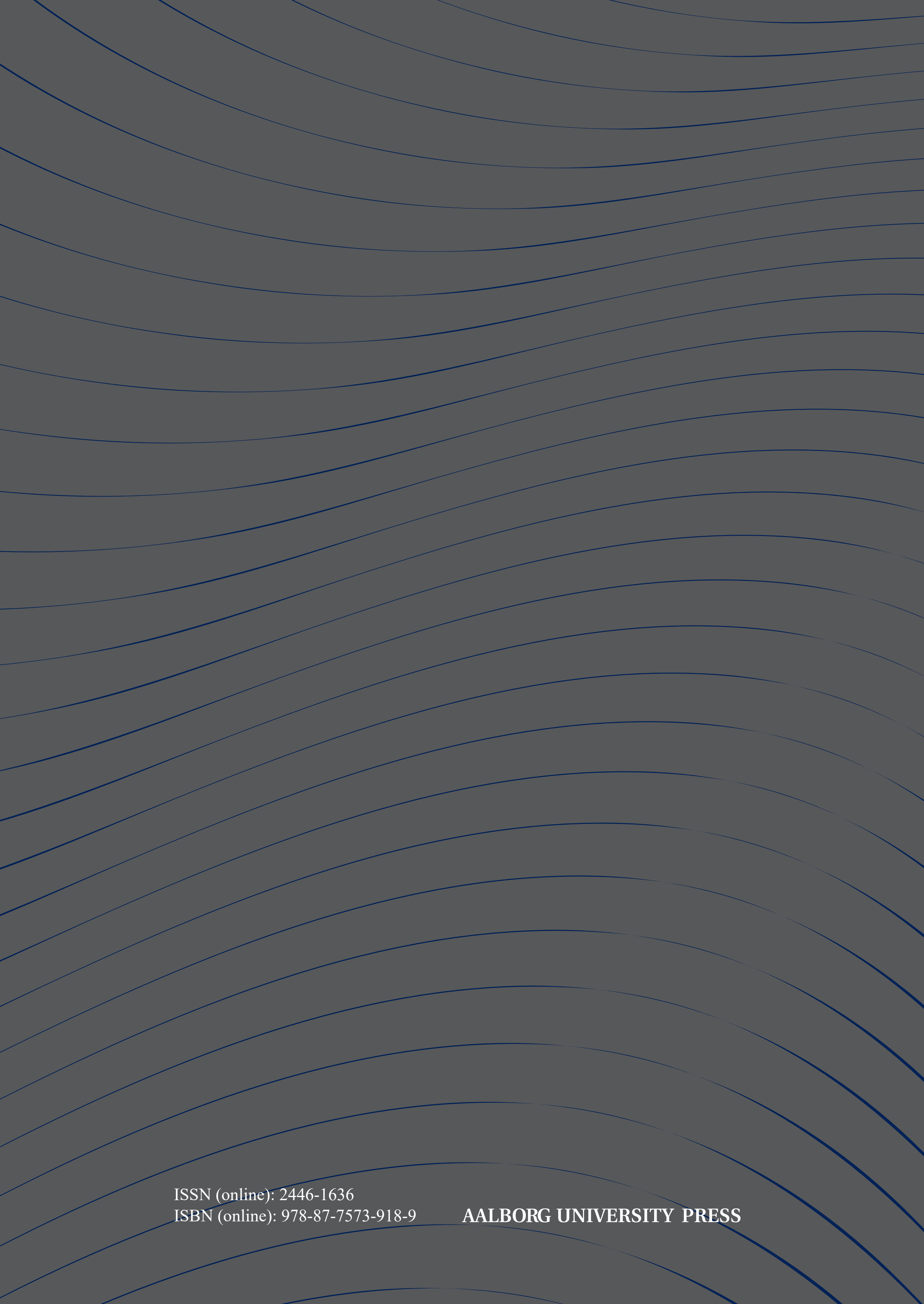

ISSN (online): 2446-1636
ISBN (online): 978-87-7573-918-9

AALBORG UNIVERSITY PRESS